# Univerzitet u Beogradu

Fizički fakultet



Master rad

# Teorija uranjanja otvorenih kvantnih klastera

Mentori: Student: dr Jakša Vučičević Petar Brinić

prof. dr Đorđe Spasojević

#### Sažetak

Izučavanje jako korelisanih elektronskih sistema je važan deo fizike kondenzovanog stanja materije. U okviru teorije ovih sistema posebna pažnja se posvećuje (interagujućim) niskoenergetskim efektivnim modelima rešetke. Oni predstavljaju kvantni višečestični problem koji je jako težak, a razvoj numeričkih metoda za njegovo rešenje je aktivna oblast istraživanja. Zbog problema konačnosti rešetke i analitičkog produženja naročito je teško računati dinamičke odzive. U ovom radu uvodimo teoriju uranjanja otvorenih kvantnih klastera (eng. open quantum cluster embedding theory, OQCET) sa ciljem računanja odziva nakon spoljašnje pobude. Uz pomoć inverzne teorije linearnog odziva moguće je rekonstruisati dinamičke suceptibilnosti. Metod omogućava tretiranje velikih rešetaka, izbegava analitičko produženje i poštuje zakone održanja energije i broja čestica. U neinteragujućem i atomskom limesu, kao i u limesu beskonačnog klastera metod daje numerički egzaktne rezulate. Uronjeni klasteri, koji se smatraju reprezentativnim za kratkodometne korelacije, su otvoreni kvantni sistemi opisani Lindbladovom jednačinom. Kratkodometne korelacije izračunate na klasterima se koriste da zatvore jednačine kretanja fermionskog bilineara i dvostruke okupiranosti na rešetki. Primenjujemo OQCET u računanju gustina-gustina korelacione funkcije u Habardovom modelu na kvadratnoj rešetki i analiziramo rezultate. Poredimo rezultate sa eksperimentom na hladnim atomima i pokazujemo dobro kvalitativno slaganje.

# University of Belgrade

Faculty of Physics



Master's thesis

# OQCET: Open Quantum Cluster Embedding Theory

Supervisors: Student:

Dr. Jakša Vučičević Petar Brinić

Prof. Đorđe Spasojević

#### Abstract

The study of strongly correlated electron systems is an important field of condensed matter physics. The theory of these systems relies in large part on low-energy effective lattice models. These models pose a difficult quantum many-body problem. The development of numerical methods to solve these (interacting) lattice models is an active area of research. Due to issues of finite-size effects and analytic continuation, the dynamical response functions are especially difficult to calculate. We introduce the open quantum cluster embedding theory (OQCET), an embedded cluster method aimed at computing the response of the system following an external perturbation. This allows one to reconstruct dynamical susceptibilities in the manner of inverse linear response theory. The method is feasible for very large lattices and avoids analytical continuation. OQCET becomes numerically exact in the non-interacting, atomic and infinite cluster size limits, and it respects the total charge and energy conservation laws. The embedded clusters, used within the method as representative of short range correlations, are open quantum systems governed by the Lindblad equation. The short-range correlations extracted from the clusters are used on the lattice to close the equations of motion for the fermionic bilinear and the local double occupancy. We apply OQCET in computation of the charge-charge correlation function in the square lattice Hubbard model and analyze the results. We compare our theoretical results with a cold atom experiment and show good qualitative agreement.

# Acknowledgments

I would like to thank my advisor Dr. Jakša Vučičević for his dedication and guidance in the process of writing this thesis. I am also grateful to my family and friends for their support and encouragement during the course of my studies.

I acknowledge insightful discussions with Hugo Strand. I also thank Michel Ferrero for providing the CTINT data used in this work. The computations were performed at the PARADOX supercomputing facility at the Scientific Computing Laboratory of the Institute of Physics Belgrade. This work was supported with funding provided by the European Research Council, grant ERC-2022-StG: 101076100.

# Contents

A	Acknowledgments						
1	Intr	Introduction					
2 General methodology							
	2.1	Embedded cluster methods	10				
	2.2	Dynamical mean-field theory (DMFT)	10				
		2.2.1 Single site DMFT for the Hubbard model	11				
		2.2.2 Cluster DMFT	13				
	2.3	Linear response theory	16				
3	OQ	OQCET as an embedded cluster method 18					
	3.1	OQCET for the square lattice Hubbard model	22				
	3.2	Inverse linear response theory	22				
	3.3	Lattice equations of motion	25				
	3.4	Preparing the initial state	28				
		3.4.1 Equilibrium lattice thermal averages	28				
		3.4.2 Clusters in equilibrium	29				
	3.5	Cluster dynamics	31				
		3.5.1 Minimization	34				
	3.6	Choice of jump operators	34				
	3.7	Limits in which OQCET becomes exact	36				
	3.8	Post-processing	37				
4	Res	Results 3					
	4.1	Benchmarks	36				
	4.2	Comparison with exact diagonalization	41				
	4.3	Initial cluster state method	43				
	4.4	Effect of constraints and cluster size	43				
	4.5	Comparison of non-equilibrium protocols	45				
	4.6	Comparison with other numerical methods	46				
	4.7	Comparison with experimental results	46				
5	Con	Conclusions					
$\mathbf{A}$	Der	Derivation of the Lindblad equation 5					

В	Energy and particle number conservation	<b>56</b>
$\mathbf{C}$	Numerical Matsubara Fourier transform	59
$\mathbf{D}$	Exact diagonalization	64

# Chapter 1

# Introduction

To accurately describe crystalline materials, one must, in principle, solve the quantum many-body problem of the constituent electrons and the atomic nuclei. The complexity of this problem scales exponentially with the number of particles, so a full solution of the many-body problem is only feasible for very small systems of about 20 particles. In macroscopic materials we work with systems with the order of  $10^{23}$  particles, so it is necessary to develop simplified models and employ a variety of approximate methods.

Methods such as mean field theory and density functional theory (DFT) attempt to reduce the many-body problem to an effective single-particle picture. This proves to be a satisfactory description for a wide range of materials, such as metals and conventional (low temperature) superconductors. The success of the single-particle description in metals can be ascribed to the Fermi liquid theory. In metals the Fermi energy is quite large (in Cu, for example, it corresponds to a Fermi temperature of  $\sim 80000K$ ) so thermal excitations remain close to the Fermi level. The Pauli exclusion principle forbids scattering into occupied states of the Fermi sea, leaving only a small volume of phase space around the Fermi level available for scattering. This effectively suppresses the strong electron-electron Coulomb interaction, allowing for a weakly-interacting quasiparticle description of low energy excitations.

However, there are systems where interactions are more important, and the simple picture of wave-like quasiparticles in an effective potential breaks down. As the potential energy becomes comparable to the kinetic energy, the delocalized states become less energetically favorable. This means that a more particle-like picture incorporating interaction of localized electrons becomes necessary. We refer to materials for which an effective single-particle description fails as *strongly correlated*. [1]

Examples of strongly correlated materials are usually found in compounds containing transition metals, lanthanides and actinides—elements with partially filled d and f orbitals. The stronger confinement in these orbitals means that the electrons experience the Coulomb interaction more strongly, and as a result we see exotic behavior that cannot can be predicted by effective single-particle theories. Common to many of these systems are rich phase diagrams, including metal-insulator (Mott) transitions, ordered phases such as charge and spin density waves and unconventional superconductivity. The disordered metallic phases prove to be no less interesting—one

often observes crossovers between standard Fermi liquid, strange, bad metallic and pseudogap regimes. Strange metals are characterized by a resistivity linear in temperature, as opposed to the quadratic dependence in good metals (as is well understood within the Fermi liquid theory). Bad metals also have a linear temperature resistivity, but the resistivity is so high that it indicates that the effective mean free path is shorter than the interatomic spacing (the so-called Mott-Ioffe-Regel limit) and thus the coherent quasiparticle description of transport breaks down. Strange and bad metal phases are often associated with the existence of a quantum critical point, a continuous phase transition occurring at zero temperature. [1, 2]

The Bardeen-Cooper-Schrieffer (BCS) theory created a framework for understanding the behavior of conventional (low-temperature) superconductors. At low temperatures, the electron-phonon interaction gives rise to a weak attractive interaction between electrons, which form superconducting Cooper pairs. In the 1980s, it was believed that BCS theory placed an upper limit to the superconducting critical temperature  $T_c$  at 30K. In 1986 high- $T_c$  superconductivity was first observed in the doped cuprate  $\text{La}_{2\text{-}x}\text{Ba}_x\text{CuO}_4$  by Bednorz and Müller, sparking a revolution in condensed matter research. In the following years, numerous cuprate superconductors were discovered, pushing  $T_c$  well above 100K (Fig. 1.1). The BCS theory fails to describe the superconductivity in the cuprates, and thus the phenomenon is often referred to as "unconventional" superconductivity. Similarly poorly understood, unconventional superconductivity was also observed in a family of iron-based compounds,  $\kappa$ -organics and moiré lattices. [3–9]

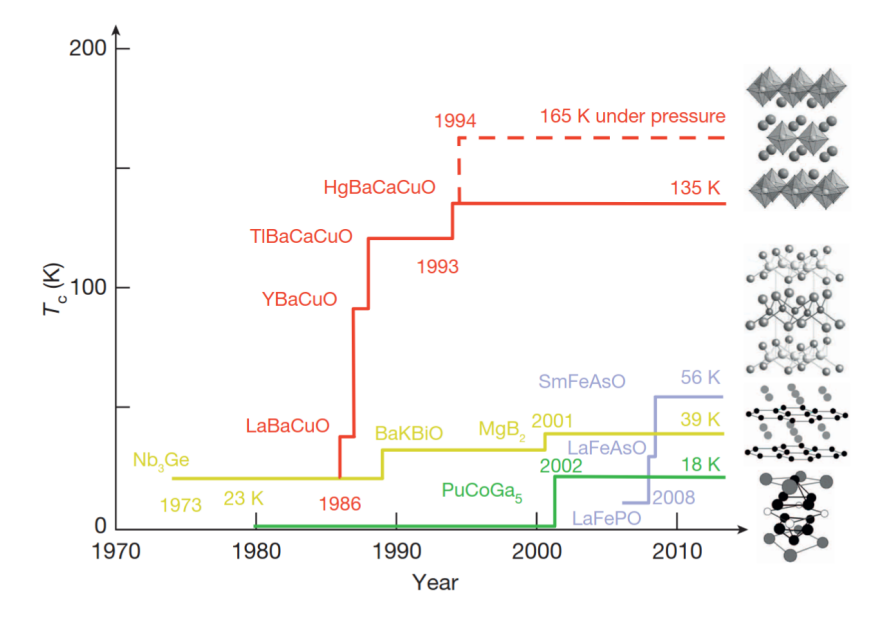


Figure 1.1: Plot of  $T_c$  over time. Cuprate superconductors (red) have the highest  $T_c$ , followed by Fe-based (purple), conventional BCS (yellow) and heavy fermion (green) superconductors. [3]

The cuprates have a structure formed of conducting layers of copper oxide planes separated by buffer layers (Fig. 1.2). DFT calculations indicate that the most signifi-

cant contributions to the electronic bands near the Fermi level come from the copper  $3d_{x^2-y^2}$  and the in-plane oxygen p-orbitals  $(2p_x$  and  $2p_y)$  [10, 11]. However, DFT in general fails to reproduce experimental observations for these materials, especially for the spectral properties. The question of the minimal model to describe the cuprates and capture the mechanisms relevant for superconductivity is an open one. Most common approaches rely on either single-band (Hubbard) models (one orbital per unit cell), or three-orbital Emery models. The importance of other orbitals such as Cu  $3d_{z^2}$ , Cu 4s, apex oxygen  $2p_z$  and even states from the buffer layers cannot be ruled out, and more complicated models are often studied. [12–15]

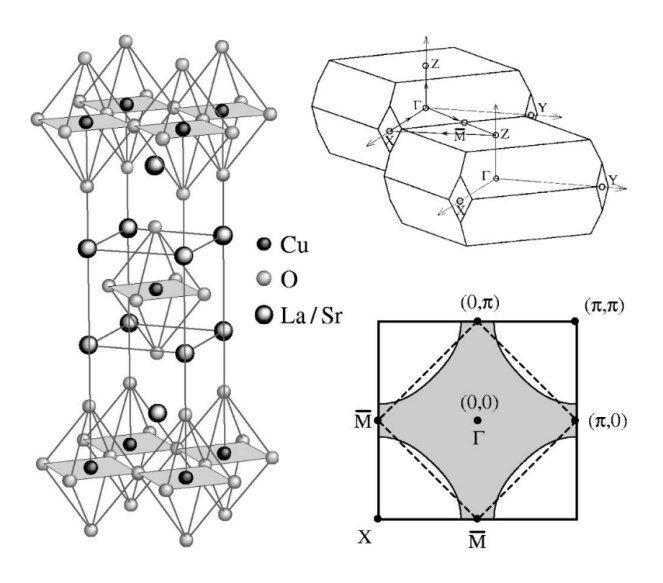


Figure 1.2: The unit cell of  $La_{2-x}Sr_xCuO_4$ , the body-centered tetragonal Brillouin zone and the 2D Brillouin zone projection. [16]

The buffer layers serve as charge reservoirs for the copper-oxide planes. To dope the system, one or more elements in the buffer layers are partially substituted with elements with fewer (hole-doping) or more (electron-doping) valence electrons. Another common way is to reduce the overall number of oxygens. The doping is essential for the cuprates—in many cases, the parent compound is insulating, and the superconducting phase is achieved only upon doping. For example, La<sub>2</sub>CuO<sub>4</sub> can either be doped by replacing La with Ba, Sr (hole dopants), Ce (electron doping), or by reducing the number of oxygens. In all cases the highest critical temperature for the superconductivity that is achieved is roughly the same. [17–20]

The generic cuprate doping-temperature phase diagram (Fig. 1.3) is very complex, and can contain spin and charge density wave ordered phases, insulating and metallic phases, and, most importantly, the superconducting dome: the critical temperature usually grows with doping to a certain point, and beyond it, the trend reverses. The doping at which the  $T_c$  is the highest is called the "optimal doping". [3]

Unlike in conventional superconductors, the superconducting pairing amplitude in the cuprates has d-wave symmetry, which has a very distinctive spectral signature observed in angle-resolved photoemission spectroscopy (ARPES) experiments. A sim-

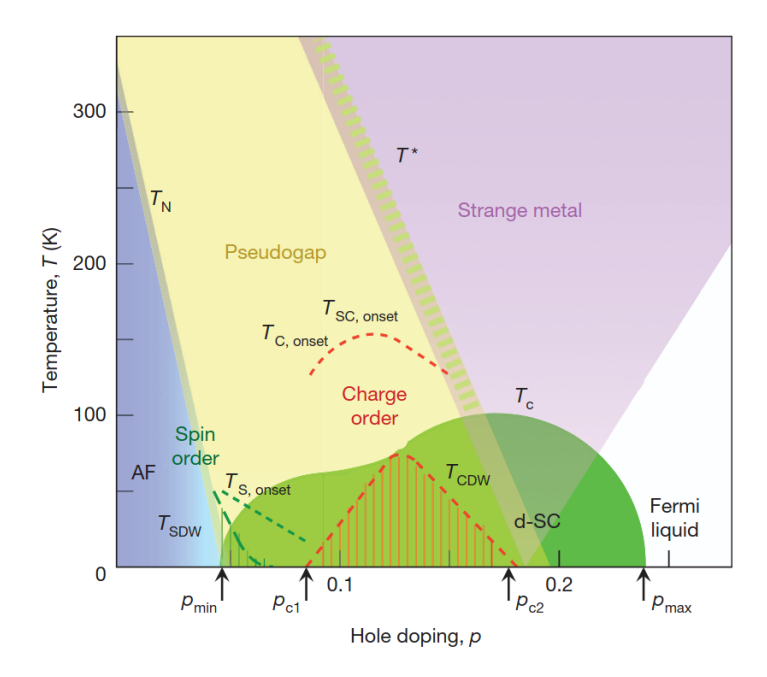


Figure 1.3: Generic phase diagram of a hole-doped cuprate superconductor. [3]

ilar spectral signature is also seen in the adjacent pseudogap regime, characteristic of the cuprates. Both regimes are characterized by a significant decrease in the density of states near the Fermi level, but a true gap is present in neither—the spectrum is gapped only in certain areas of the Brillouin zone. ARPES studies have revealed that the Fermi surface becomes discontinuous as a function of crystal momentum k, forming Fermi arcs which shrink further with decreasing temperature. Below the superconducting temperature  $T_c$  the arcs become points at the  $d_{x^2-y^2}$  nodes (Fig. 1.4). [3, 16]

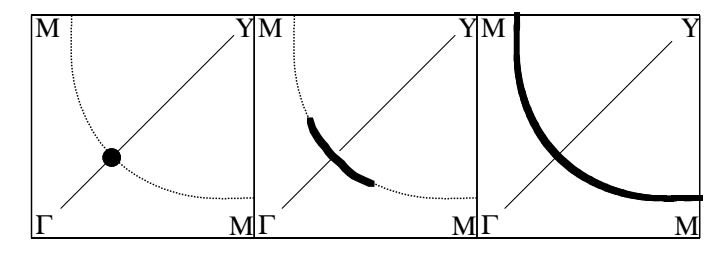


Figure 1.4: An illustration of the cuprate Fermi surface, with temperature increasing from left to right [16]

Unconventional superconductivity was also observed in some organic compounds, including charge transfer salts (BEDT-TTF)<sub>2</sub>X. These salts are formed from conducting layers of BEDT-TTF (bis(ethylenedithio)tetrathiafulvalene) separated by insulating anion layers such as  $X=Cu_2(CN)_3$ . Charge is transferred from the conducting to the ionic layers, leaving the BEDT-TTF with a half-filled band. In the  $\kappa$  phase, the BEDT-TTF molecules are dimerized and are arranged in a triangular lattice (Fig. 1.5). The phase diagram of  $\kappa$ -organics (Fig. 1.6) is qualitatively similar to that

of the cuprates, with pressure taking the place of doping. This indicates that there is a degree of universality in the strongly-correlated behaviour of these systems. [21, 22]

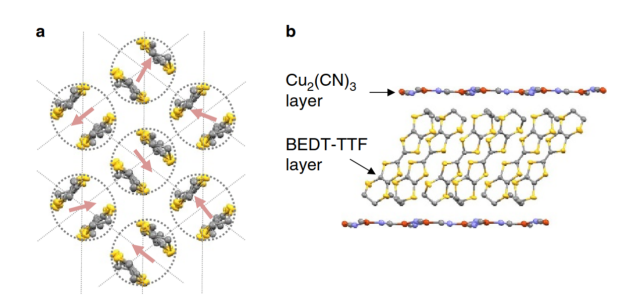


Figure 1.5:  $\kappa$ -(BEDT-TTF)<sub>2</sub>Cu<sub>2</sub>(CN)<sub>3</sub> crystal structure. (a) Top-down view of the conductive layer. (b) Side-view of the 2d layered structure. [23]

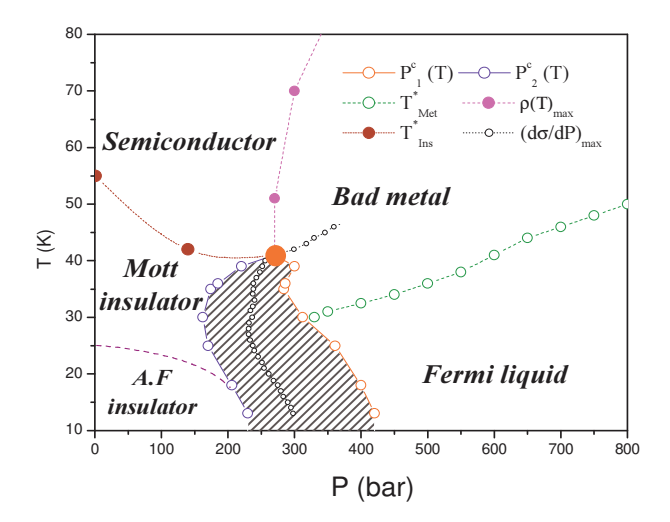


Figure 1.6:  $\kappa$ -(BEDT-TTF)<sub>2</sub>Cu[N(CN)<sub>2</sub>]Cl phase diagram with the superconducting phase ( $T_c$  of 13K) omitted. The shaded area represents a region of coexistence of insulating and metallic phases. [21]

The Hubbard model represents one of the simplest interacting lattice models, characterized by an on-site electron-electron interaction U and intersite hopping terms  $J_{ij}$ . Despite its simplicity, the presence of an interaction makes solving the Hubbard model a quantum many-body problem, and there are very few numerically exact solutions. The infinite-dimensional Hubbard model is exactly solvable by dynamical mean field theory (DMFT). In this limit, the phase diagram displays a first-order Mott metal-insulator transition at finite temperature. This is in qualitative agreement with the experimentally observed transition in vanadium oxide and  $\kappa$ -organics. [23, 24]. A wide range of approximate methods have also been applied to the Hubbard model, indicating the presence of regions with d-wave superconductivity, charge and spin order, bad metal and other phases present in cuprates and organic superconductors

(Fig. 1.7) [25, 26]. For this reason, understanding the Hubbard model and its phase diagram is directly relevant to the study of strongly correlated electron materials.

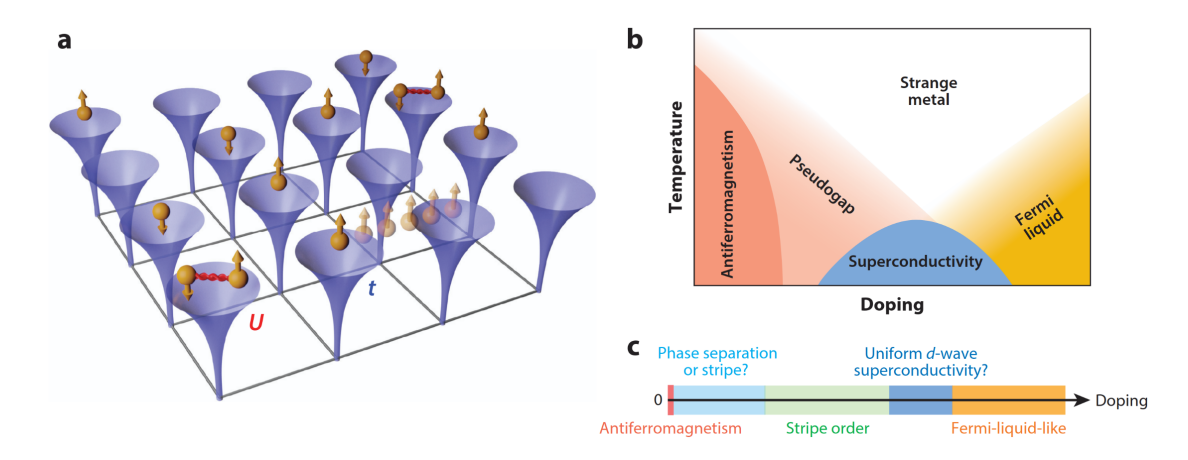


Figure 1.7: (a) Graphical representation of the Hubbard model. Proposed phase diagrams at (b) finite and (c) zero temperature [25]

Dynamical correlation functions in the Hubbard model (and other lattice models) have proven particularly challenging to compute. Imaginary-time methods, such as determinant quantum Monte Carlo (DQMC) rely on analytic continuation, which is poorly defined and introduces uncontrolled error. Exact diagonalization methods, such as the finite-temperature Lanczos method (FTLM) can directly compute these quantities, but are limited to high temperatures and either uniform or short-range correlators due to the small size of lattices that can be treated with these methods. Development of new methods to compute the dynamical correlation functions is therefore one of the primary goals in the field. [25, 27–31]

The study of the Hubbard model (and the related lattice models) is also possible by means of quantum simulation, in experiment. Advances in the field of cold atoms have allowed for the experimental realization of a wide variety of model Hamiltonians on optical lattices, allowing one to directly compare numerical results to experimental data. The lattice parameters are tunable. The optical lattice approach allows one to isolate the effects of electron-electron interactions from other scattering mechanisms (electron-phonon interactions, disorder) which are necessarily present in real materials. In optical lattices the role of fermions is taken up by individual atoms with masses thousands of times larger than the electron, resulting in much slower dynamics. This allows for the study of dynamic correlations with a high time-resolution. These factors make optical lattices an excellent way to both study the relevant physics and benchmark new and existing numerical methods. [32, 33]

However, the electrical resistivity  $\rho$  is not yet directly measurable in cold atom experiments, and the comparison the with theoretical resistivity results has, so far, been only indirect—the resistivity in experiment was deduced from charge response measurements. These experiments probe the response to an applied electric field at long wavelengths. This response can be related to the dc-resistivity via hydrodynamic theory and the Nernst-Einstein relation [27]. The dynamics at long wavelengths are

inaccessible to the presently available numerical methods—imaginary-time methods run into the problem of analytic continuation, and exact diagonalization methods are generally limited to 4x4 clusters, which is far too small to observe the wavelengths of interest.

In this thesis, we introduce the open quantum cluster embedding theory (OQCET), a real-time embedded cluster method that is able to access long-wavelength response without analytic continuation. This allows us to perform a direct comparison with the existing measurements in a cold atom experiment.

The method follows the strategy of other embedded cluster methods. Two sets of equations are solved self-consistently - the equations governing the lattice quantities are closed by short-range correlators computed in small effective clusters; in turn, the small clusters are tuned so as to mimic the dynamics of the large lattice. Namely, the small clusters are open quantum clusters, evolving per the Linblad equation, and their tuning is done via a time-dependent coupling to an external environment. The lattice equations are equations of motion for the fermionic bilinear and the local double occupancy, but additional quantities can also be used. The method is trivial in equilibrium: the starting point of the method is a solution for the instantaneous correlators extracted from a lattice QMC calculation, which requires no analytic continuation; in the absence of external fields, the OQCET equations yield no additional information. The dynamical response functions are obtained by probing the system using weak external fields, and then inverting the linear-response theory equations. The method has certain desirable properties, such a fulfillment of the total charge and energy conservation; it becomes exact in the non-interacting and zero-hopping limits, as well in the limit of infinite cluster size.

The thesis is organized as follows. In Chapter 2 we give a brief overview of the general methodology of numerical method development. We introduce the concept of embedded cluster theories, giving a brief derivation of DMFT and its cluster extensions as an example. In Chapter 3 we introduce OQCET in analogy to DMFT, and discuss implementation details. We consider several variants of the method, with respect to a) how the initial density matrices and the Hamiltonians for the clusters are set up, b) what the jump operators for the coupling to the environment are, c) what the constrained operators are (the quantities on the cluster that mimic the large lattice), d) how exactly we drive the system out of equilibrium and e) how big the cluster size is. In Chapter 4 we benchmark our method against known results, and finally directly compare to the experimental findings. We observe good qualitative agreement between theory and experiment, in terms of temperature and wavelength dependence trends. Further work is needed to implement the theory for larger clusters, and to generalize the approach to other dynamical susceptibilities and the spectral function.

# Chapter 2

# General methodology

The current, widely accepted paradigm for numerical method development puts emphasis on *controlled* theories. A theory is controlled if there exists a series of systematic corrections which reduce the level of approximation, eventually leading to an exact solution. The degree of approximation is quantified by introducing the notion of a *control parameter*. Since we often make multiple controlled approximations, a theory may have more than one control parameter. As a control parameter approaches a limiting value, the approximation associated with this parameter reduces. As all control parameters in a theory approach their associated limits, the theory becomes numerically exact.

There are three general families of controlled approaches: finite lattice, perturbative expansion and embedded cluster methods.

Finite lattice methods such as the finite-temperature Lanczos method (FTLM) and lattice quantum Monte Carlo (QMC) have lattice size as a control parameter. Quantities are calculated on smaller lattice sizes and extrapolated to the thermodynamic limit. Lattice QMC methods such as CTINT [34] and CTAUX [35] can treat larger lattices than FTLM, but are limited to calculating static quantities as they are formulated in imaginary time. These methods also have an additional control parameter: the number of Monte Carlo steps performed, which is associated with the statistical error.

Perturbative methods calculate quantities by expansion in terms of the powers of some model parameter, such as the interaction strength, (inverse) temperature, etc. The expansion is truncated at finite order n, which represents the control parameter. The requirement that the perturbative series converges generally limits interaction-expansion methods to low values of the coupling, but there has been recent progress in pushing these methods to intermediate interaction strength [36].

In embedded cluster methods, the idea is to create an exactly solvable representative model by only taking a small subset of the degrees of freedom of the original model. This representative model is then coupled to an effective field. The parameters of the effective field are determined in a self-consistent manner by a set of lattice equations.

When studying transport phenomena, it is particularly important to ensure conservation of quantities such as charge and energy, as transport equations that do not

conserve these quantities can exhibit unphysical behavior. One way to ensure that conservation laws are satisfied is to rely on Luttinger-Ward functional (LWF) derivable theories. It has been shown that theories derived as an approximation of the LWF obey conservation laws. [37, 38]

Figure 2.1: Diagrammatic expansion of the Luttinger-Ward functional and the self energy in terms of the full Green's function G. [39]

Diagrammatically, the LWF is defined as the sum of all irreducible two-particle skeleton partition function diagrams Fig. 2.1. The LWF can be related to the grand potential (the Landau free energy) as

$$\Omega[\mathbf{G}] = \operatorname{Tr} \ln \mathbf{G} - \operatorname{Tr}((\mathbf{G}_0^{-1} - \mathbf{G}^{-1})\mathbf{G}) + \Phi[\mathbf{G}]$$
(2.1)

where  $G_0$  is the bare Green's function and  $\Phi[G]$  is the LWF. The self energy can be obtained from the LWF as a functional of G

$$\frac{\delta\Phi[\mathbf{G}]}{\delta\mathbf{G}} = T\Sigma[\mathbf{G}] \tag{2.2}$$

where T is the temperature. We recover the well-known Dyson equation by looking at the stationary point of the free energy,  $\delta\Omega/\delta\mathbf{G} = 0$ 

$$\mathbf{G}^{-1} - \mathbf{G}_0^{-1} - \mathbf{\Sigma}[\mathbf{G}] = 0 \tag{2.3}$$

Self-consistent Hartree-Fock and dynamical mean field theory (DMFT) are both examples of LWF-derivable theories. Hartree-Fock is obtained by approximating the LWF with only the first term in Fig. 2.1 [40]. Restricting the domain of the full functional to local Green's functions gives us the DMFT approximation. By including certain non-local components of Green's functions (such as nearest-neighbor components) we arrive at cluster extensions of DMFT.

Similar formulations using related functionals also exist, such as the self energy functional by Potthoff et al. [41] and the Almbladh functional [42].

Another important property of the LWF is universality—the form of the functional is determined by the interacting part of the Hamiltonian, and is independent of the bare Green's function. This allows us to approach the problem by solving an auxiliary problem with the same interaction and at the same temperature. This connection between lattice models and associated "impurity" problems is the essence of embedded cluster theories. [39]

### 2.1 Embedded cluster methods

To create an accurate picture of strongly correlated materials, we need to be able to treat local interacting physics as well as more delocalized coherent phenomena. Embedded cluster theories provide a framework to do so—by connecting lattice equations to clusters in which interactions are treated numerically exactly, we can capture both local and delocalized effects.

We will outline the prescription for creating an embedded cluster theory. First, we create a representative model from a small subset of lattice degrees of freedom. This model should be small enough to be exactly solvable. After choosing a representative model, we choose some lattice quantity of interest (in DMFT this would be the Green's function). We will refer to these quantities as the constrained quantities. Next, we write down lattice equations to express the constrained quantities. These equations will in general depend on some other quantities, which we will refer to as representative quantities. The equations are closed by taking values of representative quantities from the representative model. To relate the representative model and the lattice, we introduce a self-consistency condition: the representative model is coupled to an effective field, with the field parameters chosen such that the cluster constrained quantities match the lattice constrained quantities Fig. 2.2.

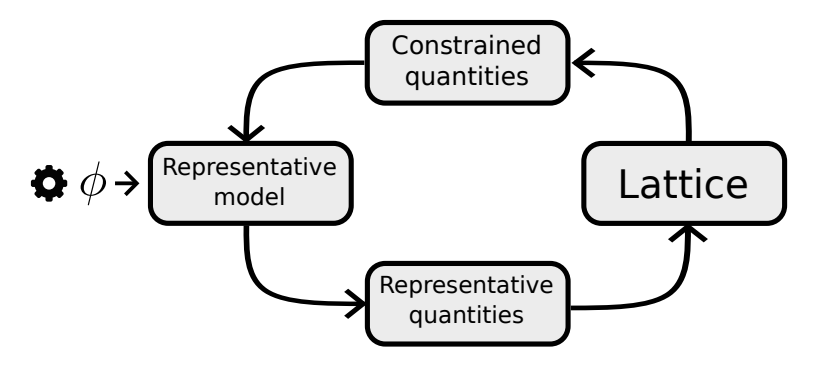


Figure 2.2: The self-consistency relation in embedded cluster theories. Coupling to the representative model is represented by the field  $\phi$ .

# 2.2 Dynamical mean-field theory (DMFT)

The LWF formalism provides a powerful framework for proving conservation laws. However, there are other ways to ensure conservation laws in embedded cluster methods. We will introduce OQCET in analogy to DMFT, so we start by recapitulating the derivation of DMFT following [1] and provide an overview of its cluster extensions.

### 2.2.1 Single site DMFT for the Hubbard model

We start with the Hubbard Hamiltonian with hopping term J, interaction U and chemical potential  $\mu$ 

$$H = -J \sum_{\langle i,j\rangle,\sigma} c_{i\sigma}^{\dagger} c_{j\sigma} - \mu \sum_{i,\sigma} n_{i\sigma} + U \sum_{i} n_{i\uparrow} n_{i\downarrow}$$
 (2.4)

where i and j denote lattice sites,  $\langle i, j \rangle$  indicates the sum should be performed over nearest neighbor pairs, and  $c^{\dagger}$  and c are fermionic creation and annihilation operators, with  $n \equiv c^{\dagger}c$ . In DMFT, the quantity of interest is the local Green's function

$$G_{\sigma,ii}(\tau) = -\left\langle \mathcal{T}c_{\sigma,i}(\tau)c_{\sigma,i}^{\dagger}(0)\right\rangle \tag{2.5}$$

where  $\mathcal{T}$  is the time-ordering operator. The lattice local Green's function can be mapped onto the Green's function of the representative model, which is in this case the single impurity Anderson model (SIAM)

$$H_{\text{SIAM}} = H_{\text{imp}} + H_{\text{bath}} + H_{\text{hyb}} \tag{2.6}$$

$$H_{\rm imp} = U n_{\uparrow}^c n_{\downarrow}^c - \mu (n_{\uparrow}^c + n_{\downarrow}^c) \tag{2.7}$$

$$H_{\text{bath}} = \sum_{\lambda} \varepsilon_{\lambda}^{d} d_{\lambda\sigma}^{\dagger} d_{\lambda\sigma}$$
 (2.8)

$$H_{\text{hyb}} = \sum_{\lambda} V_{\lambda} (d_{\lambda\sigma}^{\dagger} c_{\sigma} + c_{\sigma}^{\dagger} d_{\lambda\sigma})$$
 (2.9)

Where we have introduced a set of non-interacting fermions  $d_{\lambda}$  coupled to the impurity orbital c, parametrized by  $V_{\lambda}$  and  $\varepsilon_{\lambda}^{d}$ . The d-states  $\lambda$  present the "bath" that the impurity is coupled to. The noninteracting Green's function of the impurity can be shown to be

$$G_{0,\text{imp}}^{-1}(i\omega_n) = i\omega_n + \mu - \Delta(i\omega_n)$$
(2.10)

where

$$\Delta(i\omega_n) = \sum_{\lambda} \frac{|V_{\lambda}|^2}{i\omega_n - \varepsilon_{\lambda}^d}$$
 (2.11)

is the hybridization function.

The impurity local self-energy is defined as

$$\Sigma_{\rm imp}(i\omega_n) = G_{0\,\rm imp}^{-1}(i\omega_n) - G_{\rm imp}^{-1}(i\omega_n)$$
(2.12)

On the lattice, the full Green's function is

$$G_{\text{latt}}(\mathbf{k}, i\omega_n) = \frac{1}{i\omega_n + \mu - \varepsilon(\mathbf{k}) - \Sigma_{\text{latt}}(\mathbf{k}, i\omega_n)}$$
(2.13)

where  $\varepsilon(\mathbf{k})$  is the noninteracting dispersion

$$\varepsilon(\mathbf{k}) = -2J(\cos k_x + \cos k_y) \tag{2.14}$$

The approximation we make in DMFT is that the lattice self-energy is purely local and equal to the impurity self-energy, i.e.  $\Sigma_{ij,\text{latt}}(i\omega_n) = \delta_{i,j}\Sigma_{\text{imp}}(i\omega_n)$ , so its spatial Fourier transform is **k**-independent

$$\Sigma_{\mathbf{k},\text{latt}} = \sum_{\mathbf{r}} e^{i\mathbf{k}\cdot\mathbf{r}} \delta_{\mathbf{r},0} \Sigma_{\text{imp}}(i\omega_n) = \Sigma_{\text{imp}}(i\omega_n)$$
 (2.15)

Summing Eq. (2.13) over  $\mathbf{k}$  to obtain the local Green's function we arrive at the self-consistency condition

$$\sum_{\mathbf{k}} G_{\text{latt}}(\mathbf{k}, i\omega_n) = G_{\text{imp}}(i\omega_n)$$
 (2.16)

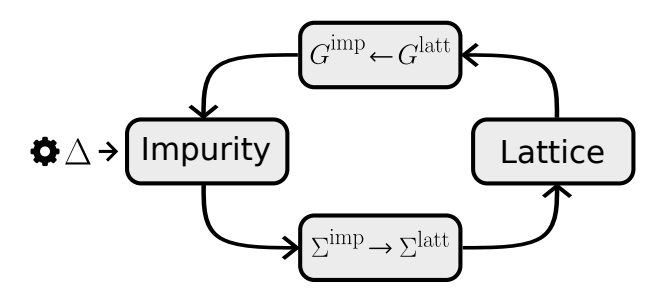


Figure 2.3: DMFT self-consistent loop.

In practice, the DMFT self-consistent equations are usually solved by an iterative procedure (Fig. 2.3). Starting from an initial guess for  $\Delta(i\omega_n)$ , we solve the impurity problem to calculate  $G_{\rm imp}(i\omega_n)$  and the impurity self-energy  $\Sigma_{\rm imp}(i\omega_n)$  (Eq. (2.12)). The local lattice Green's function is then calculated from Eq. (2.13), with the local self-energy taken from the impurity ( $\Sigma_{\rm latt}(\mathbf{k}, i\omega_n) = \Sigma_{\rm imp}(i\omega_n)$ ):

$$G_{\text{latt}}^{\text{loc}}(i\omega_n) = \frac{1}{N} \sum_{\mathbf{k}} G_{\text{latt}}(\mathbf{k}, i\omega_n) = \frac{1}{N} \sum_{\mathbf{k}} \frac{1}{i\omega_n + \mu - \varepsilon(\mathbf{k}) - \Sigma_{\text{imp}}(i\omega_n)}$$
(2.17)

Updating our guess for the hybridization function,

$$\Delta(i\omega_n) = i\omega_n - \mu - \left[G_{\text{latt}}^{\text{loc}}(i\omega_n)\right]^{-1} - \Sigma_{\text{imp}}(i\omega_n)$$
 (2.18)

we begin a new iteration of the loop. The procedure is repeated until the loop converges, and the self-consistency condition Eq. (2.16) is satisfied.

DMFT becomes exact in several limits:

- 1. In the non-interacting limit (U=0) the self-energy vanishes, so the local self energy assumption becomes trivially exact:  $\Sigma(\mathbf{k}, i\omega_n) = \Sigma(i\omega_n) = 0$
- 2. In the atomic limit (J=0) the lattice becomes a set of isolated Hubbard atoms, with the self-energy necessarily being purely local. The DMFT solution is then trivially  $\Delta(i\omega_n) = 0$  as that describes a single isolated impurity.

3. In the infinite lattice coordination limit (limit of infinite dimension) it can also be shown that the self-energy becomes local.

The local self-energy approximation is not justified in many cases, so extensions to the original theory have been developed. The family of cluster DMFT methods improve on the original by introducing non-local components to the self-energy. While these extensions represent systematic corrections of DMFT, they all approach the exact solution by different paths. Below we present a brief overview of several cluster DMFT methods following [43].

#### 2.2.2 Cluster DMFT

#### Cellular DMFT (CDMFT)

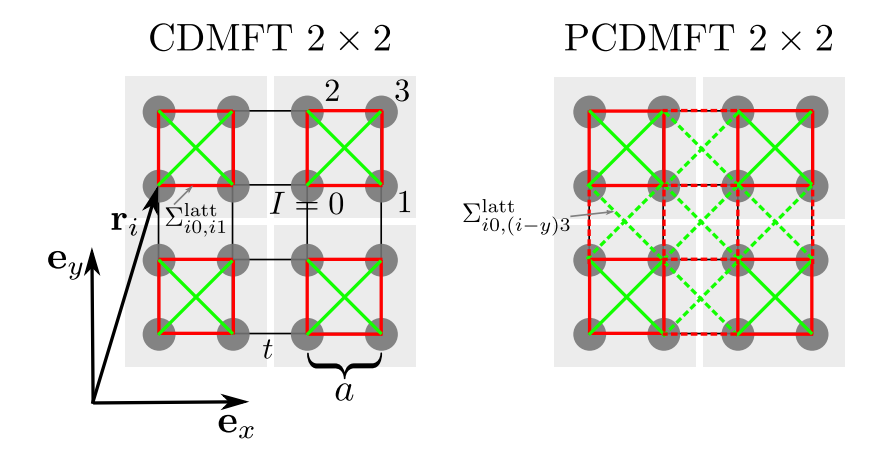


Figure 2.4: Comparison of CDMFT and PCDMFT schemes, supercells are shaded gray. In CDMFT the self-energies are zero on bonds between supercells, while in PCDMFT the inter-cell self-energies are pasted on by symmetry (dashed lines). [43]

In CDMFT, we divide the model lattice into supercells. In this notation, the Green's function depends on two sets of indices

$$G_{ij} \to G_{IJ,ij}$$

where I, J are supercell indices, and i, j are now indices of sites within the supercell. The LWF approximation then consists of restricting the domain to the set of Green's functions within one supercell

$$\Phi\left[\sum_{I,I}\sum_{i,j\in s.c.}G_{IJ,ij}\right]\approx\Phi\left[\sum_{I}\sum_{i,j\in s.c.}G_{II,ij}\right]$$
(2.19)

In this case, the self-consistency condition reads

$$\hat{G}^{\text{imp}} = \hat{G}_{II}^{\text{latt}} = \frac{1}{N} \sum_{K \in \text{RBZ}} \hat{G}_{\mathbf{K}}^{\text{latt}}$$
(2.20)

where RBZ denotes the reduced Brillouin zone and N represents the number of unit cells. Unfortunately, this approach breaks translation symmetry, as the self-energy is only nonzero within the supercells (Fig. 2.4). This can be resolved by post-processing—the lattice self-energy between clusters can be recovered from the impurity self-energy by symmetry, and we recover a translationally invariant Green's function. This symmetrization cannot be interpreted as an approximation of the LWF, and the choice of quantity to periodize yields, in general, different results.

Alternatively, in periodic cellular DMFT (PCDMFT), the lattice self-energy is symmetrized in each iteration of the DMFT loop, and the resulting  $G^{\text{latt}}$  is translationally invariant (Fig. 2.4). This removes the need for an additional post-processing step, but PCDMFT cannot be derived as a LWF approximation.

#### Dynamical cluster approximation (DCA)

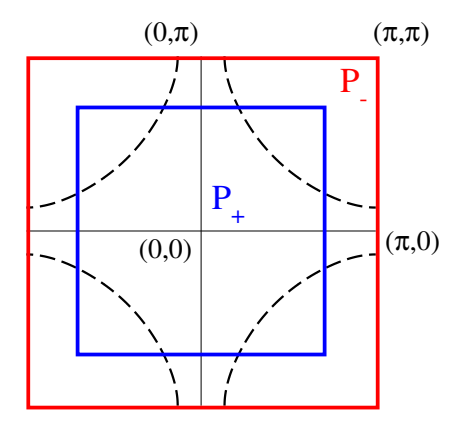


Figure 2.5: A simple DCA scheme, with the Brillouin zone divided into two patches,  $P_{+}$  (inside the blue square) and  $P_{-}$  (between the blue and red squares). [44]

DCA is realized through a coarse-graining of the Brillouin zone (Fig. 2.5). The LWF is approximated as

$$\Phi[\{G_{\mathbf{k}}\}_{\forall \mathbf{k}}] \approx \Phi\left[\left\{\sum_{\mathbf{k} \in \mathcal{P}(\mathbf{K})} G_{\mathbf{k}}\right\}_{\forall \mathbf{K}}\right] \equiv \Phi[\{G_{\mathbf{K}}\}_{\forall \mathbf{K}}]$$
(2.21)

where  $\mathbf{k}$  and  $\mathbf{K}$  are fine- and coarse-grained vectors of the BZ respectively. In the simplest case,  $\mathcal{P}(\mathbf{K})$  represents the set of vectors  $\mathbf{k}$  closest to  $\mathbf{K}$  (the Voronoi patch of  $\mathbf{K}$ ). The self-energy is then piecewise constant in  $\mathbf{k}$ , as

$$\frac{\Phi[\{G_{\mathbf{K}}\}_{\forall \mathbf{K}}]}{\partial G_{\mathbf{k}}} = \frac{\Phi[\{G_{\mathbf{K}}\}_{\forall \mathbf{K}}]}{\partial G_{\mathbf{K}}} \delta_{\mathbf{k} \in \mathcal{P}(\mathbf{K})}$$
(2.22)

The DCA impurity is then a cyclic cluster with wavevectors  $\mathbf{K}$ , and the self-consistency condition is

$$G_{\mathbf{K}}^{\mathrm{imp}}(i\omega_n) = G_{\mathbf{K}}^{\mathrm{latt}}(i\omega_n) = \frac{1}{N_{\mathcal{P}(\mathbf{K})}} \sum_{\mathbf{k} \in \mathcal{P}(\mathbf{K})} G_{\mathbf{k}}^{\mathrm{latt}}(i\omega_n)$$
(2.23)

where  $N_{\mathcal{P}(\mathbf{K})}$  is the number of fine-grained **k**-vectors in the Voronoi patch of **K**. The lattice self-energy is given as

$$\Sigma_{\mathbf{k}}^{\text{latt}} = \Sigma_{\mathbf{K}(\mathbf{k})}^{\text{imp}} \tag{2.24}$$

where  $\mathbf{K}(\mathbf{k})$  is a function that gives the coarse-grained vector nearest to  $\mathbf{k}$ .

#### Nested cluster scheme (NCS)

The nested cluster scheme [43] represents a real-space method that simultaneously preserves both the translation invariance and the continuity of the self-energy in k-space. Unlike in (P)CDMFT, this is done at the level of the LWF approximation. We start from the idea that the Luttinger-Ward functional can be approximated as a sum of cluster functionals, with clusters C chosen as subsets of lattice sites

$$\Phi[G] \approx \sum_{C \in \mathcal{C}} \Phi_C[G_C] \tag{2.25}$$

where C is the set containing all clusters. The clusters in C are chosen such that they cover the entire lattice,

$$\bigcup_{C \in \mathcal{C}} C = \mathcal{L} \tag{2.26}$$

and that they are independent

$$C \not\subset C' \quad \forall C, C' \in \mathcal{C}$$
 (2.27)

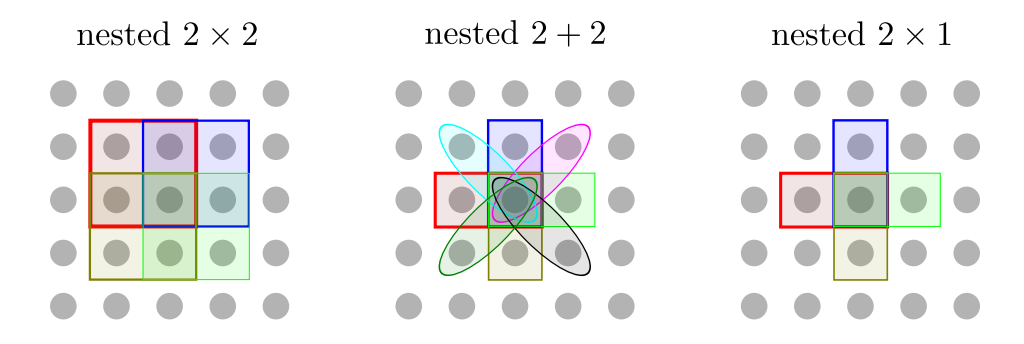


Figure 2.6: Simple cluster nesting schemes [43]

Since we preserve translation invariance, the clusters in  $\mathcal{C}$  necessarily overlap (Fig. 2.6), so we have to account for the double counting of diagrams involving orbitals present in multiple clusters. To correct for this, we can write the LWF with an additional term

$$\Phi[G] \approx \sum_{C \in \mathcal{C}} \Phi_C[G_C] + \sum_{C \in \mathcal{O}} p_C \Phi_C[G_C]$$
 (2.28)

where  $\mathcal{O}$  contains all the overlaps between the clusters.  $p_C$  are integers chosen to cancel out the double counted diagrams. This means that it will be necessary to

solve impurity problems of clusters in both the original set  $\mathcal{C}$  and the overlap set  $\mathcal{O}$ . In the NCS, both the set of overlapping clusters  $\mathcal{O}$  and the factors  $p_C$  are determined by the initial choice of  $\mathcal{C}$ . Defining  $p_{C\in\mathcal{C}}=1$ , we can rewrite Eq. (2.28) as

$$\Phi[G] \approx \sum_{C \in \mathcal{C} \cup \mathcal{O}} p_C \Phi_C[G_C] \tag{2.29}$$

To distinguish between lattice and cluster indices, lattice indices will be referred to in vector notation (e.g.  $\Sigma_{\mathbf{r},\mathbf{r}'}^{\text{latt}}$ ), and i,j... will be used for cluster indices (e.g.  $\Sigma_{i,j}^{\text{imp C}}$ ). The self-consistency condition reads

$$G_{i,j}^{\text{imp C}} = G_{\mathbf{r}(i,C),\mathbf{r}(j,C)}^{\text{latt}}$$
 (2.30)

where  $\mathbf{r}(i, C)$  is a function that maps site i on cluster C to its corresponding lattice vector. The lattice self-energy is given by

$$\Sigma_{\mathbf{r},\mathbf{r}'}^{\text{latt}} = \sum_{C \supset \mathbf{r},\mathbf{r}'} p_C \Sigma_{i_C(\mathbf{r}),i_C(\mathbf{r}')}^{\text{imp C}}$$
(2.31)

where  $i_C(\mathbf{r})$  maps lattice vector  $\mathbf{r}$  to the site i on cluster C.

# 2.3 Linear response theory

Linear response theory provides a connection between dynamic correlation functions and system response to a weak external perturbation. To derive the linear response equations we follow [45, 46].

In the Schrödinger picture, the expectation value of operator A is defined as

$$\langle A \rangle = \text{Tr}(\rho A) \tag{2.32}$$

In equilibrium, the density matrix  $\rho$  is a thermal ensemble

$$\rho = e^{\beta H_0} / \text{Tr}(e^{\beta H_0}) \tag{2.33}$$

where  $H_0$  is the unperturbed system Hamiltonian. We now introduce an external perturbation H' at time  $t = t_0$ . The total Hamiltonian then becomes

$$H(t) = H_0 + V(t)\theta(t - t_0)$$
(2.34)

Here it will be useful to work in the interaction picture. Operators in the interaction picture will be denoted with a hat, e.g.  $\hat{V}(t)$ . For the interacting Hamiltonian we choose  $\hat{H}' = V(t)\theta(t-t_0)$  The evolution operator U is given as

$$\hat{U}(t,t_0) = 1 + \frac{1}{i} \int_{t_0}^t dt' \hat{H}'(t') \hat{U}(t',t_0)$$
(2.35)

Approximating the above expression to first order in  $\hat{H}'$  we get

$$\hat{U}(t,t_0) \approx 1 + \frac{1}{i} \int_{t_0}^t dt' \hat{H}'(t')$$
 (2.36)

In the interaction picture, states and operators evolve as follows:

$$|\hat{\psi}(t)\rangle = \hat{U}(t, t_0)e^{iH_0t} |\psi(t_0)\rangle \tag{2.37}$$

$$\hat{A}(t) = e^{iH_0t} A e^{-iH_0t} \tag{2.38}$$

It can be shown that the expectation value Eq. (2.32) then evolves as

$$\langle A(t) \rangle = \langle A \rangle_0 - i \int_{t_0}^t dt' \frac{1}{Z_0} \sum_n e^{-\beta E_n} \langle n(t_0) | \hat{A}(t) \hat{H}'(t') - \hat{H}'(t') \hat{A}(t) | n(t_0) \rangle$$

$$= \langle A \rangle_0 - i \int_{t_0}^t dt' \langle [\hat{A}(t), \hat{V}(t')] \rangle_0$$

$$= \langle A \rangle_0 + \int_{t_0}^\infty dt' C_{AV}^R(t, t')$$
(2.39)

where  $\langle A \rangle_0$  denotes the equilibrium thermal average  $(H = H_0)$  and

$$C_{AV}^{R}(t,t') = -i\theta(t-t')\langle [\hat{A}(t),\hat{V}(t')]\rangle_{0}$$
(2.40)

is a general retarded correlation function. We can note here that the Heisenberg and interaction pictures coincide for  $\langle \cdots \rangle_0$  as H' = 0. If the perturbation can be written as a time-dependent classical field F(t) coupled to an operator B

$$V(t) = F(t)B (2.41)$$

the linear response equation becomes

$$\langle A(t)\rangle = \langle A\rangle_0 + \int_{t_0}^t dt' \chi_{AB}(t, t') F(t')$$
 (2.42)

where

$$\chi_{AB}(t,t') = -i\theta(t-t')\langle [\hat{A}(t),\hat{B}(t')]\rangle_0 \tag{2.43}$$

is a general retarded susceptibility. As the system was originally in equilibrium, we can rewrite the above as

$$\chi_{AB}(t,t') = \chi_{AB}(t-t')$$
(2.44)

If the field F(t) is of an appropriate form (a delta-like function, for example) then Eq. (2.42) can be inverted easily, and the susceptibility can be calculated from the non-equilibrium response. This approach is referred to as *inverse linear response theory* [28].

# Chapter 3

# OQCET as an embedded cluster method

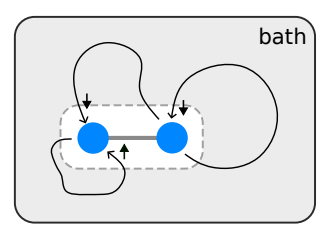
In this chapter we will introduce OQCET as an embedded cluster method in analogy to DMFT. After outlining the general formalism, we derive the OQCET equations for charge response in the square lattice Hubbard model.

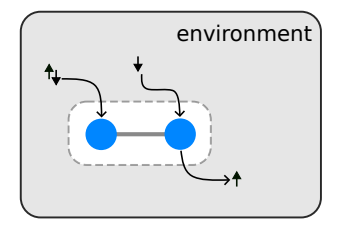
In OQCET, the role of the representative model is taken up by an open quantum cluster governed by the Lindblad equation [47]. Like the Anderson impurity model in DMFT, Lindbladian evolution allows for particles to enter and leave the clusters. Beyond what is usually considered in the SIAM, in our open clusters we will also consider more complicated couplings with the environment. In the AIM, the particles in the bath behave according the bare-propagator  $\Delta$ . In Lindbladian evolution the particles entering the cluster have no memory of their previous state (Fig. 3.1). As a result, the Lindblad equation is Markovian—the future evolution of the system only depends on its current state [47]. In practice, this means that it is only necessary to store data in working memory for the current time step. Therefore, the memory requirements for non-equilibrium calculations remain constant with the number of time steps  $n_t$  and the cpu-time scales as  $O(n_t)$ . This contrasts with other methods such as non-equilibrium DMFT [48], where both memory usage and cpu-time scale as  $O(n_t^2)$ . Significantly lower memory and processing power requirements make it feasible to perform calculations to very long times. The coupling to the bath in DMFT is described and tuned by the 2-time propagator  $\Delta(t, t')$ , while in the Lindblad equation we tune the single-time dependence of the coupling constants  $\Gamma(t)$ .

As already noted, embedded cluster theories are formulated by coupling two sets of equations—one for the lattice, and one for the embedded clusters. In DMFT, the lattice equation is the Dyson equation expressing the Green's function from the self-energy and the lattice Hamiltonian; the cluster equations are the solution for the self-energy with respect to the cluster action, which depends on the hybridization function  $\Delta$ .

In OQCET, the lattice equations are equations of motion for expectation values of constrained operators. The expectation values (EVs) of lattice operators evolve by the Heisenberg equation

$$\partial_t \langle A(t) \rangle = i \langle [H(t), A(t)] \rangle$$
 (3.1)





effective Anderson impurity problem

Lindbladian open cluster

Figure 3.1: Schematic representation of the Anderson impurity model and a Lindbladian open quantum cluster

In general (due to two-particle terms in the Hamiltonian), the set of operator expectation values  $\{\langle A_{\lambda} \rangle\}$  will not yield closed equations of motion (EOM), and the EOM will also depend on some set  $\{\langle B_{\lambda} \rangle\}$ .

$$\partial_t \langle A_{\lambda}(t) \rangle = f\left(\{\langle A_{\mu} \rangle\}, \{\langle B_{\mu} \rangle\}\right) \tag{3.2}$$

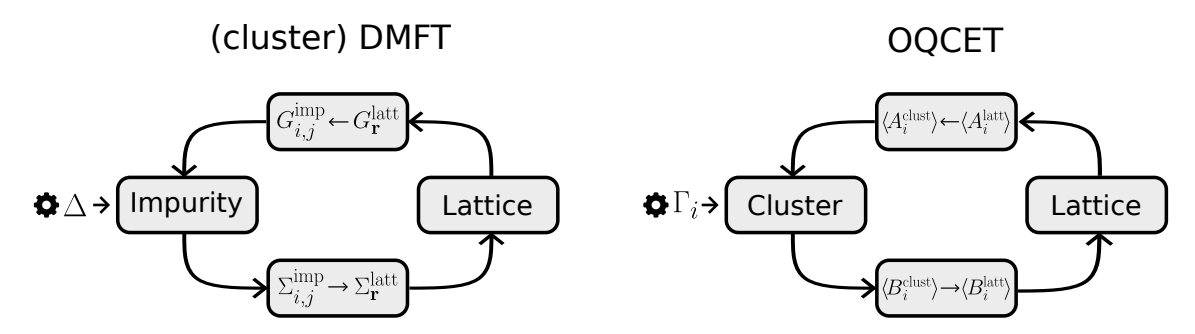


Figure 3.2: Schematic comparison of the DMFT and OQCET loops. Quantities in the top boxes are imposed onto the representative model, while quantities at the bottom are extracted from the representative model and passed onto the lattice equations.

In OQCET the equations of motion for the set of lattice operator EVs  $\{\langle \hat{A}^{\text{latt}}_{\lambda} \rangle\}$  will be closed by  $\{\langle \hat{B}^{\text{latt}}_{\lambda} \rangle\}$  computed within the clusters, using a mapping between cluster and lattice sites. Here the 'hat' symbol denotes that  $\hat{A}^{\text{latt}}_{\lambda}$  and  $\hat{B}^{\text{latt}}_{\lambda}$  are tensors of real space vectors  $\mathbf{r}$ . These tensors can be of arbitrary rank, e.g. the bilinear  $c^{\dagger}_{\mathbf{r}\sigma}c_{\mathbf{r}'\sigma}$  is a rank two tensor and the local double occupancy operator  $n_{\mathbf{r}\uparrow}n_{\mathbf{r}\downarrow}$  is of rank one.

Clusters in OQCET are formed by restricting the single-particle lattice Hilbert space to a subspace containing a small set of lattice sites. For example, a cluster can be formed from two neighboring lattice sites with vectors  $\mathbf{r}$  and  $\mathbf{r} + \mathbf{e}_x$ . In principle, the clusters can be of any shape and the sites need not be connected by nearest-neighbor bonds. The mapping between cluster site indices and lattice vectors is in general many-to-many: clusters can overlap, i.e. sites on different clusters can map to the same lattice vector. If the lattice has symmetries, a single cluster site can map to multiple lattice vectors.

To create a set of clusters we first select the desired cluster shape (for example, 2x1 nearest neighbor clusters) and we tile the lattice with all possible translations and

rotations of those clusters. Next, we use lattice symmetries to select the irreducible set of non-equivalent clusters. On the clusters,  $\{\langle \hat{A}^{\rm clust}_{\lambda} \rangle\}$  and  $\{\langle \hat{B}^{\rm clust}_{\lambda} \rangle\}$  are tensors of cluster site indices  $\{i,j,...\}$ . Since the clusters are small, longer range components of  $\{\langle \hat{B}^{\rm latt}_{\lambda} \rangle\}$  might not have a mapping in the space of cluster operators. For example, if we tile the lattice with two-site nearest-neighbor clusters, a rank two tensor  $\langle B^{\rm latt}_{{\bf r},{\bf r}',\lambda} \rangle$  will not have a mapping if  ${\bf r}$  and  ${\bf r}'$  are not vectors of nearest-neighbor lattice sites. If that is the case, we set those tensor components of  $\{\langle \hat{B}^{\rm latt}_{\lambda} \rangle\}$  to zero.

If the disconnected components of the Wick's theorem decomposition of  $\langle \hat{B}_{\lambda} \rangle$  can be expressed as a product of averages  $\{\langle \hat{A}_{\mu} \rangle\}$ , we can rewrite the equations of motion such that the equations are now closed by the connected average

$$\partial_t \langle A_\lambda(t) \rangle = f\left(\{\langle A_\mu \rangle\}, \{\langle \hat{B}_\mu \rangle^{\text{conn}}\}\right)$$
 (3.3)

With this approach, we instead set the longer range components of  $\{\langle \hat{B}_{\lambda}^{\text{latt}}\rangle^{\text{conn}}\}$  to zero, which is equivalent to taking only the disconnected components of  $\{\langle \hat{B}_{\lambda}^{\text{latt}}\rangle\}$ .

Due to the possibility of cluster overlaps, the procedure for mapping cluster quantities to lattice quantities is, in general, not unique. One way to address this would be to apply the nested cluster scheme discussed in the previous chapter, where we would subtract double counting contributions from clusters formed by overlaps. Another, simpler approach would be to simply average out contributions of overlapping clusters. These approaches will be discussed further in Chapter 4.

The cluster is coupled to an effective environment via the Lindblad equation

$$\frac{d\rho(t)}{dt} = -i[H_{\text{clust}}, \rho(t)] + \sum_{i} \Gamma_{i}(t) \left( L_{i}\rho(t)L_{i}^{\dagger} - \frac{1}{2} \left\{ L_{i}^{\dagger}L_{i}, \rho(t) \right\} \right)$$
(3.4)

where  $L_i$  are 'jump operators' describing the system-environment coupling and  $\Gamma_i$  are positive real numbers representing the coupling strength (analogous to the hybridization function  $\Delta(i\omega_n)$ ). For example, a jump operator  $L=c_{i\sigma}^{\dagger}$  ( $L=c_{i\sigma}$ ) can be interpreted as a particle entering (leaving) the system at site i with spin  $\sigma$ , and the rate at which this happens is determined by the associated  $\Gamma$ . In OQCET, the set of jump operators  $\{L_i\}$  is chosen a priori based on the quantities we wish to calculate, and  $\Gamma_i$  are tuned so that cluster EVs  $\{\langle \hat{A}_{\lambda}^{\text{clust}} \rangle\}$  match lattice EVs  $\{\langle \hat{A}_{\lambda}^{\text{latt}} \rangle\}$  (corresponding to how the hybridization  $\Delta(i\omega_n)$  is set so that the impurity Green's function matches the lattice Green's function in DMFT). The analogy with DMFT is illustrated in Fig. 3.2. The procedure for constructing the cluster Hamiltonian  $H_{\text{clust}}$  will be discussed in a later section.

In OQCET we start from a system prepared in equilibrium. The lattice equilibrium EVs  $\{\langle \hat{A}^{\text{latt}}_{\lambda}(t=0)\rangle\}$  and  $\{\langle \hat{B}^{\text{latt}}_{\lambda}(t=0)\rangle\}$  must be obtained first, preferably employing numerically exact methods. On the clusters, the equilibrium density matrix  $\rho^{\text{clust}}(t=0)$  is prepared such that  $\{\langle \hat{A}^{\text{clust}}_{\lambda}(t=0)\rangle\} = \{\langle \hat{A}^{\text{latt}}_{\lambda}(t=0)\rangle\}$  and  $\{\langle \hat{B}^{\text{clust}}_{\lambda}(t=0)\rangle\} = \{\langle \hat{B}^{\text{latt}}_{\lambda}(t=0)\rangle\}$ . We note here that in the case where  $\{\langle \hat{B}^{\text{latt}}_{\lambda}(t=0)\rangle\}$  are zero by symmetry in equilibrium and the clusters inherit the relevant symmetries, the second condition is trivially satisfied.

We coevolve the sets of lattice and cluster equations—lattice equations determine  $\Gamma_i(t)$  for cluster evolution and lattice evolution is set by  $\{\langle \hat{B}_{\lambda}(t=0) \rangle\}$  obtained from

clusters. One iteration of the method evolves the system in time by a step dt. The algorithm can be described as follows (Fig. 3.3):

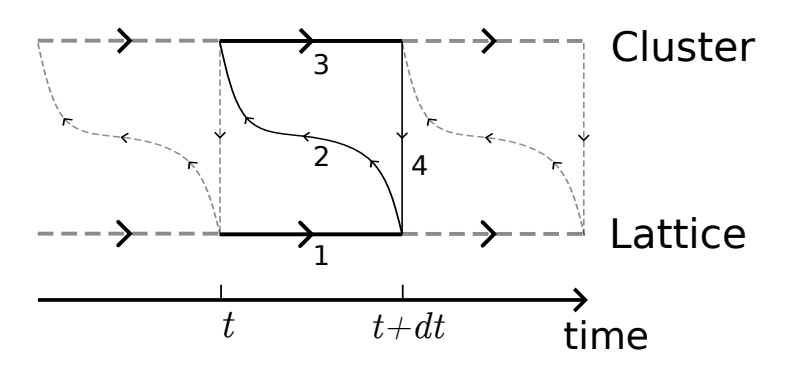


Figure 3.3: The OQCET algorithm in time

- 1.  $\{\langle \hat{A}^{\text{latt}}_{\lambda}(t) \rangle\}$  are evolved by a time step dt on the lattice by their respective EOM, using the values of  $\{\langle \hat{B}^{\text{latt}}_{\lambda}(t) \rangle\}$  obtained from the previous iteration. This gives us  $\{\langle \hat{A}^{\text{latt}}_{\lambda}(t+dt) \rangle\}$ . If this is the first iteration, then  $\{\langle \hat{B}^{\text{latt}}_{\lambda}(t=0) \rangle\}$  are the equilibrium expectation values.
- 2. On the cluster,  $\Gamma_i(t)$  are chosen such that the evolution  $t \to t + dt$  by the Lindblad equation Eq. (3.4) satisfies  $\{\langle \hat{A}_{\lambda}^{\text{clust}}(t+dt)\rangle\} = \{\langle \hat{A}_{\lambda}^{\text{latt}}(t+dt)\rangle\}$ . Since they constrain the cluster time evolution will refer to the set  $\{\langle \hat{A}_{\lambda}(t)\rangle\}$  as constrained operators.
- 3. The cluster density matrix is evolved to t + dt using  $\Gamma_i(t)$  and cluster EVs  $\{\langle \hat{B}_{\lambda}^{\text{clust}}(t+dt)\rangle\}$  are calculated
- 4. The cluster EVs  $\{\langle \hat{B}_{\lambda}^{\text{clust}}(t+dt)\rangle\}$  are mapped onto lattice EVs  $\{\langle \hat{B}_{\lambda}^{\text{latt}}(t+dt)\rangle\}$

This procedure is repeated until we reach a desired final time  $t_f$ . This is in contrast to the loop described in Section 2.2, where the hybridization  $\Delta$  is determined for all frequencies (all times) simultaneously. The comparison between OQCET and cluster DMFT is shown in Table 3.1.

	cluster DMFT	OQCET
Rep. model	Anderson impurity model	Open quantum cluster
Constr. Quantity	$G_{ij}$	$\langle \hat{A}_{\lambda} \rangle$
Rep. quantity	$\mid \Sigma_{ij} \mid$	$\left  \; \langle \hat{B}_{\lambda}  angle  ight $
Eff. field	$\mid \Delta \mid$	$\{\Gamma_i\}$
Latt. eq.	$G_{\text{latt}} = [G_{0,\text{latt}} - \Sigma_{\text{latt}}]^{-1}$	$\partial_t \langle A_{\lambda}(t) \rangle = f\left(\{\langle A_{\mu} \rangle\}, \{\langle \hat{B}_{\lambda} \rangle\}\right)$

Table 3.1: Cluster DMFT and OQCET as embedded cluster theories.

### 3.1 OQCET for the square lattice Hubbard model

We will describe the implementation of OQCET for the Hubbard model, following a non-equilibrium protocol to calculate the density response function  $\chi_{\mathbf{q}}(\omega)$ . The perturbing potential we introduce will be piecewise constant in time, i.e.  $\partial_t(\phi_{\mathbf{r}}(t)) =$ 0. We start with the square lattice Hamiltonian of the Hubbard model in a timedependent non-uniform scalar potential  $\phi_i(t)$ 

$$H(t) = -J \sum_{\mathbf{r}, \mathbf{u} \in \{\mathbf{e}_x, -\mathbf{e}_x, \mathbf{e}_y, -\mathbf{e}_y\}, \sigma} c_{\sigma, \mathbf{r}}^{\dagger} c_{\sigma, \mathbf{r} + \mathbf{u}} - \sum_{\mathbf{r}, \sigma} (\mu - \phi_{\mathbf{r}}(t)) n_{\sigma, \mathbf{r}} + U \sum_{\mathbf{r}} n_{\uparrow, \mathbf{r}} n_{\downarrow, \mathbf{r}}$$
(3.5)

We will restrict our calculations to disordered phases, so we assume that in equilibrium (in the absence of external fields  $\phi$ ) the system has both translation invariance and SU(2) spin symmetry. Since we are interested in the density response, we will have the density operator  $c_{\sigma,i}^{\dagger}c_{\sigma,i}$  in the set of constrained operators. If we wish for the energy to be a conserved quantity in our model, we must also constrain the bilinear  $c_{\sigma,i}^{\dagger}c_{\sigma,j}$  and the double occupancy operator  $n_{i\uparrow}n_{i\downarrow}$ . In Appendix B we show that constraining the bilinear and the double occupancy gives us both conservation of energy and conservation of particle number. DMFT and other embedded cluster theories generally break momentum conservation, and, in principle, there is no reason to expect our theory to obey momentum conservation either.

In the following sections we will derive the lattice equations of motion for the bilinear and the density-density operator  $n_{\sigma,i}n_{\sigma',j}$ . We will also outline the different variants of OQCET, depending on the choices of constrained and jump operators, field probe protocol, cluster Hamiltonian and initial density matrix.

### 3.2 Inverse linear response theory

In our implementation of inverse linear response theory (discussed in Section 2.3) we apply two different non-equilibrium protocols: one with potential localized in real space (protocol A), the other localized in **q**-space (protocol B) (Fig. 3.4). From Eq. (2.44), the generalized charge susceptibility  $\chi_{\sigma,\mathbf{r},\mathbf{r}'}(t)$  is defined as

$$\chi_{\sigma,\mathbf{r},\mathbf{r}'}(t) = -i\theta(t)\langle [n_{\sigma,\mathbf{r}}(t), n_{\sigma,\mathbf{r}'}(0)]\rangle_0$$
(3.6)

Since we have translation invariance,  $\chi_{\sigma,\mathbf{r},\mathbf{r}'}(t) = \chi_{\sigma,\mathbf{r}-\mathbf{r}'}(t)$  and the above can be rewritten as

$$\chi_{\mathbf{r}-\mathbf{r}'}(t) = -i\theta(t)\langle [n_{\sigma,\mathbf{r}}(t), n_{\sigma,\mathbf{r}'}(0)]\rangle_0$$
(3.7)

Its Fourier transform in space is defined as

$$\chi_{\mathbf{q}}(t) = \sum_{\sigma, \mathbf{r}} e^{-i\mathbf{q}\cdot\mathbf{r}} \chi_{\sigma, \mathbf{r} - \mathbf{r}'}(t)$$
(3.8)

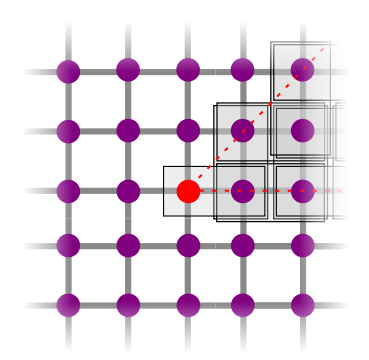
$$\chi_{\mathbf{q}}(t) = -i\theta(t)\langle [n_{\mathbf{q}}(t), n_{-\mathbf{q}}(0)]\rangle_0$$
(3.9)

where

$$n_{\mathbf{q}}(t) = \sum_{\sigma, \mathbf{k}} c_{\sigma, \mathbf{k}}^{\dagger}(t) c_{\sigma, \mathbf{k} + \mathbf{q}}(t)$$
(3.10)

### Protocol A

## Protocol B



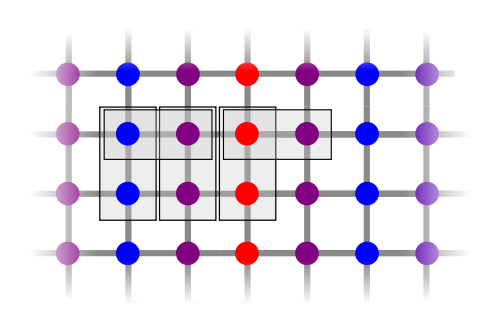


Figure 3.4: Schematic representation of non-equilibrium protocols. Boxes represent symmetry-irreducible 2x1 clusters. Colors correspond to values of the potential  $\phi_{\mathbf{r}}$ : +V (red), 0 (purple), -V (blue). The dashed lines in protocol A indicate the symmetry-irreducible part of the lattice. In protocol B, the wavelength represented is  $\lambda = 4$ .

In protocol A we introduce a delta potential at  $\mathbf{r} = \mathbf{0}$ 

$$\phi_{\mathbf{Ar}}(t) = \alpha \delta_{\mathbf{r},\mathbf{0}} \delta(t) \tag{3.11}$$

using Eq. (2.42) we get

$$\langle n_{\mathbf{r}}(t) \rangle - \langle n_{\mathbf{r}}(0) \rangle = \sum_{\mathbf{r}'} \int_{0}^{t} dt' \chi_{\mathbf{r}-\mathbf{r}'}(t-t') \phi_{A\mathbf{r}'}(t')$$

$$\langle \delta n_{\mathbf{r}}(t) \rangle = \sum_{\mathbf{r}'} \int_{0}^{t} dt' \chi_{\mathbf{r}-\mathbf{r}'}(t-t') \alpha \delta_{\mathbf{r},0} \delta(t')$$

$$\langle \delta n_{\mathbf{r}}(t) \rangle = \alpha \chi_{\mathbf{r}}(t)$$
(3.12)

 $\chi_{\mathbf{q}}(t)$  is then obtained as a Fourier transform of

$$\chi_{\mathbf{r}}(t) = \frac{1}{\alpha} \langle \delta n_{\mathbf{r}}(t) \rangle \tag{3.13}$$

For protocol B, we probe the system with a delta potential at wavevector  $\mathbf{q} = \mathbf{q}^*$ ,

$$\phi_{\mathbf{B}\mathbf{q}}(t) = \frac{\alpha}{2} \left( \delta_{\mathbf{q}^*,\mathbf{q}} + \delta_{-\mathbf{q}^*,\mathbf{q}} \right) \delta(t)$$
 (3.14)

We keep both  $\mathbf{q}^*$  and  $-\mathbf{q}^*$  terms to preserve inversion symmetry. In real space, this is equivalent to

$$\phi_{\mathrm{B}\mathbf{r}}(t) = \alpha \cos\left(\mathbf{q}^* \cdot \mathbf{r}\right) \delta(t) \tag{3.15}$$

Inverting the linear response equations

$$\langle n_{\mathbf{q}}(t) \rangle - \langle n_{\mathbf{q}}(0) \rangle = \sum_{\mathbf{q}} \int_{0}^{t} dt' \chi_{\mathbf{q}}(t - t') \phi_{\mathbf{B} - \mathbf{q}}(t')$$

$$\langle \delta n_{\mathbf{q}}(t) \rangle = \sum_{\mathbf{q}} \int_{0}^{t} dt' \chi_{\mathbf{q}}(t - t') \frac{\alpha}{2} \left( \delta_{\mathbf{q}^{*}, \mathbf{q}} + \delta_{-\mathbf{q}^{*}, \mathbf{q}} \right) \delta(t')$$

$$\langle \delta n_{\mathbf{q}}(t) \rangle = \frac{\alpha}{2} (\chi_{\mathbf{q}^{*}}(t) + \chi_{-\mathbf{q}^{*}}(t))$$

$$\langle \delta n_{\mathbf{q}}(t) \rangle = \alpha \chi_{\mathbf{q}^{*}}(t)$$
(3.16)

where we have used  $\chi_{\mathbf{q}}(t) = \chi_{-\mathbf{q}}(t)$ . This gives us  $\chi_{\mathbf{q}^*}(t)$  as a function of the density response  $\langle \delta n_{\mathbf{q}^*}(t) \rangle$ , which can be obtained as a Fourier transform of  $\langle \delta n_{\mathbf{r}}(t) \rangle$ .

In protocol A, we obtain the entire  $\chi_{\mathbf{q}}(t)$  in one calculation, but the potential  $\phi_{\mathrm{Ar'}}(t)$  breaks all translation symmetries. In protocol B one calculation only gives us  $\chi_{\mathbf{q}^*}(t)$  for one  $\mathbf{q}^*$ , but we preserve translation symmetry in the direction orthogonal to  $\mathbf{q}^*$ . The presence of additional symmetries means that we need fewer non-equivalent clusters, making the individual calculations significantly less computationally expensive. The number of clusters needed for protocol A scales as  $O(L^2)$ , where L is the linear length of the system, while for protocol B the scaling is O(L). In the special case where  $\mathbf{q}^*$  is collinear with a lattice unit vector and the wavelength  $\lambda = 2\pi/q$  is an integer, the system also retains translation symmetry along  $\mathbf{q}^*$  with a step of  $\lambda$  lattice spacings. Retaining inversion symmetry by the inclusion of  $-\mathbf{q}^*$  further reduces the number of irreducible clusters. This means that we then require  $O(\lambda)$  clusters, and we lose dependence on L, making calculations on large lattices easier.

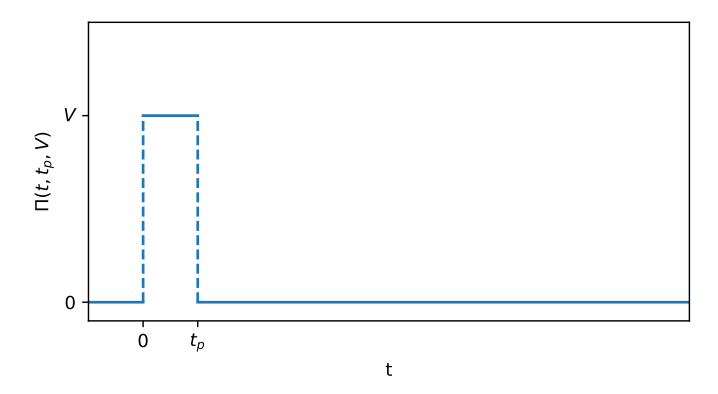


Figure 3.5: Boxcar function  $\Pi(t, t_p, V)$  with total area  $\alpha = Vt_p$ 

In our implementation, since we work with finite time steps, we approximate the potential delta with a boxcar function  $\Pi(t, t_p, V)$ 

$$\alpha \delta(t) \approx \Pi(t, t_p, V)$$

$$\Pi(t, t_p, V) = \begin{cases} V, & \text{if } 0 < t < t_p \\ 0, & \text{otherwise} \end{cases}$$
(3.17)

where  $t_p$  is the pulse duration and  $V = \alpha/t_p$ .

### 3.3 Lattice equations of motion

In this section we will be working in the Heisenberg picture, and we omit timedependence in notation for brevity,  $c_{\sigma,\mathbf{r}}^{\dagger} \equiv c_{\sigma,\mathbf{r}}^{\dagger}(t)$ . The Heisenberg equation for  $c_{\sigma,\mathbf{r}}^{\dagger}c_{\sigma,\mathbf{r}'}$ reads

$$\partial_t (c_{\sigma, \mathbf{r}}^{\dagger} c_{\sigma, \mathbf{r}'}) = i \left[ H, c_{\sigma, \mathbf{r}}^{\dagger} c_{\sigma, \mathbf{r}'} \right] \tag{3.18}$$

The Hamiltonian can be split into three terms,  $H = H_{\text{kin}} + H_{\text{pot}} + H_{\text{int}}$ . The kinetic energy term gives us

$$i\left[H_{\mathrm{kin}}, c_{\sigma,\mathbf{r}}^{\dagger} c_{\sigma,\mathbf{r}'}\right] = -iJ \sum_{\mathbf{r}'',\mathbf{u} \in \{\mathbf{e}_{x}, -\mathbf{e}_{x}, \mathbf{e}_{y}, -\mathbf{e}_{y}\}, \sigma'} \left[c_{\sigma',\mathbf{r}''}^{\dagger} c_{\sigma',\mathbf{r}''+\mathbf{u}}, c_{\sigma,\mathbf{r}}^{\dagger} c_{\sigma,\mathbf{r}'}\right]$$
(3.19)

applying the identity  $\left[a^{\dagger}b, c^{\dagger}d\right] = \delta_{bc}a^{\dagger}d - \delta_{ad}c^{\dagger}b$ 

$$i\left[H_{\mathrm{kin}}, c_{\sigma,\mathbf{r}}^{\dagger} c_{\sigma,\mathbf{r}'}\right] = -iJ \sum_{\mathbf{r}'',\mathbf{u},\sigma'} \delta_{\sigma,\sigma'} \left(\delta_{\mathbf{r}''+\mathbf{u},\mathbf{r}} c_{\sigma',\mathbf{r}''}^{\dagger} c_{\sigma,\mathbf{r}'} - \delta_{\mathbf{r}'',\mathbf{r}'} c_{\sigma,\mathbf{r}}^{\dagger} c_{\sigma',\mathbf{r}''+\mathbf{u}}\right)$$

$$= -iJ \sum_{\mathbf{u}} \left(c_{\sigma,\mathbf{r}-\mathbf{u}}^{\dagger} c_{\sigma,\mathbf{r}'} - c_{\sigma,\mathbf{r}}^{\dagger} c_{\sigma,\mathbf{r}'+\mathbf{u}}\right)$$
(3.20)

For the potential we have

$$i \left[ H_{\text{pot}}, c_{\sigma, \mathbf{r}}^{\dagger} c_{\sigma, \mathbf{r}'} \right] = -\sum_{\mathbf{r}'', \sigma'} (\mu - \phi_{\mathbf{r}''}) \left[ c_{\sigma', \mathbf{r}''}^{\dagger} c_{\sigma', \mathbf{r}''}, c_{\sigma, \mathbf{r}}^{\dagger} c_{\sigma, \mathbf{r}'} \right]$$

$$= -\sum_{\mathbf{r}'', \sigma'} (\mu - \phi_{\mathbf{r}''}) \delta_{\sigma, \sigma'} \left( \delta_{\mathbf{r}'', \mathbf{r}} c_{\sigma', \mathbf{r}''}^{\dagger} c_{\sigma, \mathbf{r}'} - \delta_{\mathbf{r}'', \mathbf{r}'} c_{\sigma, \mathbf{r}'} c_{\sigma', \mathbf{r}''} \right)$$

$$= -\left( (\mu - \phi_{\mathbf{r}}) - (\mu - \phi_{\mathbf{r}'}) \right) c_{\sigma, \mathbf{r}}^{\dagger} c_{\sigma, \mathbf{r}'}$$

$$= (\phi_{\mathbf{r}} - \phi_{\mathbf{r}'}) c_{\sigma, \mathbf{r}}^{\dagger} c_{\sigma, \mathbf{r}'}$$

$$(3.21)$$

Finally, for the interacting part

$$i\left[H_{\text{int}}, c_{\sigma,\mathbf{r}}^{\dagger} c_{\sigma,\mathbf{r}'}\right] = U \sum_{\mathbf{r}''} \left[c_{\sigma,\mathbf{r}''}^{\dagger} c_{\sigma,\mathbf{r}''} c_{\bar{\sigma},\mathbf{r}''}^{\dagger} c_{\bar{\sigma},\mathbf{r}''}, c_{\sigma,\mathbf{r}}^{\dagger} c_{\sigma,\mathbf{r}'}\right]$$

$$= U \sum_{\mathbf{r}''} c_{\bar{\sigma},\mathbf{r}''}^{\dagger} c_{\bar{\sigma},\mathbf{r}''} \left(\delta_{\mathbf{r}'',\mathbf{r}} c_{\sigma',\mathbf{r}'}^{\dagger} c_{\sigma,\mathbf{r}'} - \delta_{\mathbf{r}'',\mathbf{r}'} c_{\sigma,\mathbf{r}}^{\dagger} c_{\sigma',\mathbf{r}''}\right)$$

$$= U \left(c_{\bar{\sigma},\mathbf{r}}^{\dagger} c_{\bar{\sigma},\mathbf{r}} - c_{\bar{\sigma},\mathbf{r}'}^{\dagger} c_{\bar{\sigma},\mathbf{r}'}\right) c_{\sigma,\mathbf{r}}^{\dagger} c_{\sigma,\mathbf{r}'}$$

$$(3.22)$$

Combining everything together we have

$$\partial_{t}(c_{\sigma,\mathbf{r}}^{\dagger}c_{\sigma,\mathbf{r}'}) = i\left(-J\sum_{\mathbf{u}}\left(c_{\sigma,\mathbf{r}-\mathbf{u}}^{\dagger}c_{\sigma\mathbf{r}'} - c_{\sigma,\mathbf{r}}^{\dagger}c_{\sigma\mathbf{r}'+\mathbf{u}}\right) + (\phi_{\mathbf{r}} - \phi_{\mathbf{r}'})c_{\sigma,\mathbf{r}}^{\dagger}c_{\sigma,\mathbf{r}'}\right) + U\left(c_{\bar{\sigma},\mathbf{r}}^{\dagger}c_{\bar{\sigma},\mathbf{r}} - c_{\bar{\sigma},\mathbf{r}'}^{\dagger}c_{\bar{\sigma},\mathbf{r}'}\right)c_{\sigma,\mathbf{r}}^{\dagger}c_{\sigma,\mathbf{r}'}\right)$$

$$(3.23)$$

We now take the thermal average of the bilinear,  $X_{\sigma,\mathbf{r},\mathbf{r}'} = \langle c_{\sigma,\mathbf{r}}^{\dagger} c_{\sigma,\mathbf{r}'} \rangle$ 

$$\partial_{t} X_{\sigma,\mathbf{r},\mathbf{r}'} = i \left( -J \sum_{\mathbf{u}} (X_{\sigma,\mathbf{r}-\mathbf{u},\mathbf{r}'} - X_{\sigma,\mathbf{r},\mathbf{r}'+\mathbf{u}}) + (\phi_{\mathbf{r}} - \phi_{\mathbf{r}'}) X_{\sigma,\mathbf{r},\mathbf{r}'} + U \langle (c_{\bar{\sigma},\mathbf{r}}^{\dagger} c_{\bar{\sigma},\mathbf{r}} - c_{\bar{\sigma},\mathbf{r}'}^{\dagger} c_{\bar{\sigma},\mathbf{r}'}) c_{\sigma,\mathbf{r}}^{\dagger} c_{\sigma,\mathbf{r}'} \rangle \right)$$

$$(3.24)$$

The 4-operator average can be decomposed into connected and disconnected components

$$\left\langle \left( c_{\bar{\sigma},\mathbf{r}}^{\dagger} c_{\bar{\sigma},\mathbf{r}} - c_{\bar{\sigma},\mathbf{r}'}^{\dagger} c_{\bar{\sigma},\mathbf{r}'} \right) c_{\sigma,\mathbf{r}}^{\dagger} c_{\sigma,\mathbf{r}'} \right\rangle = \left( \left\langle c_{\bar{\sigma},\mathbf{r}}^{\dagger} c_{\bar{\sigma},\mathbf{r}} \right\rangle - \left\langle c_{\bar{\sigma},\mathbf{r}'}^{\dagger} c_{\bar{\sigma},\mathbf{r}'} \right\rangle \right) \left\langle c_{\sigma,\mathbf{r}}^{\dagger} c_{\sigma,\mathbf{r}'} \right\rangle + Y_{\sigma,\mathbf{r},\mathbf{r}'} \quad (3.25)$$

where we have introduced

$$Y_{\sigma,\mathbf{r},\mathbf{r}'} = \left\langle c_{\bar{\sigma},\mathbf{r}}^{\dagger} c_{\bar{\sigma},\mathbf{r}} c_{\sigma,\mathbf{r}'}^{\dagger} c_{\sigma,\mathbf{r}'} \right\rangle^{\text{conn}} - \left\langle c_{\bar{\sigma},\mathbf{r}'}^{\dagger} c_{\bar{\sigma},\mathbf{r}'} c_{\sigma,\mathbf{r}'}^{\dagger} c_{\sigma,\mathbf{r}'} \right\rangle^{\text{conn}}$$
(3.26)

By using  $X_{\sigma,\mathbf{r},\mathbf{r}'} = X_{\bar{\sigma},\mathbf{r},\mathbf{r}'}$  and substituting  $\mathbf{u} \to -\mathbf{u}$  in the first term we get

$$\partial_{t}X_{\sigma,\mathbf{r}\mathbf{r}'} = i\left(-J\sum_{\mathbf{u}}(X_{\sigma,\mathbf{r}+\mathbf{u},\mathbf{r}'} - X_{\sigma,\mathbf{r},\mathbf{r}'+\mathbf{u}}) + (\phi_{\mathbf{r}} - \phi_{\mathbf{r}'})X_{\sigma,\mathbf{r},\mathbf{r}'} + U\left((X_{\sigma,\mathbf{r},\mathbf{r}} - X_{\sigma,\mathbf{r}',\mathbf{r}'})X_{\sigma,\mathbf{r},\mathbf{r}'} + Y_{\sigma,\mathbf{r},\mathbf{r}'}\right)\right)$$

$$(3.27)$$

For the density-density operator we have

$$\partial_t(n_{\sigma,\mathbf{r}}n_{\sigma',\mathbf{r}'}) = -i\left[H, n_{\sigma,\mathbf{r}}n_{\sigma',\mathbf{r}'}\right] \tag{3.28}$$

The operator  $n_{\sigma,\mathbf{r}}n_{\sigma',\mathbf{r}'}$  commutes with the density operator  $n_{\sigma',\mathbf{r}''}$ , so the commutator  $[H_{\text{pot}} + H_{\text{int}}, n_{\sigma,\mathbf{r}}n_{\sigma',\mathbf{r}'}]$  vanishes and  $[H, n_{\sigma,\mathbf{r}}n_{\sigma',\mathbf{r}'}] = [H_{\text{kin}}, n_{\sigma,\mathbf{r}}n_{\sigma',\mathbf{r}'}]$ 

$$\partial_{t}(n_{\sigma,\mathbf{r}}n_{\sigma',\mathbf{r}'}) = i \left[ H_{\text{kin}}, n_{\sigma,\mathbf{r}}n_{\sigma',\mathbf{r}'} \right]$$

$$= -iJ \sum_{\mathbf{r}'',\mathbf{u},\sigma''} \left[ c^{\dagger}_{\sigma'',\mathbf{r}''}c_{\sigma'',\mathbf{r}''+\mathbf{u}}, n_{\sigma,\mathbf{r}}n_{\sigma',\mathbf{r}'} \right]$$

$$= -iJ \sum_{\mathbf{r}'',\mathbf{u},\sigma''} n_{\sigma,\mathbf{r}} \left[ c^{\dagger}_{\sigma'',\mathbf{r}''}c_{\sigma'',\mathbf{r}''+\mathbf{u}}, n_{\sigma',\mathbf{r}'} \right] + \left[ c^{\dagger}_{\sigma'',\mathbf{r}''}c_{\sigma'',\mathbf{r}''+\mathbf{u}}, n_{\sigma,\mathbf{r}} \right] n_{\sigma',\mathbf{r}'}$$

$$(3.29)$$

Following the same procedure as for the bilinear, we get

$$\partial_{t}(n_{\sigma,\mathbf{r}}n_{\sigma',\mathbf{r}'}) = -iJ \sum_{\mathbf{u}} \left\{ \left( c_{\sigma,\mathbf{r}-\mathbf{u}}^{\dagger} c_{\sigma,\mathbf{r}} - c_{\sigma,\mathbf{r}}^{\dagger} c_{\sigma,\mathbf{r}+\mathbf{u}} \right) n_{\sigma',\mathbf{r}'} + n_{\sigma,\mathbf{r}} \left( c_{\sigma',\mathbf{r}'-\mathbf{u}}^{\dagger} c_{\sigma',\mathbf{r}'} - c_{\sigma',\mathbf{r}'}^{\dagger} c_{\sigma',\mathbf{r}'+\mathbf{u}} \right) \right\}$$

$$(3.30)$$

By substituting  $\mathbf{u} \to -\mathbf{u}$  in the first terms in brackets we arrive

$$\partial_{t}(n_{\sigma,\mathbf{r}}n_{\sigma',\mathbf{r}'}) = -iJ \sum_{\mathbf{u}} \left\{ \left( c_{\sigma,\mathbf{r}+\mathbf{u}}^{\dagger} c_{\sigma,\mathbf{r}} - c_{\sigma,\mathbf{r}}^{\dagger} c_{\sigma,\mathbf{r}+\mathbf{u}} \right) n_{\sigma',\mathbf{r}'} + n_{\sigma,\mathbf{r}} \left( c_{\sigma',\mathbf{r}'+\mathbf{u}}^{\dagger} c_{\sigma',\mathbf{r}'} - c_{\sigma',\mathbf{r}'}^{\dagger} c_{\sigma',\mathbf{r}'+\mathbf{u}} \right) \right\}$$

$$(3.31)$$

We now take the thermal average, and decompose the averages into connected and disconnected components

$$\partial_{t} \langle n_{\sigma,\mathbf{r}} n_{\sigma',\mathbf{r}'} \rangle = -iJ \sum_{\mathbf{u}} \left\{ \left( \left\langle c_{\sigma,\mathbf{r}+\mathbf{u}}^{\dagger} c_{\sigma,\mathbf{r}} \right\rangle - \left\langle c_{\sigma,\mathbf{r}}^{\dagger} c_{\sigma,\mathbf{r}+\mathbf{u}} \right\rangle \right) \left\langle n_{\sigma',\mathbf{r}'} \right\rangle + \left\langle n_{\sigma,\mathbf{r}} \right\rangle \left( \left\langle c_{\sigma',\mathbf{r}'+\mathbf{u}}^{\dagger} c_{\sigma',\mathbf{r}'} \right\rangle - \left\langle c_{\sigma',\mathbf{r}'}^{\dagger} c_{\sigma',\mathbf{r}'+\mathbf{u}} \right\rangle \right) + \left\langle n_{\sigma,\sigma'} \left\langle c_{\sigma,\mathbf{r}}^{\dagger} c_{\sigma',\mathbf{r}'} \right\rangle \left( \left\langle c_{\sigma',\mathbf{r}'}^{\dagger} c_{\sigma,\mathbf{r}+\mathbf{u}} \right\rangle - \left\langle c_{\sigma',\mathbf{r}'+\mathbf{u}}^{\dagger} c_{\sigma,\mathbf{r}} \right\rangle \right) + \left\langle n_{\sigma,\sigma'} \left\langle c_{\sigma',\mathbf{r}'}^{\dagger} c_{\sigma',\mathbf{r}'} \right\rangle \left( \left\langle c_{\sigma,\mathbf{r}}^{\dagger} c_{\sigma',\mathbf{r}'+\mathbf{u}} \right\rangle - \left\langle c_{\sigma',\mathbf{r}+\mathbf{u}}^{\dagger} c_{\sigma',\mathbf{r}'} \right\rangle \right) + \left\langle n_{\sigma,\sigma'} \left\langle c_{\sigma',\mathbf{r}'}^{\dagger} c_{\sigma,\mathbf{r}} \right\rangle \left( \left\langle c_{\sigma,\mathbf{r}+\mathbf{u}}^{\dagger} c_{\sigma',\mathbf{r}'+\mathbf{u}} \right\rangle - \left\langle c_{\sigma,\mathbf{r}+\mathbf{u}}^{\dagger} c_{\sigma',\mathbf{r}'} \right\rangle \right) + \left\langle n_{\sigma,\sigma'} \left\langle c_{\sigma,\mathbf{r}+\mathbf{u}}^{\dagger} c_{\sigma',\mathbf{r}'} \right\rangle - \left\langle c_{\sigma,\mathbf{r}}^{\dagger} c_{\sigma',\mathbf{r}'+\mathbf{u}} \right\rangle + \left\langle n_{\sigma,\sigma'} \left\langle c_{\sigma,\mathbf{r}+\mathbf{u}}^{\dagger} c_{\sigma',\mathbf{r}'} \right\rangle - \left\langle c_{\sigma,\mathbf{r}}^{\dagger} c_{\sigma',\mathbf{r}'+\mathbf{u}} \right\rangle - \left\langle c_{\sigma,\mathbf{r}+\mathbf{u}}^{\dagger} c_{\sigma',\mathbf{r}'+\mathbf{u}} \right\rangle + \left\langle n_{\sigma,\sigma'} \left\langle c_{\sigma,\mathbf{r}+\mathbf{u}}^{\dagger} c_{\sigma',\mathbf{r}'} \right\rangle - \left\langle c_{\sigma,\mathbf{r}+\mathbf{u}}^{\dagger} c_{\sigma',\mathbf{r}'+\mathbf{u}} \right\rangle - \left\langle c_{\sigma,\mathbf{r}+\mathbf{u}}^{\dagger} c_{\sigma',\mathbf{r}'+\mathbf{u}} \right\rangle - \left\langle c_{\sigma,\mathbf{r}+\mathbf{u}}^{\dagger} c_{\sigma',\mathbf{r}'+\mathbf{u}} \right\rangle + \left\langle n_{\sigma,\sigma'} \left\langle c_{\sigma,\mathbf{r}+\mathbf{u}}^{\dagger} c_{\sigma',\mathbf{r}'} \right\rangle - \left\langle c_{\sigma,\mathbf{r}+\mathbf{u}}^{\dagger} c_{\sigma',\mathbf{r}'+\mathbf{u}} \right\rangle - \left\langle c_{\sigma,\mathbf{r}+\mathbf{u}}^{\dagger} c_{\sigma',\mathbf{r}'} \right\rangle + \left\langle n_{\sigma,\sigma'} \left\langle c_{\sigma,\mathbf{r}+\mathbf{u}}^{\dagger} c_{\sigma',\mathbf{r}'} \right\rangle - \left\langle c_{\sigma,\mathbf{r}+\mathbf{u}}^{\dagger} c_{\sigma',\mathbf{r}'} \right\rangle + \left\langle n_{\sigma,\sigma'} \left\langle c_{\sigma,\mathbf{r}+\mathbf{u}}^{\dagger} c_{\sigma',\mathbf{r}'} \right\rangle + \left\langle n_{\sigma,\sigma'} \left\langle c_{\sigma,\mathbf{r}+\mathbf{u}}^{\dagger} c_{\sigma',\mathbf{r}'} \right\rangle + \left\langle n_{\sigma,\sigma'} \left\langle c_{\sigma,\mathbf{r}+\mathbf{u}}^{\dagger} c_{\sigma',\mathbf{r}'} \right\rangle - \left\langle n_{\sigma,\sigma'} \left\langle c_{\sigma,\mathbf{r}+\mathbf{u}}^{\dagger} c_{\sigma',\mathbf{r}'} \right\rangle + \left\langle n_{\sigma,\sigma'} \left\langle c_{\sigma,\mathbf{$$

Where

$$W_{\sigma,\sigma',\mathbf{r},\mathbf{r}'} = \left\langle \sum_{\mathbf{u}} \left\{ \left( c_{\sigma,\mathbf{r}+\mathbf{u}}^{\dagger} c_{\sigma,\mathbf{r}} - c_{\sigma,\mathbf{r}}^{\dagger} c_{\sigma,\mathbf{r}+\mathbf{u}} \right) n_{\sigma',\mathbf{r}'} + n_{\sigma,\mathbf{r}} \left( c_{\sigma',\mathbf{r}'+\mathbf{u}}^{\dagger} c_{\sigma',\mathbf{r}'} - c_{\sigma',\mathbf{r}'}^{\dagger} c_{\sigma',\mathbf{r}'+\mathbf{u}} \right) \right\} \right\rangle^{\text{conn}}$$

$$+ n_{\sigma,\mathbf{r}} \left( c_{\sigma',\mathbf{r}'+\mathbf{u}}^{\dagger} c_{\sigma',\mathbf{r}'} - c_{\sigma',\mathbf{r}'}^{\dagger} c_{\sigma',\mathbf{r}'+\mathbf{u}} \right) \right\} \right\rangle^{\text{conn}}$$

$$(3.33)$$

We have spin symmetry in our system, so we can rewrite Eq. (3.32) using  $X_{\sigma,\mathbf{r},\mathbf{r}'} = X_{\sigma',\mathbf{r},\mathbf{r}'}$ 

$$\partial_{t} \langle n_{\sigma,\mathbf{r}} n_{\sigma',\mathbf{r}'} \rangle = -iJ \sum_{\mathbf{u}} \left\{ (X_{\sigma,\mathbf{r}+\mathbf{u},\mathbf{r}'} - X_{\sigma,\mathbf{r},\mathbf{r}+\mathbf{u}}) X_{\sigma,\mathbf{r}',\mathbf{r}'} + X_{\sigma,\mathbf{r},\mathbf{r}'} (X_{\sigma,\mathbf{r}'+\mathbf{u},\mathbf{r}'} - X_{\sigma,\mathbf{r}',\mathbf{r}'+\mathbf{u}}) + \delta_{\sigma,\sigma'} X_{\sigma,\mathbf{r},\mathbf{r}'} (X_{\sigma,\mathbf{r}',\mathbf{r}+\mathbf{u}} - X_{\sigma,\mathbf{r}'+\mathbf{u},\mathbf{r}}) + \delta_{\sigma,\sigma'} X_{\sigma,\mathbf{r}',\mathbf{r}} (X_{\sigma,\mathbf{r},\mathbf{r}'+\mathbf{u}} - X_{\sigma,\mathbf{r}+\mathbf{u},\mathbf{r}'}) + \delta_{\sigma,\sigma'} \delta_{\mathbf{r},\mathbf{r}'} (X_{\sigma,\mathbf{r}+\mathbf{u},\mathbf{r}'} - X_{\sigma,\mathbf{r},\mathbf{r}'+\mathbf{u}}) + \delta_{\sigma,\sigma'} (\delta_{\mathbf{r},\mathbf{r}'+\mathbf{u}} - \delta_{\mathbf{r}+\mathbf{u},\mathbf{r}'}) X_{\sigma,\mathbf{r},\mathbf{r}'} \right\} - iJW_{\sigma,\sigma',\mathbf{r},\mathbf{r}'}$$

$$(3.34)$$

The double occupancy thermal average,  $d_{\mathbf{r}} = \langle n_{\uparrow,\mathbf{r}} n_{\downarrow,\mathbf{r}} \rangle$  is a special case of the above expression,

$$\partial_t d_{\mathbf{r}} = -2iJ \sum_{\mathbf{u}} \left( X_{\sigma, \mathbf{r} + \mathbf{u}, \mathbf{r}} - X_{\sigma, \mathbf{r}, \mathbf{r} + \mathbf{u}} \right) X_{\sigma, \mathbf{r}, \mathbf{r}} - iJW_{\uparrow, \downarrow, \mathbf{r}, \mathbf{r}}$$
(3.35)

By taking the complex conjugate of Eq. (3.26), we get

$$Y_{\sigma,\mathbf{r},\mathbf{r}'}^{*} = \left\langle c_{\bar{\sigma},\mathbf{r}}^{\dagger} c_{\bar{\sigma},\mathbf{r}} c_{\sigma,\mathbf{r}'}^{\dagger} c_{\sigma,\mathbf{r}} \right\rangle^{\text{conn}} - \left\langle c_{\bar{\sigma},\mathbf{r}'}^{\dagger} c_{\bar{\sigma},\mathbf{r}'} c_{\sigma,\mathbf{r}'}^{\dagger} c_{\sigma,\mathbf{r}} \right\rangle^{\text{conn}}$$

$$= -Y_{\bar{\sigma},\mathbf{r}',\mathbf{r}}$$
(3.36)

Analogously for Eq. (3.33)

$$W_{\sigma,\sigma',\mathbf{r},\mathbf{r}'}^* = -\left\langle \sum_{\mathbf{u}} \left\{ n_{\sigma',\mathbf{r}'} \left( c_{\sigma,\mathbf{r}+\mathbf{u}}^{\dagger} c_{\sigma,\mathbf{r}} - c_{\sigma,\mathbf{r}}^{\dagger} c_{\sigma,\mathbf{r}+\mathbf{u}} \right) + \left( c_{\sigma',\mathbf{r}'+\mathbf{u}}^{\dagger} c_{\sigma',\mathbf{r}'} - c_{\sigma',\mathbf{r}'}^{\dagger} c_{\sigma',\mathbf{r}'+\mathbf{u}} \right) n_{\sigma,\mathbf{r}} \right\} \right\rangle^{\text{conn}}$$

$$= -W_{\sigma',\sigma,\mathbf{r}',\mathbf{r}}$$

$$= -W_{\sigma',\sigma,\mathbf{r}',\mathbf{r}}$$
(3.37)

Since at equilibrium  $Y_{\sigma,\mathbf{r},\mathbf{r}'} = Y_{\bar{\sigma},\mathbf{r}'\mathbf{r}}$  and  $W_{\sigma,\sigma',\mathbf{r},\mathbf{r}'} = W_{\sigma',\sigma,\mathbf{r}',\mathbf{r}}$  by symmetry, we conclude  $Y_{\sigma,\mathbf{r},\mathbf{r}'}(t=0) = 0$  and  $W_{\sigma,\sigma',\mathbf{r},\mathbf{r}'}(t=0) = 0$ .

# 3.4 Preparing the initial state

To prepare the initial state for OQCET, we must obtain lattice expectation values of our constrained operators  $\{\langle \hat{A}^{\text{latt}}_{\lambda}(t=0)\rangle\}$  and initialize a cluster density matrix with matching equilibrium EVs.

### 3.4.1 Equilibrium lattice thermal averages

The quantities we are interested in, the fermionic bilinear and the double occupancy can both be obtained directly from the full Green's function and self-energies in the imaginary-time formalism. As defined in Eq. (2.5), the Matsubara Green's function is

$$G_{\sigma,ij}(\tau) = -\left\langle \mathcal{T}c_{\sigma,i}(\tau)c_{\sigma,j}^{\dagger}(0)\right\rangle \tag{3.38}$$

The bilinear is simply the appropriate component of the Green's function at time  $\tau = 0^-$ :

$$G_{\sigma,ij}(\tau=0^{-}) = -\left\langle \mathcal{T}c_{\sigma,i}(0^{-})c_{\sigma,j}^{\dagger}(0)\right\rangle = \left\langle c_{\sigma,j}^{\dagger}(0)c_{\sigma,i}(0^{-})\right\rangle \tag{3.39}$$

The double occupancy  $d_{\mathbf{r}} \equiv d$  can be calculated from the well-known Migdal-Galitskii formula [49]

$$d = \frac{1}{U} \sum_{\mathbf{k}, i\omega_n} G_{\mathbf{k}}(i\omega_n) \Sigma_{\mathbf{k}}(i\omega_n) = \lim_{\eta \to 0^-} \frac{1}{U} \sum_{\mathbf{k}, i\omega_n} G_{\mathbf{k}}(i\omega_n) \Sigma_{\mathbf{k}}(i\omega_n) e^{i\omega_n \eta}$$
(3.40)

To obtain numerically exact values for the self-energy, we employ the quantum Monte Carlo method CTINT implemented in the TRIQS library. [34, 50]. Since CTINT is a Monte Carlo method, we first symmetrize the result to reduce statistical noise and enforce lattice symmetries. To study long wavelength response, we need to work

with lattices of size  $\sim$ 64x64. We cannot obtain the self-energy for such large lattices directly, as CTINT is limited to  $\sim$ 8x8 lattices. However, at high temperatures the self-energy is sufficiently short-ranged and the 8x8 lattice self-energy is a good approximation. The CTINT self-energy can be mapped onto the larger lattice (Fig. 3.6) by the formula

$$\Sigma_{\mathbf{r}}^{\text{latt}} = \begin{cases} \Sigma_{\mathbf{r}}^{\text{CTINT}} & \text{if } |x| \leq \frac{1}{2}L^{\text{CTINT}} \text{ and } |y| \leq \frac{1}{2}L^{\text{CTINT}} \\ 0, & \text{otherwise} \end{cases}$$
(3.41)

for a CTINT lattice of size  $L^{\text{CTINT}}$  x  $L^{\text{CTINT}}$ .

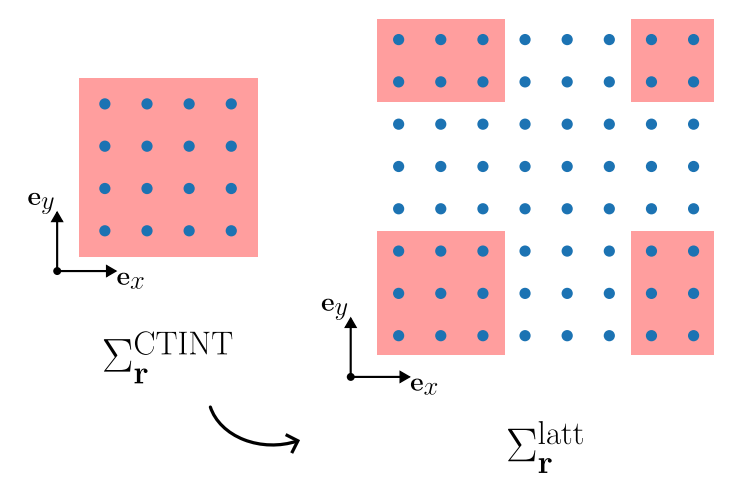


Figure 3.6: Mapping of CTINT self-energy (red) onto a larger lattice. The self energy for remaining sites is set to zero.

The full lattice Green's function is then calculated as

$$G_{\mathbf{k}}(i\omega_n) = \frac{1}{i\omega_n - \varepsilon_{\mathbf{k}} + \mu - \Sigma_{\mathbf{k}}(i\omega_n)}$$
(3.42)

This procedure is analogous to the periodization step in CDMFT discussed in Section 2.2.2. To obtain the expectation values for the bilinear and the double occupancy, we must perform Fourier transforms of the quantities  $G_{\sigma,ij}(i\omega)$  and  $\sum_{\mathbf{k}} G_{\mathbf{k}}(i\omega_n) \Sigma_{\mathbf{k}}(i\omega_n)$ , as described in Appendix C.

Two-particle quantities such as the nearest neighbor density-density correlator  $n_{\sigma,\mathbf{r}}n_{\sigma',\mathbf{r}+\mathbf{u}}$  cannot be obtained just from the self energy, but can be measured directly in CTINT. In this case, we use the CTINT data directly, assuming that it does not significantly depend on lattice size.

### 3.4.2 Clusters in equilibrium

The initial cluster expectation values can be calculated as

$$\langle \hat{A}_{\lambda}^{\text{clust}}(t=0) \rangle = \text{Tr} \left[ \rho_{\text{clust}}(t=0) \hat{A}^{\text{clust}} \right]$$
 (3.43)

A natural way to prepare the cluster density matrix would be to create a reduced density matrix by tracing all lattice degrees of freedom outside the cluster (from the environment)

$$\rho_{\text{clust}}(t=0) = \text{Tr}_{\text{Env}}[\rho_{\text{latt}}(t=0)] \tag{3.44}$$

where  $\text{Tr}_{\text{Env}}$  represents a partial trace of the environment degrees of freedom. This guarantees that cluster expectation values will match lattice EVs for all possible single- and many-body operators in the initial state. The reduced density matrix is however computationally very difficult to obtain for large lattices. Another problem is that the reduced density matrix will generally not commute with the projected cluster Hamiltonian, meaning that the EOM for  $\rho_{\text{clust}}$  will not be stationary even in absence of external fields. One possible way to address this is to introduce additional jump operators  $\{\tilde{L}_i\}$  and coupling  $\{\tilde{\Gamma}_i\}$  in Eq. (3.4) such that  $\rho_{\text{clust}}$  presents a stationary solution for the corresponding Lindblad equation. In this case, applying the stationarity condition  $\partial \rho_0/\partial t = 0$  to Eq. (3.4) we get

$$i[H, \rho_0] = \sum_{i} \tilde{\Gamma}_i \left( \tilde{L}_i \rho_0 \tilde{L}_i^{\dagger} - \frac{1}{2} \left\{ \tilde{L}_i^{\dagger} \tilde{L}_i, \rho_0 \right\} \right)$$
 (3.45)

since  $\Gamma_i(t=0) \equiv 0$ .

It is not immediately clear how to choose  $\tilde{L}_i$  and  $\tilde{\Gamma}_i$  to satisfy this condition. If we now write the equations of motion for  $\rho$  very close to  $\rho_0$ ,  $\rho(t) = \rho_0 + \Delta \rho(t)$ 

$$\frac{d\rho(t)}{dt} = -i[H_{\text{clust}}, \rho(t)] + \sum_{i} \tilde{\Gamma}_{i} \left( \tilde{L}_{i}(\rho_{0} + \Delta \rho(t)) \tilde{L}_{i}^{\dagger} - \frac{1}{2} \left\{ \tilde{L}_{i}^{\dagger} \tilde{L}_{i}, (\rho_{0} + \Delta \rho(t)) \right\} \right) + \sum_{i} \Gamma_{i}(t) \left( L_{i}\rho(t) L_{i}^{\dagger} - \frac{1}{2} \left\{ L_{i}^{\dagger} L_{i}, \rho(t) \right\} \right)$$
(3.46)

if we ignore contributions from the  $\Delta \rho$  term in the second term on the RHS, substituting Eq. (3.45) we get

$$\frac{d\rho(t)}{dt} = -i[H_{\text{clust}}, \rho(t)] + i[H, \rho_0] + \sum_{i} \Gamma_i(t) \left( L_i \rho(t) L_i^{\dagger} - \frac{1}{2} \left\{ L_i^{\dagger} L_i, \rho(t) \right\} \right) 
= -i[H_{\text{clust}}, \rho(t) - \rho_0] + \sum_{i} \Gamma_i(t) \left( L_i \rho(t) L_i^{\dagger} - \frac{1}{2} \left\{ L_i^{\dagger} L_i, \rho(t) \right\} \right)$$
(3.47)

With this modified Heisenberg equation, we now have satisfied the stationarity condition, while the reduced density matrix gives us appropriate expectation values.

As the computation of a reduced density matrix on large lattices is difficult, we propose two alternative schemes. In the first, we modify Hamiltonian parameters  $\mu,t,U$  on the cluster and use the thermal density matrix corresponding to that Hamiltonian (at the same temperature as the lattice). The parameters are tuned so that the cluster EVs of constrained operators match lattice EVs. For constraining  $X_{i,j}$  and  $d_i$  the choice of  $\mu,t,U$  as parameters make clear physical sense, as they modify

the density, kinetic, and potential energy. For more complicate choices of constrained operators, additional terms would have to be introduced into the Hamiltonian with corresponding parameters.

In the second scheme we start with an unmodified, projected lattice Hamiltonian. The density matrix is then constructed as a modified Boltzmann ensemble

$$\rho_{\text{clust}}(t=0) = \frac{1}{Z'} \sum_{\lambda} \sum_{k \in \lambda} \sum_{\alpha} \sum_{i,j \in \alpha} e^{-\beta E_{\alpha} \delta_{i,j} - \gamma_{\lambda,k} \langle \Psi_{\alpha_i} | A_{\lambda,k} | \Psi_{\alpha_j} \rangle} |\Psi_{\alpha_j} \rangle \langle \Psi_{\alpha_i} |$$

$$Z' = \text{Tr} \left[ \sum_{\lambda} \sum_{k \in \lambda} \sum_{\alpha} \sum_{i,j \in \alpha} e^{-\beta E_{\alpha} \delta_{i,j} - \gamma_{\lambda,k} \langle \Psi_{\alpha_i} | A_{\lambda,k} | \Psi_{\alpha_j} \rangle} \right]$$
(3.48)

where  $\alpha$  are eigenspaces of the Hamiltonian,  $E_{\alpha}$  are the associated eigenvalues and  $\Psi_{\alpha_i}$  are vectors in the eigenspace  $\alpha$ . The index k represents a sum over all components of the constrained operator tensors  $\{\hat{A}_{\lambda}^{\text{latt}}\}$ , so  $A_{\lambda,k}$  is a scalar in the space of cluster indices (it is of course still a matrix in the cluster Hilbert space). The parameters  $\gamma_{\lambda,k}$  are again chosen to reproduce lattice EVs for constrained operators.

Projecting onto the eigenspaces guarantees that  $[\rho, H] = 0$ . In the Hamiltonian eigenbasis, the density matrix has a block diagonal form  $\rho = \bigoplus_{\alpha} \rho_{\alpha}$ , with the blocks corresponding to eigenspaces  $\alpha$ . In each block  $\alpha$  the Hamiltonian has a scalar form,  $H_{\alpha} = E_{\alpha}I_{\alpha}$ , where  $I_{\alpha}$  is the identity matrix with dimension  $\dim(\alpha)$ . Since scalar matrix commutes with every matrix,

$$[H_{\alpha}, \rho_{\alpha}] = 0 \tag{3.49}$$

The commutator of block matrices is simply a block matrix of commutators of individual blocks, so

$$[H, \rho] = \bigoplus_{\alpha} [H_{\alpha}, \rho_{\alpha}] = 0 \tag{3.50}$$

The obvious approach might have been to try to modify the weights  $w(\Psi)$  in the ensemble

$$\rho_{\text{clust}} = \sum_{\psi} w(\Psi) |\Psi\rangle \langle \Psi| \qquad (3.51)$$

where  $|\Psi\rangle$  are system eigenstates. However, if these eigenstates were obtained numerically, we cannot make sure to get  $|\Psi\rangle$  that obey system symmetries. This means that tuning  $w(\Psi)$  can break these symmetries, making it an unsuitable approach. The approach we described previously respects symmetries by construction and is independent of the choice of basis for degenerate eigenstates.

#### 3.5 Cluster dynamics

As previously introduced, cluster dynamics are governed by the Lindblad equation

$$\frac{d\rho(t)}{dt} = -i[H_{\text{clust}}, \rho(t)] + \sum_{i} \Gamma_{i}(t) \left( L_{i}\rho(t)L_{i}^{\dagger} - \frac{1}{2} \left\{ L_{i}^{\dagger}L_{i}, \rho(t) \right\} \right)$$
(3.52)

If we are using the reduced density matrix method, the first term on the right-hand side becomes  $[H_{\text{clust}}, \rho(t) - \rho_0]$ , but the rest of the derivation proceeds completely analogously. For brevity, we will use H for  $H_{\text{clust}}$  in the remainder of the section. A short derivation of Eq. (3.52) is outlined in Appendix A.

For some choices of jump operators nonzero contributions to operator expectation values start at the second order, so we solve the equations to second order in  $\Delta t$ 

$$\rho(t_{i+1}) = \rho(t_i) + \Delta t \cdot \frac{d\rho}{dt} \Big|_{t=t_i} + \frac{1}{2} (\Delta t)^2 \cdot \frac{d^2 \rho}{dt^2} \Big|_{t=t_i}.$$
 (3.53)

The second derivative can be expanded as follows:

$$\frac{d^2\rho}{dt^2} = -i\left[H, \frac{d\rho(t)}{dt}\right] + \sum_{i} \Gamma_i(t) \left(L_i \frac{d\rho(t)}{dt} L_i^{\dagger} - \frac{1}{2} \left\{\frac{d\rho(t)}{dt}, L_i^{\dagger} L_i\right\}\right) + \sum_{i} \frac{d\Gamma_i(t)}{dt} \left(L_i \rho(t) L_i^{\dagger} - \frac{1}{2} \left\{\rho(t), L_i^{\dagger} L_i\right\}\right)$$
(3.54)

Substituting Eq. (3.52) and Eq. (3.54) into Eq. (3.53) we get

$$\rho(t_{i+1}) = \rho(t_i)$$

$$+ \Delta t \cdot \left( -i \left[ H, \rho(t_i) \right] + \sum_{i} \left( \Gamma_i(t_i) + \frac{1}{2} \Delta t \frac{d\Gamma}{dt} \Big|_{t=t_i} \right) \left( L_i \rho(t_i) L_i^{\dagger} - \frac{1}{2} \left\{ \rho(t_i), L_i^{\dagger} L_i \right\} \right) \right)$$

$$+ \frac{1}{2} (\Delta t)^2 \left( -i \left[ H, \frac{d\rho}{dt} \Big|_{t=t_i} \right] + \sum_{i} \Gamma_i(t_i) \left( L_i \frac{d\rho}{dt} \Big|_{t=t_i} L_i^{\dagger} - \frac{1}{2} \left\{ \frac{d\rho}{dt} \Big|_{t=t_i}, L_i^{\dagger} L_i \right\} \right) \right)$$

$$(3.55)$$

We can now make the substitution  $\Gamma'_i(t) = \Gamma_i(t) + \frac{1}{2}\Delta t \frac{d\Gamma(t)}{dt}$ . This is equivalent to taking the value of  $\Gamma_i(t)$  at the midpoint of the interval, assuming  $\Gamma_i(t)$  is piecewise linear. Ignoring terms of order  $(\Delta t)^3$  we arrive at

$$\rho(t_{i+1}) = \rho(t_i) + \Delta t \cdot \left( -i \left[ H, \rho(t_i) \right] + \sum_i \Gamma_i'(t_i) \left( L_i \rho(t_i) L_i^{\dagger} - \frac{1}{2} \left\{ \rho(t_i), L_i^{\dagger} L_i \right\} \right) \right)$$

$$+ \frac{1}{2} (\Delta t)^2 \left( -i \left[ H, \frac{d\rho}{dt} \Big|_{t=t_i} \right] + \sum_i \Gamma_i'(t_i) \left( L_i \frac{d\rho}{dt} \Big|_{t=t_i} L_i^{\dagger} - \frac{1}{2} \left\{ \frac{d\rho}{dt} \Big|_{t=t_i}, L_i^{\dagger} L_i \right\} \right) \right)$$

$$(3.56)$$

By introducing the new parameters  $\Gamma'_i$  we can solve the differential equation to second order without worrying about the parameters' derivatives. The derivative  $\frac{d\rho}{dt}$  in Eq. (3.56) is calculated as:

$$\left. \frac{d\rho}{dt} \right|_{t=t_i} \approx -i \left[ H, \rho(t_i) \right] + \sum_i \Gamma_i'(t_i) \left( L_i \rho(t_i) L_i^{\dagger} - \frac{1}{2} \left\{ \rho(t_i), L_i^{\dagger} L_i \right\} \right)$$
(3.57)

Where we have substituted  $\Gamma'_i$  into Eq. (3.52) and discarded the  $\sim \Delta t$  term, as its contribution to Eq. (3.56) would be of the order  $(\Delta t)^3$ . To simplify notation, we will

relabel  $\Gamma'_i$  as  $\Gamma_i$ .

Expanding each term in Eq. (3.56) we get:

$$-i\left[H,\frac{d\rho}{dt}\right] = -\left\{HH,\rho\right\} + 2H\rho H - i\sum_{i}\Gamma_{i}\left(\left[H,L_{i}\rho L_{i}^{\dagger}\right] - \frac{1}{2}\left[H,\left\{\rho,L_{i}^{\dagger}L_{i}\right\}\right]\right)$$

$$\sum_{i}\Gamma_{i}L_{i}\frac{d\rho}{dt}L_{i}^{\dagger} = -i\sum_{i}\Gamma_{i}L_{i}\left[H,\rho\right]L_{i}^{\dagger} + \sum_{i,j}\Gamma_{i}\Gamma_{j}\left(L_{i}L_{j}\rho L_{j}^{\dagger}L_{i}^{\dagger} - \frac{1}{2}L_{i}\left\{\rho,L_{j}^{\dagger}L_{j}\right\}L_{i}^{\dagger}\right)$$

$$-\frac{1}{2}\sum_{i}\Gamma_{i}\left\{\frac{d\rho}{dt},L_{i}^{\dagger}L_{i}\right\} = \frac{i}{2}\sum_{i}\Gamma_{i}\left\{\left[H,\rho\right],L_{i}^{\dagger}L_{i}\right\} - \frac{1}{2}\sum_{i,j}\Gamma_{i}\Gamma_{j}\left\{L_{j}\rho L_{j}^{\dagger},L_{i}^{\dagger}L_{i}\right\}$$

$$+\frac{1}{4}\sum_{i,j}\Gamma_{i}\Gamma_{j}\left\{\left\{\rho,L_{j}^{\dagger}L_{j}\right\},L_{i}^{\dagger}L_{i}\right\}$$

$$(3.60)$$

We can rewrite Eq. (3.56) in terms of sums over  $\{\Gamma_i\}$  by introducing the following:

$$P = \Delta t \cdot (-i[H, \rho]) + \frac{1}{2} (\Delta t)^2 (-\{HH, \rho\} + 2H\rho H)$$
 (3.61)

$$Q_{i} = \Delta t \left( L_{i} \rho L_{i}^{\dagger} - \frac{1}{2} \left\{ \rho, L_{i}^{\dagger} L_{i} \right\} \right) + \frac{1}{2} (\Delta t)^{2} \left( -i \left[ H, L_{i} \rho L_{i}^{\dagger} \right] + \frac{i}{2} \left[ H, \left\{ \rho, L_{i}^{\dagger} L_{i} \right\} \right] - i L_{i} \left[ H, \rho \right] L_{i}^{\dagger} + \frac{i}{2} \left\{ \left[ H, \rho \right], L_{i}^{\dagger} L_{i} \right\} \right)$$

$$(3.62)$$

$$R_{ij} = \frac{1}{2} (\Delta t)^2 \left( L_i L_j \rho L_j^{\dagger} L_i^{\dagger} - \frac{1}{2} \left( L_i \left\{ \rho, L_j^{\dagger} L_j \right\} L_i^{\dagger} + \left\{ L_j \rho L_j^{\dagger}, L_i^{\dagger} L_i \right\} - \frac{1}{2} \left\{ \left\{ \rho, L_j^{\dagger} L_j \right\}, L_i^{\dagger} L_i \right\} \right) \right)$$

$$(3.63)$$

For the reduced density matrix method, coefficients A and  $B_i$  change, becoming

$$P = \Delta t \cdot (-i[H, \rho - \rho_0]) + \frac{1}{2}(\Delta t)^2 (-\{HH, \rho\} + 2H\rho H)$$
 (3.64)

$$Q_{i} = \Delta t \left( L_{i} \rho L_{i}^{\dagger} - \frac{1}{2} \left\{ \rho, L_{i}^{\dagger} L_{i} \right\} \right) + \frac{1}{2} (\Delta t)^{2} \left( -i \left[ H, L_{i} \rho L_{i}^{\dagger} \right] + \frac{i}{2} \left[ H, \left\{ \rho, L_{i}^{\dagger} L_{i} \right\} \right] - i L_{i} \left[ H, \rho - \rho_{0} \right] L_{i}^{\dagger} + \frac{i}{2} \left\{ \left[ H, \rho \right], L_{i}^{\dagger} L_{i} \right\} \right)$$

$$(3.65)$$

Now Eq. (3.56) can be written more compactly as:

$$\rho(t_{i+1}) = \rho(t_i) + P(t_i) + \sum_{i} \Gamma_i Q_i(t_i) + \sum_{i,j} \Gamma_i \Gamma_j R_{ij}(t_i)$$
(3.66)

At the beginning of each step we calculate P,  $Q_i$  and  $R_{ij}$ , then we find the appropriate  $\{\Gamma_i\}$  such that we match the desired set of expectation values.

#### 3.5.1 Minimization

We wish to minimize the difference between thermal averages of the set of constrained operators  $\{A_k\}$  on the full lattice and on our cluster. This amounts to minimizing the merit function that we define as:

$$r(t_i) = \sqrt{\frac{1}{N_K} \sum_{k} \left| \langle A_k \rangle_{\text{latt}} (t_{i+1}) - \langle A_k \rangle_{\text{clust}} (t_{i+1}) \right|^2}$$
 (3.67)

Where  $N_K$  is the number of operators  $\{A_k\}$ . The average  $\langle A_k \rangle_{\text{clust}}$  is given by

$$\langle A_k \rangle_{\text{clust}} = \text{Tr}(\rho \cdot A_k)$$
 (3.68)

Substituting Eq. (3.56) in and using linearity of the trace we get

$$\langle A_k \rangle_{\text{clust}} (t_{i+1}) = \text{Tr}((\rho(t_i) + P(t_i))A_k) + \sum_i \Gamma_i Tr(Q_i(t_i)A_k) + \sum_{i,j} \Gamma_i \Gamma_j \text{Tr}(R_{ij}(t_i)A_k)$$

$$(3.69)$$

$$\langle A_k \rangle_{\text{clust}} (t_{i+1}) = \langle A_k \rangle_{\text{clust}} (t_i) + \tilde{P}(t_i) + \sum_i \Gamma_i \tilde{Q}_i(t_i) + \sum_{i,j} \Gamma_i \Gamma_j \tilde{R}_{ij}(t_i)$$
 (3.70)

Where  $\tilde{M} = \text{Tr}(MA_k)$ . The merit function  $r(t_i)$  can now be expressed as a function of  $\{\Gamma_i\}$ 

$$r^{2}(t_{i}) = \frac{1}{N_{K}} \sum_{k} \left( -\langle A_{k} \rangle_{\text{latt}} (t_{i+1}) + \langle A_{k} \rangle_{\text{clust}} (t_{i}) + \tilde{P}(t_{i}) + \sum_{i} \Gamma_{i} \tilde{Q}_{i}(t_{i}) + \sum_{i} \Gamma_{i} \Gamma_{j} \tilde{R}_{ij}(t_{i}) \right)^{2}$$

$$(3.71)$$

We perform the minimization numerically using the Nelder-Mead algorithm implemented in the SciPy Python package. [51, 52]

#### 3.6 Choice of jump operators

In general, there is an arbitrary number of possible choices for the set of jump operators. There are however a few guiding principles for making this choice. Firstly, the solutions to the optimization problem should be unique (this can be checked numerically), so the number of  $\Gamma_i$ 's should match the number of constrained operators (counting the real and imaginary parts of complex-valued operators separately).

In the Lindblad equation,  $\Gamma_i$  are non-negative real numbers. To make the optimization problem simpler, we can extend the domain of  $\Gamma_i$  to the real axis  $(\Gamma_i \in \mathbf{R})$  by pairing up conjugate operators:

$$\frac{d\rho(t)}{dt} = -i[H_{\text{clust}}, \rho(t)] + \sum_{i} \left( |\Gamma_{i}|\theta(\Gamma_{i}) \left( L_{i}\rho(t)L_{i}^{\dagger} - \frac{1}{2} \left\{ L_{i}^{\dagger}L_{i}, \rho(t) \right\} \right) + |\Gamma_{i}|\theta(-\Gamma_{i}) \left( L_{i}^{\dagger}\rho(t)L_{i} - \frac{1}{2} \left\{ L_{i}L_{i}^{\dagger}, \rho(t) \right\} \right) \right)$$
(3.72)

Secondly, the jump operators and their  $\Gamma_i$ 's must respect lattice symmetries. For example, if sites i and j are equivalent by symmetry and the operator  $L_i = c_{\sigma,i}$  is present, then  $L_j = c_{\sigma,j}$  must also be included, with  $\Gamma_j = \Gamma_i$ . This reasoning also applies for spin symmetry (if present).

It is also helpful if the physical meaning of jump operators can be easily intuited. In the simple case of 2x1 clusters with constraints on  $X_{\sigma,i,j}$  we have one complex and two purely real constraints (four unknowns). A good starting point for jump operators are the annihilation (and creation) operators of the single particle single-site and plane-wave states

$$\left\{c_{\sigma,0}, \quad c_{\sigma,1}, \quad c_{\sigma,k=0}, \quad c_{\sigma,k=\frac{\pi}{2}}\right\}_{\sigma\in\{\uparrow,\downarrow\}} \tag{3.73}$$

where

$$c_{\sigma,k=0} = c_{\sigma,0} + c_{\sigma,1}, \quad c_{\sigma,k=\frac{\pi}{2}} = c_{\sigma,0} + ic_{\sigma,1}$$

After introducing additional constraints in the form of  $d_i$ , it might be tempting to simply add the operators  $c_{\sigma,i}c_{\sigma,i}$  to Eq. (3.73). In practice we find that such choice leads to problems; at some point in time evolution, there no longer seems to be a solution to the self-consistency condition, and no choice of  $\{\Gamma_i\}$  can be found to make the merit function zero. We interpret this as being related to the operators being insufficiently independent. To alleviate the problem, we separate the action of  $c_{\sigma,i}$  by introducing operators

$$n_{\bar{\sigma},i}c_{\sigma,i}, \quad (1-n_{\bar{\sigma},i})c_{\sigma,i}$$

$$\tag{3.74}$$

The action of these operators is illustrated in Fig. 3.7. After some trial and error for the other operators, we arrive at the set

$$\begin{cases}
(n_{\bar{\sigma},0}c_{\sigma,0}, \quad n_{\bar{\sigma},1}c_{\sigma,1}, \quad (1-n_{\bar{\sigma},0})c_{\sigma,0}, \quad (1-n_{\bar{\sigma},1})c_{\sigma,1}, \\
(1-n_{\bar{\sigma},0})(1-n_{\bar{\sigma},1})c_{\sigma,k=0}, \quad c_{\sigma,k=\frac{\pi}{2}} \end{cases}_{\sigma \in \{\uparrow,\downarrow\}}$$
(3.75)

If we wish to introduce additional non-local density-density constraints  $(n_{\sigma,i}n_{\sigma',j})$ ,

$$\begin{vmatrix} \cdot \rangle \\ | \uparrow \rangle \\ | \uparrow \rangle \\ | \uparrow \downarrow \rangle$$

$$\begin{vmatrix} (1 - n_{\downarrow,i}) c_{\uparrow,i} \\ (1 - n_{\downarrow,i}) c_{\uparrow,i}^{\dagger} \\ n_{\downarrow,i} c_{\uparrow,i} \\ n_{\downarrow,i} c_{\uparrow,i}^{\dagger} \end{vmatrix}$$

Figure 3.7: Effect of  $n_{\bar{\sigma},i}c_{\sigma,i}$  and  $(1-n_{\bar{\sigma},i})c_{\sigma,i}$  on a lattice site.

we use the same jump operators as Eq. (3.75), adding

$$\{(1 - n_{i,\bar{\sigma}})c_{i,\sigma}^{\dagger} \quad i \neq j\}_{\sigma \in \{\uparrow,\downarrow\}}$$
(3.76)

For  $2\times 2$  clusters with  $X_{\sigma,i,j}$  constraints, the jump operators we chose are tailored to the non-equilibrium protocol B, as this allows us significant savings on computation time. Since we have translation symmetry along one direction, e.g. the x direction, the expectation value  $X_{\sigma,\mathbf{r},\mathbf{r}+\mathbf{e_x}}$  is purely real. This means that we need fewer jump operators (the current operator in the form  $c_i + ic_j$  is unnecessary). With reasoning analogous to the  $2x1 \ X_{\sigma,i,j}$  case, we choose

$$\begin{cases}
c_{\sigma,0}, & c_{\sigma,1}, & c_{\sigma,2}, & c_{\sigma,3}, & c_{\sigma,0} + c_{\sigma,1}, & c_{\sigma,2} + c_{\sigma,3}, \\
c_{\sigma,1} + c_{\sigma,2}, & c_{\sigma,0} + c_{\sigma,3}, & c_{\sigma,1} + ic_{\sigma,2}, & c_{\sigma,0} + ic_{\sigma,3}, \\
c_{\sigma,0} + c_{\sigma,1} + c_{\sigma,2} + c_{\sigma,3}, & c_{\sigma,0} + c_{\sigma,1} + ic_{\sigma,2} + ic_{\sigma,3}
\end{cases}_{\sigma \in \{\uparrow,\downarrow\}}$$
(3.77)

with indices  $\{0, 1, 2, 3\}$  as labeled on Fig. 3.8.

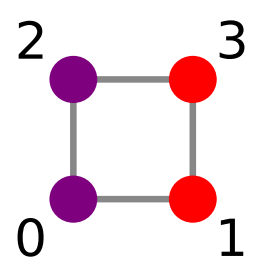


Figure 3.8: A 2x2 cluster in protocol B with labeled sites. The colors denote symmetry equivalent sites

#### 3.7 Limits in which OQCET becomes exact

OQCET is exact in the atomic limit J=0, as the problem is reduced to a sum of individual Hubbard atoms. The solution to the optimization problem is then trivially  $\{\Gamma_i = 0 \quad \forall i\}$ , as the individual atoms are uncoupled.

In the non-interacting limit U=0, the situation is more complicated. Even at U=0, for the cluster evolution to follow lattice EOM nonzero  $\{\Gamma_i\}$  are needed. This coupling introduces correlations into clusters, meaning that  $Y_{\sigma,\mathbf{r},\mathbf{r}'}$  and  $W_{\sigma,\sigma',\mathbf{r},\mathbf{r}'}$  are nonzero. For  $X_{\sigma,\mathbf{r},\mathbf{r}'}$ , the connected parts no longer factor into the equations of motion Eq. (3.27), and they reduce to the exact EOM for the non-interacting problem. This means that  $X_{\sigma,\mathbf{r},\mathbf{r}'}$  is exact in this limit. In the lattice EOM for  $d_{\mathbf{r}}$  (Eq. (3.35)), the  $W_{\sigma,\sigma',\mathbf{r},\mathbf{r}'}$  term does not vanish since it does not depend on U. The nonzero contributions from  $W_{\sigma,\sigma',\mathbf{r},\mathbf{r}'}$  mean that the results for the double occupancy are not exact even at U=0. However, in this limit the Hamiltonian only depends on  $X_{\sigma,\mathbf{r},\mathbf{r}'}$ , giving us exact results for the total energy. Since we are ultimately interested in the susceptibility  $\chi_{\mathbf{q}}(t) \propto \langle \delta n_{\mathbf{q}}(t) \rangle$ , the fact that  $d_{\mathbf{r}}$  is not exact does not affect the final results.

OQCET also becomes exact in the limit of infinite cluster size, as the lattice EOM become equivalent to the Lindblad equation for the single remaining cluster with  $\{\Gamma_i = 0 \ \forall i\}$ . We note that in this limit, the Lindblad equations of motion

for all three initial cluster state methods (Section 3.4.2) reduce to the exact solution, with  $\rho_{\text{clust}} = \rho_{\text{latt}}$ ,  $H_{\text{clust}} = H_{\text{latt}}$  and  $[H, \rho_0] = 0$ .

#### 3.8 Post-processing

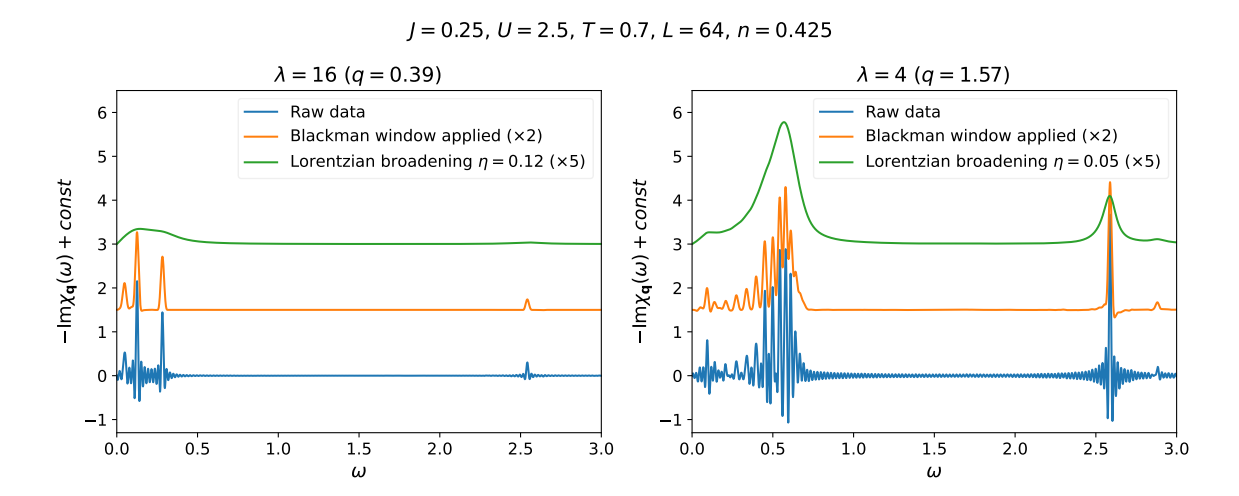


Figure 3.9: Comparison of raw and processed data for two values of  $\lambda$ . At shorter wavelengths the peaks become more dense and smaller broadening is necessary.

The response calculated in OQCET has a discrete spectrum due to the fact that the both the clusters and the lattice have finite size, meaning that the response does not decay in time. At long wavelengths the dynamics become slow, and we only have a response in a narrow range of low frequencies. Because of this, the coupling of clusters to the environment is weak and we observe only a few sharp peaks in the response.

The calculations have a finite cutoff time  $t_{\rm max}$ , so a Fourier transform into the frequency domain will be noisy. To correct for this, we multiply the response with the Blackman window function before performing the Fourier transform. [53] The Blackman window is defined as

$$w(t) = a_0 - a_1 \cos\left(\pi \frac{t - t_{max}}{t_{max}}\right) + a_2 \cos\left(2\pi \frac{t - t_{max}}{t_{max}}\right)$$
(3.78)

with  $a_0 = 7938/18608$ ,  $a_1 = 9240/18608$  and  $a_2 = 1430/18608$ . The cutoff  $t_{max}$  is taken to be long enough such that we remove the noise while preserving discrete peaks in the spectrum.

When comparing with experimental data, to get the system response to decay we have to apply additional broadening, as is standard in ED-based methods. To do so, we perform a convolution of the raw frequency response with the Lorentzian kernel

$$f(\omega) = \frac{1}{\pi \eta \left[ 1 + \left( \frac{\omega}{\eta} \right)^2 \right]}$$
 (3.79)

where  $\eta$  is the broadening width. An example of the post-processing steps can be seen in Fig. 3.9.

## Chapter 4

### Results

All calculations in this chapter were performed for the square-lattice Hubbard model. All the results are presented in the units of bare half-bandwidth D=4J=1. The delta function is approximated with V=1 and  $t_p=0.001$ . The Blackman window cutoff is chosen to be  $t_{max}=200$ .

#### 4.1 Benchmarks

We check the correctness of our implementation of OQCET by benchmarking the lattice differential equation and the Lindbladian cluster evolution against known results.

In the U=0 limit, the lattice differential equations should give exact results for the density. To verify this, we compare the results to bubble calculations which are in this case numerically exact (Fig. 4.1) [54]. This also serves to show that our approximation for the delta potential places us in the linear response regime.

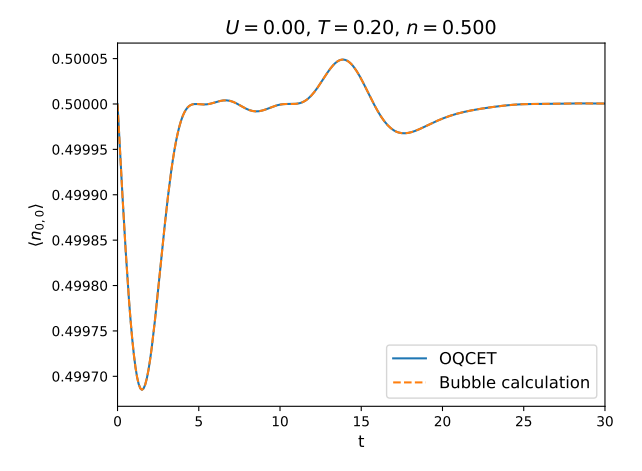


Figure 4.1: Comparison of density response between OQCET differential equations and bubble calculations.

OQCET does not give us exact  $d_{\mathbf{r}}$  in the U=0 limit, but if we evolve the double occupancy by equation Eq. (3.35) with  $W_{\sigma,\sigma',\mathbf{r},\mathbf{r}'}=0$  we expect to get exact results.

For U=0, the double occupancy is simply the square of the density,  $d_{\mathbf{r}}=\langle n_{\mathbf{r}}\rangle^2$ , which we can calculate from the bubble (Fig. 4.2).

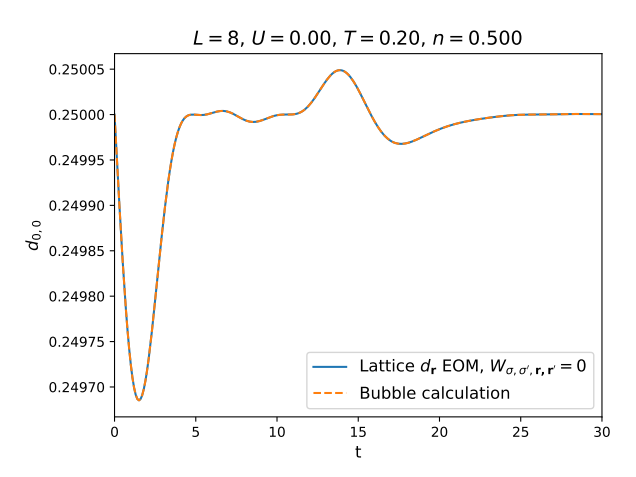


Figure 4.2: Comparison of double occupancy response between lattice differential equations and bubble calculations. The bubble double occupancy is given as the square of the density shown in Fig. 4.1.

To check that the equations for Lindbladian evolution (Section 3.5) have been implemented correctly, we reproduce results for the evolution of a simple two-level system with decay shown in [47]. We compare the OQCET implementation of Eq. (3.66) with code provided in [47] (Fig. 4.3).

The Hamiltonian, initial state and jump operator of the system are given by

$$H = \begin{bmatrix} 0 & \Omega \\ \Omega & E \end{bmatrix}, \quad \rho(t=0) = \begin{bmatrix} 0 & 0 \\ 0 & 1 \end{bmatrix}, \quad L = \sigma^{-} = \begin{bmatrix} 0 & 1 \\ 0 & 0 \end{bmatrix}$$
(4.1)

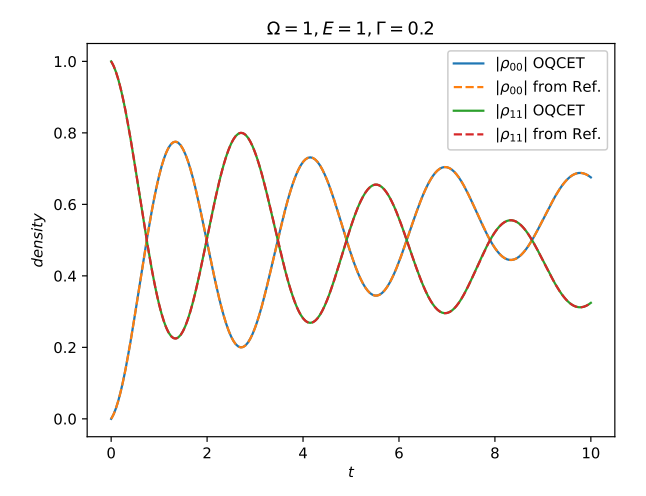


Figure 4.3: Comparison of density evolution of a two level system between OQCET and implementation provided in [47].

#### 4.2 Comparison with exact diagonalization

The 2x2 Hubbard lattice is small enough to be solvable by exact diagonalization (ED). While results obtained from it cannot tell us much about long-wavelength response, it allows us to compare OQCET with numerically exact results. The procedure for exact diagonalization calculations is outlined in Appendix D.

To verify that the differential equations are correct in the interacting case, we compare results obtained by exact diagonalization on a 2x2 lattice with results from our implementation of the equations of motion, given the exact  $Y_{\sigma,\mathbf{r},\mathbf{r}'}$  and  $W_{\sigma,\sigma',\mathbf{r},\mathbf{r}'}$  extracted from ED (Fig. 4.4).

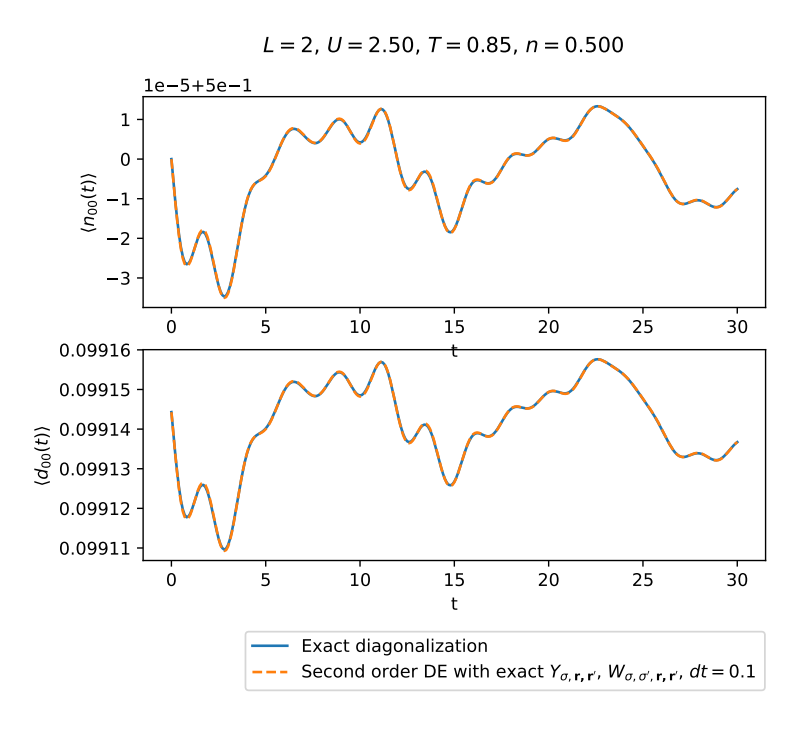


Figure 4.4: Comparison of density and double occupancy evolution for an interacting 2x2 lattice.

When using 2x1 clusters,  $Y_{\sigma,\mathbf{r},\mathbf{r}'}(t)$  is truncated to its nearest-neighbor components. To check the validity of this approximation, we compare results for evolving  $X_{\sigma,\mathbf{r},\mathbf{r}'}$  and  $d_{\mathbf{r}}$  equations of motion using truncated  $Y_{\sigma,\mathbf{r},\mathbf{r}'}(t)$  with exact results (Figs. 4.5 and 4.6). We see that the data are qualitatively similar, while the  $Y_{\sigma,\mathbf{r},\mathbf{r}'}=0$  approximation gives significantly worse results. We see that the next-nearest neighbor Y is not always smaller than the nearest neighbor Y, but it's effect on the EOM is apparently significantly less important.

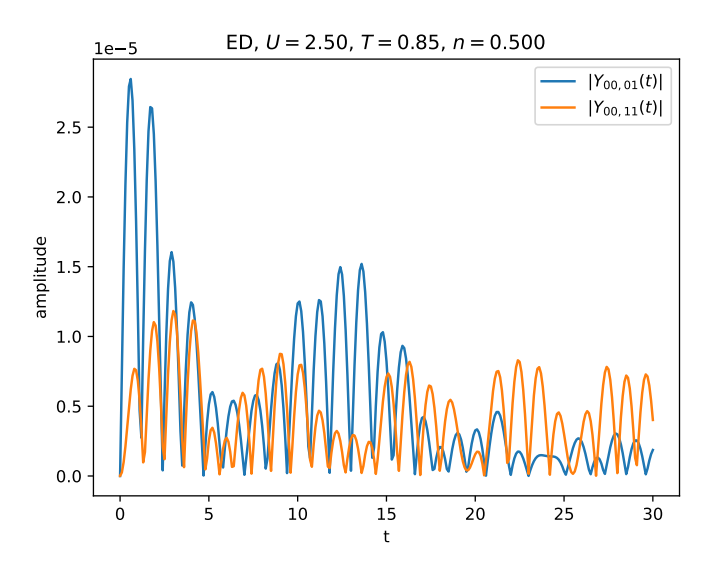


Figure 4.5: Values of nearest and next-nearest neighbor  $Y_{\sigma,\mathbf{r},\mathbf{r}'}(t)$  on a 2x2 lattice

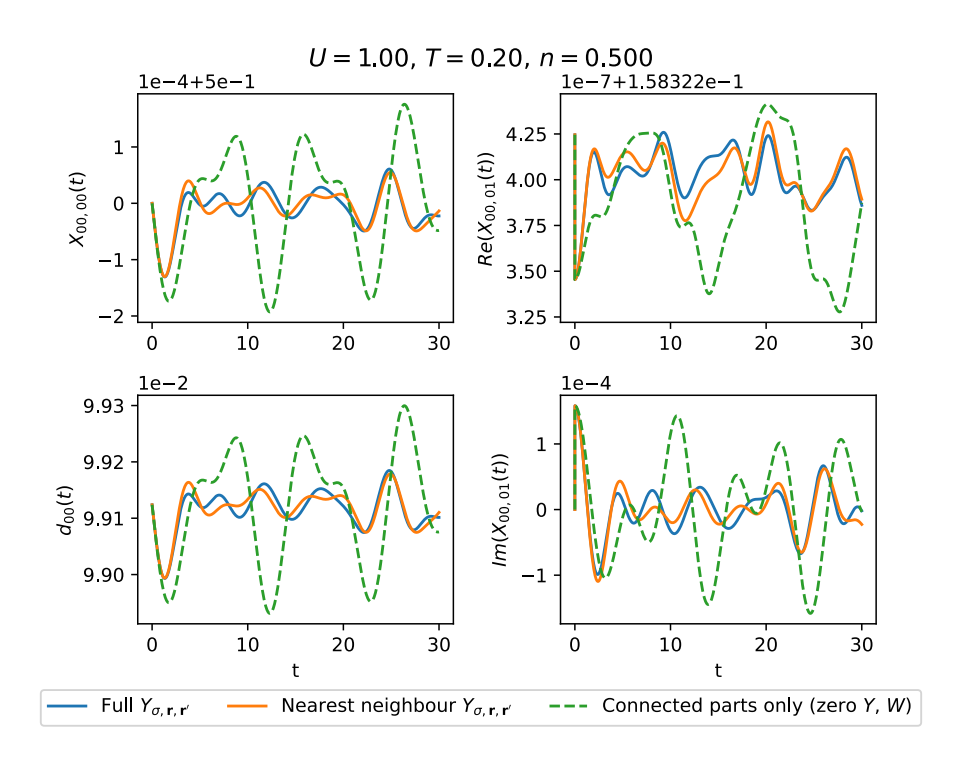


Figure 4.6: Comparison of expectation values between exact diagonalization results and results using truncated  $Y_{\sigma,\mathbf{r},\mathbf{r}'}(t)$  on a 2x2 lattice.  $X_{\sigma,\mathbf{r},\mathbf{r}'}$  and  $d_{\mathbf{r}}$  are obtained from the lattice equations of motion.

#### 4.3 Initial cluster state method

In Section 3.4.2 we introduced three methods for preparing the initial density matrix and the cluster Hamiltonian: using a reduced density matrix with additional environment coupling needed to ensure stationarity in absence of external fields, using a modified Hamiltonian with a thermal state, and using a density matrix with a modified Boltzmann ensemble. We will refer to these three methods as reduced, thermal and weighted.

In Fig. 4.7 we compare the three methods on a 2x2 lattice, which allows us to benchmark them against numerically exact results obtained from ED. We see that  $\chi_q(\omega)$  does not significantly depend on the choice of method. In the following sections, we will use the weighted method to prepare initial states. We also see that the OQCET spectrum is discrete with fewer peaks than the ED case. The discrete spectrum is an artifact of finite cluster size, as discussed in Section 3.8.

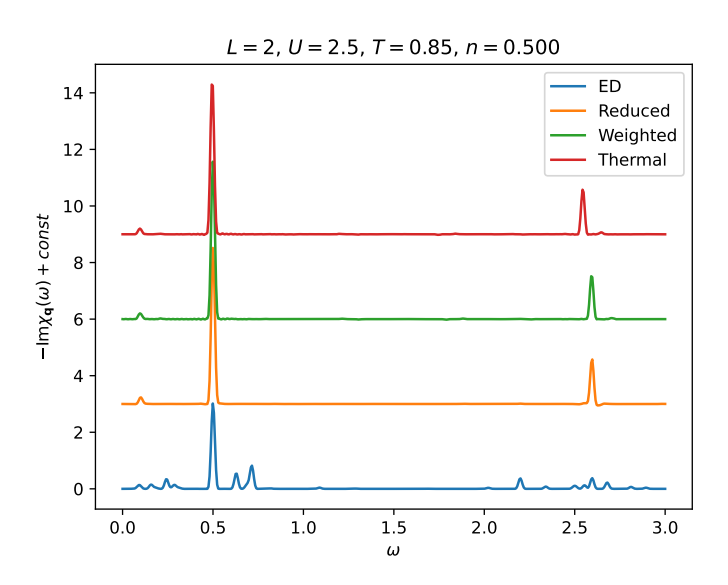


Figure 4.7:  $-\text{Im}\chi_{\mathbf{q}}(\omega)$  for different initial state schemes. (waiting for reduced matrix scheme results)

#### 4.4 Effect of constraints and cluster size

Cluster evolution in OQCET is constrained by operator expectation values  $\{\langle \hat{A}_{\lambda} \rangle\}$ . The choice of operators  $\{\hat{A}_{\lambda}\}$  is arbitrary to a degree—to get charge response it is necessary to place a constraint on the density  $\langle n_i(t) \rangle$ . If we want conservation of energy in our theory it is necessary to include constraints on both  $X_{\sigma,i,j}$  and  $d_i$ . In Fig. 4.8 we compare the charge response for three sets of constrained operators. In the first, we only constrain  $X_{\sigma,i,j}$ . For the second, we constrain both  $X_{\sigma,i,j}$  and  $d_i$ . We see that the latter choice introduces an additional peak in the spectrum. Finally, we include additional constraints on the nearest neighbor density-density correlators  $n_{\sigma,\mathbf{r}}n_{\sigma',\mathbf{r}+\mathbf{u}}$ , but this does not qualitatively change the spectrum. These operators are

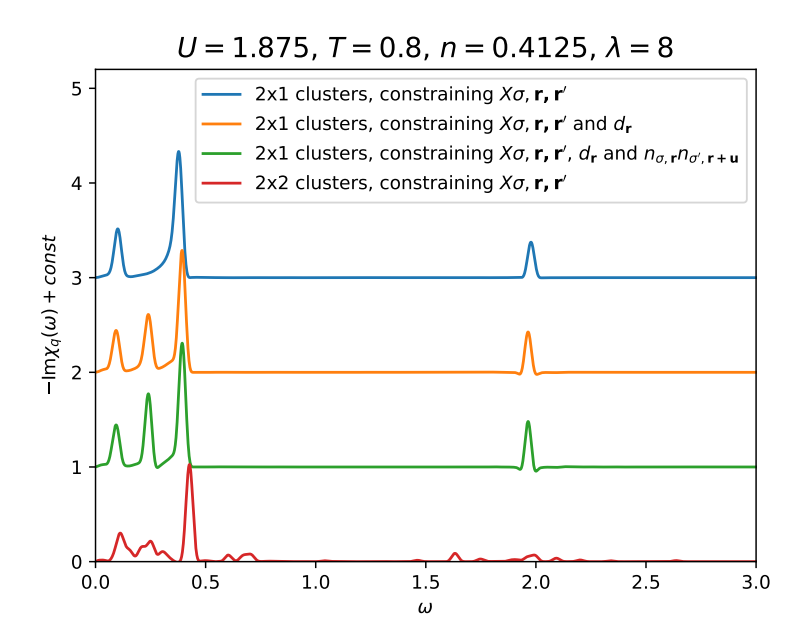


Figure 4.8:  $-\text{Im}\chi_{\mathbf{q}}(\omega)$  for different cluster sizes and choices of constrained operators.

not explicitly present as terms in the Hamiltonian, so they may have a less pronounced effect on system dynamics.

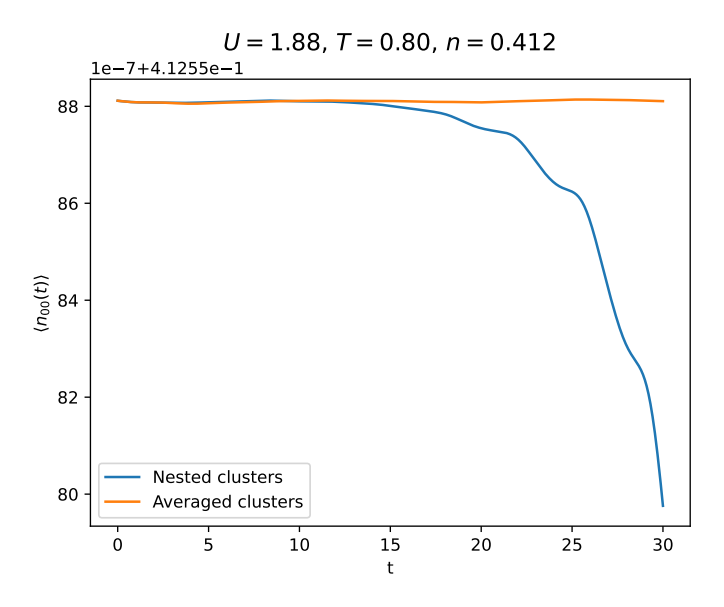


Figure 4.9: Density response for different 2x2 overlap schemes.

To see the effect of cluster size on the charge response, we compare results for 2x1 and 2x2 clusters with constraints on  $X_{\sigma,i,j}$ . There is an additional subtlety when using 2x2 clusters. Nearest-neighbor bonds will generally belong to two (overlapping) 2x2 clusters which might not be equivalent. When using cluster results for  $Y_{\sigma,\mathbf{r},\mathbf{r}'}(\omega)$  and  $W_{\sigma,\sigma',\mathbf{r},\mathbf{r}'}$  on a given bond to close the lattice EOM, the question is which value to use— $Y_{\sigma,\mathbf{r},\mathbf{r}'}(\omega)$  and  $W_{\sigma,\sigma',\mathbf{r},\mathbf{r}'}$  on the given bond might be different when computed from

two clusters to which this bond belongs. We apply two different methods to resolve this ambiguity in two ways—the nested cluster scheme (explained in Section 2.2.2), and a scheme where we average the values of  $Y_{\sigma,\mathbf{r},\mathbf{r}'}(\omega)$  and  $W_{\sigma,\sigma',\mathbf{r},\mathbf{r}'}$  from overlapping clusters. If we try to apply a nested cluster scheme subtracting contributions from 2x1 clusters, the system response very quickly diverges (Fig. 4.9), giving unphysical results. A possible reason for this is that  $Y_{\sigma,\mathbf{r},\mathbf{r}'}(\omega)$  has a discrete spectrum, the contributions from the 2x2 and 2x1 clusters do not cancel out properly; in general, subtracting two discrete spectra with peaks whose positions do not perfectly match results in a non-causal spectrum. This non-causality might drive the system further and further out of equilibrium. If instead we average contributions from overlapping 2x2 clusters, we get a well behaved response (Figs. 4.8 and 4.9).

#### 4.5 Comparison of non-equilibrium protocols

We see that protocols A and B give qualitatively similar results. Away from half-filling, protocol A often diverges, whereas B gives good results. Protocol B requires fewer clusters and preserves more symmetries, which is likely what makes it more stable. Since embedded cluster theories break momentum conservation (as discussed in Section 3.1), we expect to see the response differ somewhat with the choice of protocol.

After applying Lorentzian broadening, the two protocols give nearly identical results. This tells us that the initial response  $\text{Im}\chi_{\mathbf{q}}(t)$  is the same for both protocols.

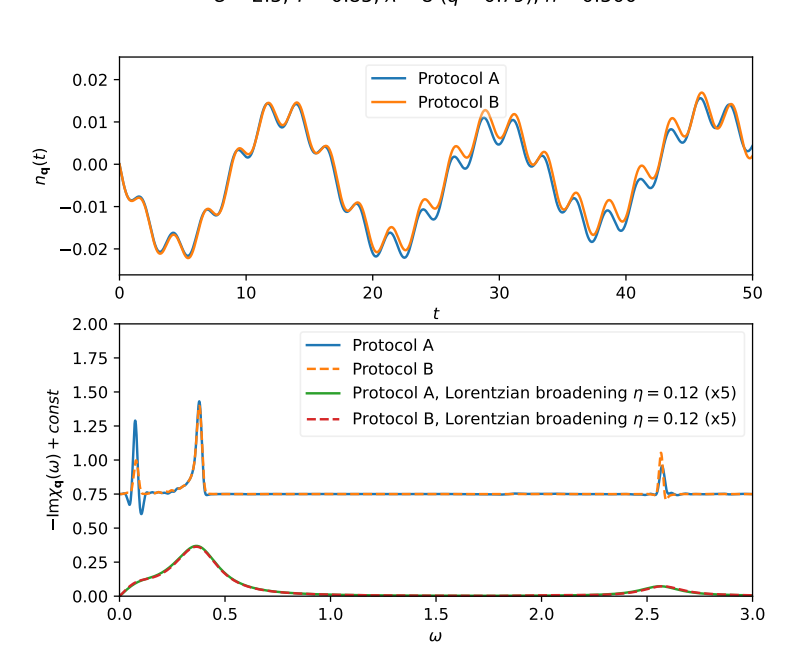


Figure 4.10:  $n_{\mathbf{q}}(t)$  and  $-\mathrm{Im}\chi_{\mathbf{q}}(\omega)$  for non-equilibrium protocols.

#### 4.6 Comparison with other numerical methods

In Fig. 4.11 we compare results for  $\operatorname{Im}\chi_{\mathbf{q}}(\omega)$  between several methods. When comparing OQCET to the equations of motion Eq. (3.27) with  $Y_{\sigma,\mathbf{r},\mathbf{r}'}=0$  we see qualitatively different results: in OQCET we see renormalization of the lower band and the presence of a Hubbard band at  $\omega\approx U$ . The DMFT results only see the Hubbard band, which is expected, as at T=0.02 the system is in a Mott insulating state. At T=0.85 the Mott gap has melted, which explains the presence of the lower band in OQCET. To obtain the entire spectrum, the OQCET results in Fig. 4.11 were obtained by protocol A.

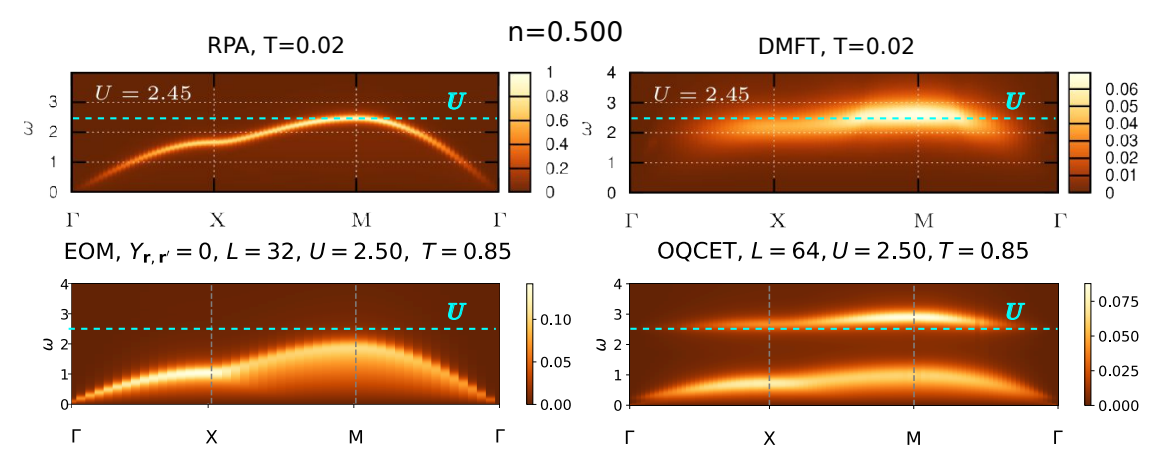


Figure 4.11:  $-\frac{1}{\pi}\text{Im}\chi_{\mathbf{q}}(\omega)$  at half filling. RPA and DMFT results are taken from [55]. EOM refers to equations of motion Eq. (3.27) with connected parts set to zero.

The charge compressibility  $\chi_c = \partial n/\partial \mu$  can be obtained as the limit of the susceptibility

$$\chi_c = -\lim_{\mathbf{q} \to 0} \chi_{\mathbf{q}}(\omega = 0) \tag{4.2}$$

The compressibility  $\chi_c$  is a static quantity, so it can be calculated numerically exactly by Monte Carlo methods such as DQMC. In Fig. 4.12 we see good agreement between OQCET and DQMC results. OQCET overestimates  $\chi_c$  somewhat, but the results become better with increasing temperature, as is expected. Since there is a finite cutoff to our signal, the raw data is oscillatory (Fig. 4.12a) which introduces error to our calculation of  $\chi_c$ . The value of  $\chi_c$  in Fig. 4.12b is taken from the converged value of Blackman window  $\chi_{\bf q}(\omega=0)$  at finite  $\bf q$ . The error is estimated from the width of the oscillations in the raw data.

#### 4.7 Comparison with experimental results

In the experiment performed by Brown et al. [27] <sup>6</sup>Li atoms are placed in an optical lattice simulating the Hubbard model with an external sinusoidal potential

$$H \to H + V \int d\mathbf{r} \sin(xq^*) n(\mathbf{r}) \theta(-t)$$
 (4.3)

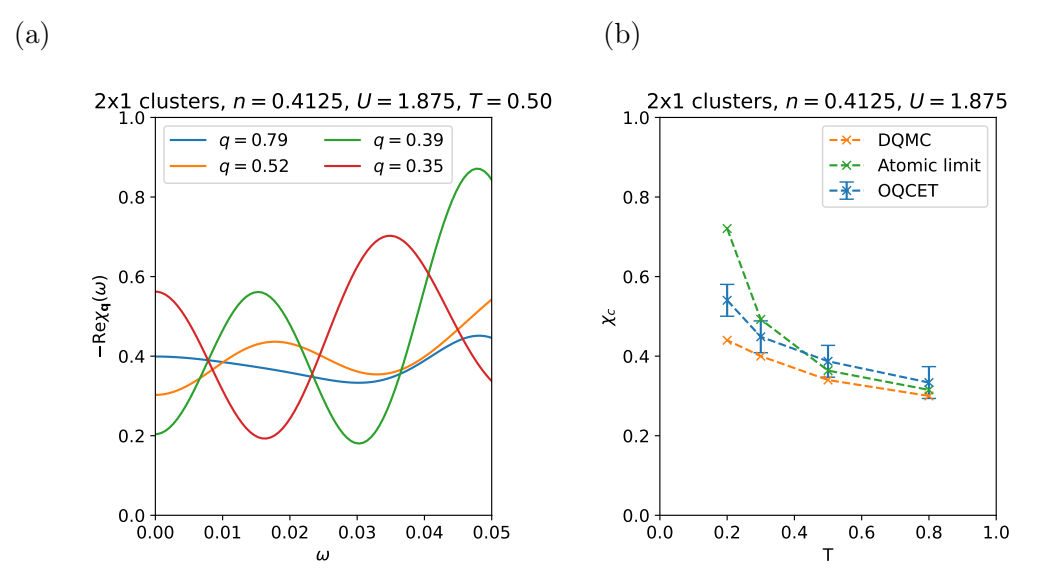


Figure 4.12: (a) Real part of charge susceptibility for different values of  $\mathbf{q}$  (raw data). (b) Comparison of  $\chi_c(T)$  between OQCET, numerically exact DQMC results, and exact diagonalization results in the atomic limit. DQMC results have been taken from [27]

After first thermalizing the system in the external potential, the potential is switched off at t = 0, and the response in the experimental protocol is given by

$$n_{\mathbf{q}}(t) = \int_{-\infty}^{t} dt' \chi_{\mathbf{q}}(t - t') \theta(-t')$$

$$= \int_{t}^{\infty} \chi_{\mathbf{q}}(t') dt'$$
(4.4)

Certain assumptions about hydrodynamic behavior at the longest length and time scales yield an ansatz for the charge susceptibility at long wavelengths and low frequencies [27, 54]

$$\chi_{\mathbf{q}}(\omega) = \frac{\chi_c}{1 - \frac{i\omega}{g^2 D} - \frac{\omega^2}{g^2 D \Gamma}} \tag{4.5}$$

where  $\chi_c$  is the charge compressibility, D is the diffusion constant and  $\Gamma$  is the momentum relaxation rate. The experiment was performed for a range of temperatures and wavelengths of the external potential, and the response was fit to the ansatz Eq. (4.4) to obtain the parameters  $\chi_c$ , D and  $\Gamma$ . The experiment found excellent agreement between experimental data and the hydrodynamic ansatz.

The raw experimental data is not available, so OQCET results shown in Figs. 4.13 and 4.14 are compared with the hydrodynamic ansatz Eq. (4.5) using  $\chi_c$ , D and  $\Gamma$  extracted from experiment. The trends with wavelength and temperature in OQCET are in qualitative agreement with the hydrodynamic theory. The Hubbard peak at  $\omega \approx U$  present in OQCET cannot be described by the ansatz. In the time domain, this

peak corresponds to high frequency oscillations that cannot be seen in the experiment due to the finite time resolution and relatively large error bars. However, this peak is expected to be present, as it can be seen in the optical conductivity spectrum [56] and the spectral function [26]. To get results for individual wavelengths, the OQCET data in Figs. 4.12 to 4.14 was obtained using protocol B.

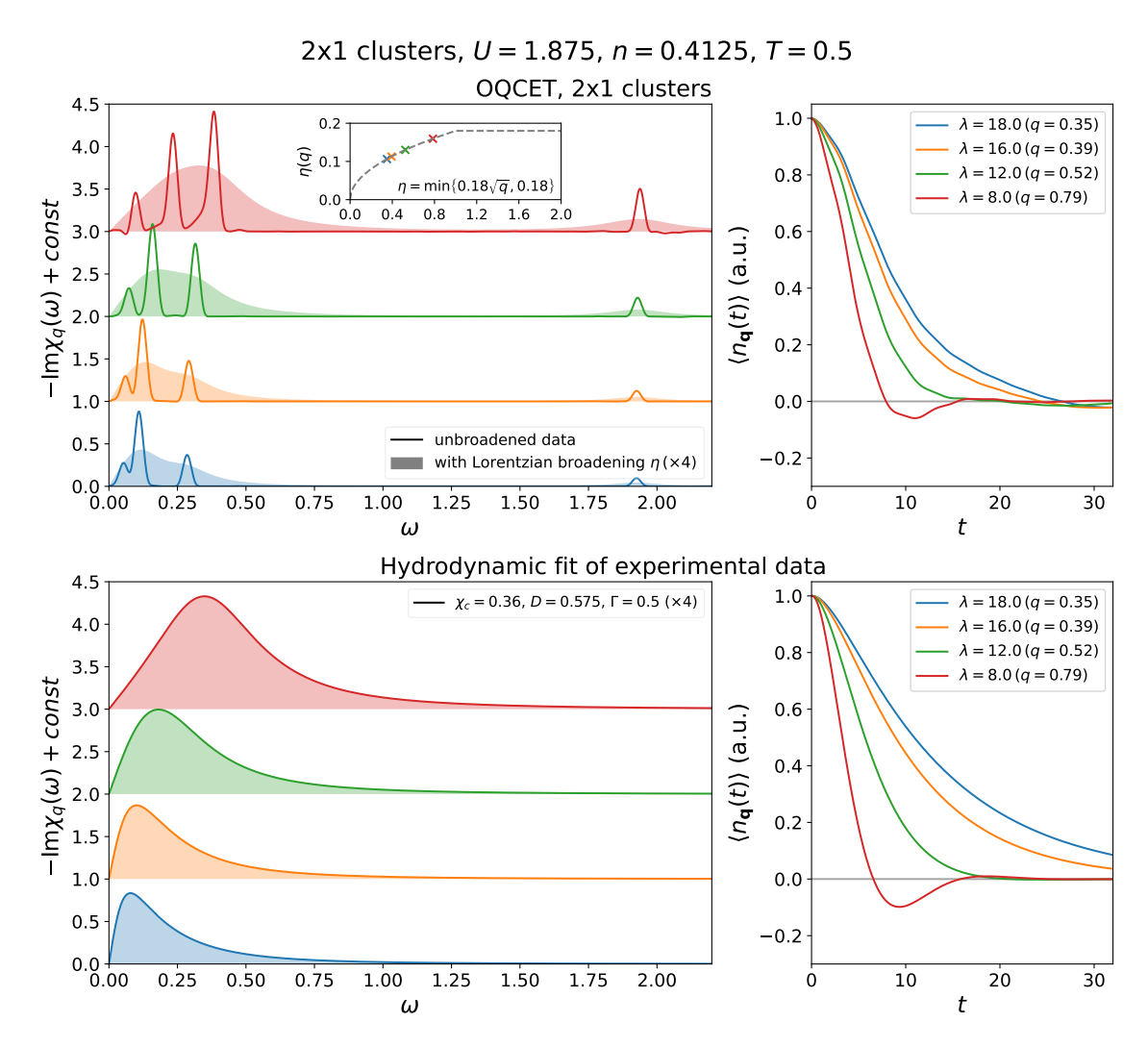


Figure 4.13:  $-\text{Im}\chi_{\mathbf{q}}(\omega)$  and experimental protocol response for different values of the wavelength  $\lambda$  (wavevector q).

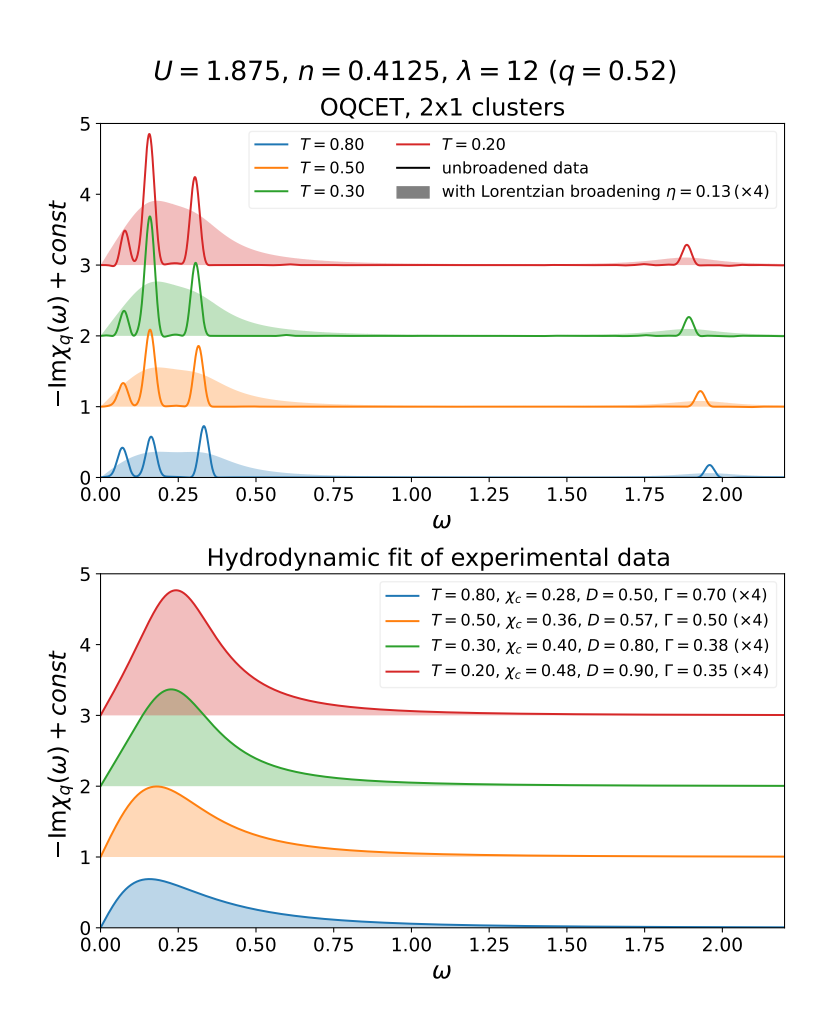


Figure 4.14:  $-{\rm Im}\chi_{\bf q}(\omega)$  for different values of the temperature T.

## Chapter 5

### Conclusions

We have formulated, developed and tested OQCET, an embedded cluster method, based on the exact solution for Lindbladian dynamics of small, open quantum clusters. OQCET becomes formally exact in the atomic, noninteracting and infinite cluster size limits, ensures conservation laws, allows computations for large lattices and avoids analytical continuation. Different versions of the method can be formulated depending on the specifics of the impurity and lattice equations (the choice of constrained and jump operators, the initial density matrix and the impurity Hamiltonian, choice of non-equilibrium protocol). We document the differences in the results obtained by the different versions of the method and identify the most optimal choices for the computation of the quantity of our interest, which is the charge-charge correlation function.

As expected, we find that finite lattice and cluster size necessarily yield a discrete charge-fluctuation spectrum, which is especially evident at long wavelengths. Discrete spectrum means a non-decaying response in real time. Our calculation is formulated in real-time and can only ever be performed up to a finite time; a Fourier transform of a non-decaying function of time given on a finite interval leads to oscillatory artifacts in the frequency domain. In practice, we apply the Blackman window when performing the Fourier transform from time to frequency and obtain precise positions and amplitudes of the peaks. To compare with experimental results, we need to employ additional Lorentzian broadening, as is standard in ED-based methods. We are able to probe large lattices and response at wavelengths of order 20, which is not possible with any straightforward application of ED (or even FTLM). The qualitative agreement with the experiment is solid, which is evidence for the validity of both OQCET and the effective hydrodynamic theory proposed in [27].

In the future we aim to apply OQCET with 2x2 clusters including constraints to the double occupancy. We also plan to use a non-equilibrium protocol involving a pulse of vector potential (as outlined in [28]) to probe the current response and calculate the optical conductivity.

## Appendix A

## Derivation of the Lindblad equation

We derive the Lindblad equation used in cluster evolution from microscopic dynamics, following [47, 57].

We start with a total system with a Hilbert space  $\mathcal{H}_T$ , dividing into the system of interest represented by  $\mathcal{H}$  and the environment  $\mathcal{H}_E$  (Fig. A.1).

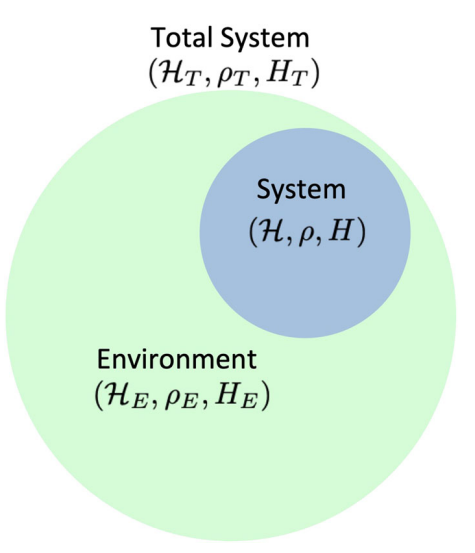


Figure A.1: A schematic representation of the system and environment. [47]

The evolution of the total density matrix is given by the von Neumann equation:

$$\frac{d\rho_T}{dt} = -i[H_T, \rho_T(t)] \tag{A.1}$$

The total Hamiltonian can be decomposed as  $H_T = H_S \otimes \mathbb{1}_E + \mathbb{1}_S \otimes H_E + \alpha H_I$ , with  $\alpha$  representing the strength of the system-environment coupling. The interaction term can be written as

$$H_I = \sum_i S_i \otimes E_i \tag{A.2}$$

with  $S_i \in B(\mathcal{H})$  and  $E_i \in B(\mathcal{H}_E)$  ( $B(\mathcal{H})$  represents the space of bounded linear operators on  $\mathcal{H}$ ).

For the following derivation we will work in the interaction picture. Operators evolve with the system and environment Hamiltonians, while the density matrix evolves by the interaction Hamiltonian:

$$O(t) = e^{i(H+H_E)t}Oe^{-i(H+H_E)t}$$
(A.3)

$$\frac{d\rho_T(t)}{dt} = -i\alpha[H_i(t), \rho_T(t)] \tag{A.4}$$

Integrating the equation we get

$$\rho_T(t) = \rho_T(0) - i\alpha \int_0^t ds [H_I(s), \rho_T(s)]$$
(A.5)

Substituting Eq. (A.5) into Eq. (A.4)

$$\frac{d\rho_T(t)}{dt} = -i\alpha[H_i(t), \rho_T(0)] - \alpha^2 \int_0^t ds [H_I(t), [H_I(s), \rho_T(s)]]$$
 (A.6)

Repeating the procedure once more

$$\frac{d\rho_T(t)}{dt} = -i\alpha[H_i(t), \rho_T(0)] - \alpha^2 \int_0^t ds[H_I(t), [H_I(s), \rho_T(t)]] + O(\alpha^3)$$
 (A.7)

We now have no dependence on the previous states of  $\rho_T(t)$  in time up to order  $\alpha^2$ . We make the approximation that the system is weakly coupled to the environment, and discard orders  $\sim \alpha^3$  and above, leaving us with the equation of motion

$$\frac{d\rho_T(t)}{dt} = -i\alpha[H_i(t), \rho_T(0)] - \alpha^2 \int_0^t ds[H_I(t), [H_I(s), \rho_T(t)]]$$
 (A.8)

To obtain the equation of motion for our system, we trace out the environment degrees of freedom

$$\frac{d\rho(t)}{dt} = \text{Tr}_E\left(\frac{d\rho_T(t)}{dt}\right) = -i\alpha \text{Tr}_E[H_i(t), \rho_T(0)] - \alpha^2 \int_0^t ds \text{Tr}_E[H_I(t), [H_I(s), \rho_T(t)]]$$
(A.9)

The system density matrix still depends on the total density matrix, so we have to make further approximations. We assume that initially, at t=0 the system and environment are decoupled, i.e. the total density matrix is separable,  $\rho_T(0) = \rho(0) \otimes \rho_E(0)$ . We also take the initial environment state to be thermal,  $\rho_E(0) = \exp(-\beta H_E)/Z$ .

With these assumptions we can substitute Eq. (A.2) into the linear-in- $\alpha$  term of Eq. (A.9)

$$\operatorname{Tr}_{E}[H_{i}(t), \rho_{T}(0)] = \sum_{i} (S_{i}(t)\rho(0)\operatorname{Tr}_{E}[E_{i}(t)\rho_{E}(0)] - \rho(0)S_{i}(t)\operatorname{Tr}_{E}[\rho_{E}(0)E_{i}(t)])$$
(A.10)

We can set this term to zero by rewriting our total Hamiltonian  $H_T$  such that  $\langle E_i \rangle = \text{Tr}_E[\rho_E(0)E_i] = 0$ . Our new total Hamiltonian is then  $H_T = H + \alpha \sum_i \langle E_i \rangle S_i + H_E + \alpha H_i'$ , where  $H_i' = \sum_i S_i \otimes (E_i - \langle E_i \rangle)$ . This reduces Eq. (A.9) to

$$\frac{d\rho(t)}{dt} = -\alpha^2 \int_0^t ds \operatorname{Tr}_E[H_I(t), [H_I(s), \rho_T(t)]]$$
(A.11)

To extract a closed equation for  $\rho(t)$  we have to make further approximations. If we take that the environment correlation and relaxation times are much smaller than the characteristic system time scale, we can assume the environment is always in a thermal state and is decoupled from our system,  $\rho_T(t) = \rho(t) \otimes \rho_E(0)$ . From the above equation we then get

$$\frac{d\rho(t)}{dt} = -\alpha^2 \int_0^t ds \operatorname{Tr}_E[H_I(t), [H_I(s), \rho(t) \otimes \rho_E(0)]]$$
(A.12)

The kernel of integration is generally fast-decaying, so we can extend the domain of integration to infinity. A change of the integral variable  $s \to t-s$  gives us the Redfield equation

$$\frac{d\rho(t)}{dt} = -\alpha^2 \int_0^\infty ds \operatorname{Tr}_E[H_I(t), [H_I(t-s), \rho(t) \otimes \rho_E(0)]]$$
 (A.13)

This mapping does not guarantee positivity of the density matrix. To ensure a positive mapping we need to perform the rotating-wave approximation. To do so, we look at the spectrum of the superoperator  $\tilde{H}_S A_S = [H_S, A_S]$  in the Schrödinger picture, denoted by the subscript S. We write the system operators from Eq. (A.2) in the  $\tilde{H}$  eigenbasis:

$$S_{iS} = \sum_{\omega} S_{iS}(\omega) \tag{A.14}$$

where  $S_{iS}(\omega)$  are such that

$$\tilde{H}S_{iS}(\omega) = -\omega S_{iS}(\omega) \tag{A.15}$$

In the interaction picture, following Eq. (A.3), we write  $H_i(t)$  as

$$H_i(t) = e^{i(H+H_E)t} \left( \sum_i S_{iS} \otimes E_{iS} \right) e^{-i(H+H_E)t}$$
(A.16)

in the  $\tilde{H}$  eigenbasis the above becomes

$$H_i(t) = \sum_{i,\omega} e^{-i\omega t} S_{iS}(\omega) \otimes E_i(t) = \sum_{i,\omega} e^{i\omega t} S_{iS}^{\dagger}(\omega) \otimes E_i^{\dagger}(t)$$
 (A.17)

We expand the commutators in Eq. (A.13)

$$\frac{d\rho(t)}{dt} = -\alpha^2 \left[ \int_0^\infty ds \operatorname{Tr}_E[H_I(t)H_I(t-s)(\rho(t) \otimes \rho_E(0))] \right] 
- \int_0^\infty ds \operatorname{Tr}_E[H_I(t)(\rho(t) \otimes \rho_E(0))H_I(t-s)] 
- \int_0^\infty ds \operatorname{Tr}_E[H_I(t-s)(\rho(t) \otimes \rho_E(0))H_I(t)] 
- \int_0^\infty ds \operatorname{Tr}_E[(\rho(t) \otimes \rho_E(0))H_I(t-s)H_I(t)]$$
(A.18)

We now write  $H_I(t-s)$  in terms of  $S_i(\omega)$  and  $H_I(t)$  in terms of  $S_j(\omega')$ . Here we will show the algebra for the first term above, the rest are computed analogously.

$$\int_{0}^{\infty} ds \operatorname{Tr}_{E} \left[ H_{I}(t) H_{I}(t-s) (\rho(t) \otimes \rho_{E}(0)) \right] =$$

$$= \int_{0}^{\infty} ds \operatorname{Tr}_{E} \left[ \sum_{i,j,\omega,\omega'} e^{i\omega't} (S_{iS}^{\dagger}(\omega') \otimes E_{i}^{\dagger}(t)) e^{-i\omega(t-s)} (S_{jS}(\omega) \otimes E_{j}(t-s)) (\rho(t) \otimes \rho_{E}(0)) \right]$$

$$= \sum_{i,j,\omega,\omega'} \operatorname{Tr}_{E} \left[ \int_{0}^{\infty} ds e^{i\omega s} E_{i}^{\dagger}(t) E_{j}(t-s) \rho_{E}(0) \right] e^{i(\omega'-\omega)t} S_{iS}^{\dagger}(\omega') S_{jS}(\omega) \rho(t)$$

$$= \sum_{i,j,\omega,\omega'} \operatorname{Tr}_{E} \left[ \int_{0}^{\infty} ds e^{i\omega s} E_{i}^{\dagger}(t) E_{j}(t-s) \rho_{E}(0) \right] e^{i(\omega'-\omega)t} S_{iS}^{\dagger}(\omega') S_{jS}(\omega) \rho(t)$$
(A.19)

Combining all four terms we get

$$\frac{d\rho(t)}{dt} = \sum_{i,j,\omega,\omega'} \left( e^{i(\omega'-\omega)t} \Lambda_{ij}(\omega) \left[ S_{jS}(\omega)\rho(t), S_{iS}^{\dagger}(\omega') \right] + e^{-i(\omega'-\omega)t} \Lambda_{ji}^{*}(\omega') \left[ S_{jS}(\omega), \rho(t) S_{iS}^{\dagger}(\omega') \right] \right)$$
(A.20)

where

$$\Lambda_{ij}(\omega) = \operatorname{Tr}_{E} \left[ \int_{0}^{\infty} ds e^{i\omega s} E_{i}^{\dagger}(t) E_{j}(t-s) \rho_{E}(0) \right] 
= \operatorname{Tr}_{E} \left[ \int_{0}^{\infty} ds e^{i\omega s} e^{-iH_{E}s} E_{iS}^{\dagger} e^{iH_{E}s} E_{jS} \rho_{E}(0) \right] 
= \int_{0}^{\infty} ds e^{i\omega s} \left\langle E_{i}^{\dagger}(s) E_{j}(0) \right\rangle_{E}$$
(A.21)

We expect the terms with  $|\omega - \omega'| \gg \alpha^2$  to oscillate faster than the characteristic times scale of the system, so in the low-coupling approximation we only take the resonant terms  $\omega = \omega'$  and we get

$$\frac{d\rho(t)}{dt} = \sum_{i,j,\omega} \left( \Lambda_{ij}(\omega) \left[ S_{jS}(\omega)\rho(t), S_{iS}^{\dagger}(\omega) \right] + \Lambda_{ji}^{*}(\omega) \left[ S_{jS}(\omega), \rho(t) S_{iS}^{\dagger}(\omega) \right] \right)$$
(A.22)

We can decompose  $\Lambda_{i,j}$  into Hermitian and non-Hermitian parts to obtain the Hamiltonian and non-Hamiltonian dynamics

$$\pi_{ij} \equiv -\frac{i}{2} \left( \Lambda_{ij}(\omega) - \Lambda_{ij}^*(\omega) \right)$$

$$\gamma_{ij} \equiv \Lambda_{ij}(\omega) + \Lambda_{ij}^*(\omega)$$
(A.23)

Returning to the Schrödinger picture (and omitting the S subscript onwards) we arrive at the

$$\frac{d\rho(t)}{dt} = -i[H + H_{LS}, \rho(t)] + \sum_{\omega, i, j} \gamma_{i, j}(\omega) \left( S_j(\omega) \rho(t) S_i^{\dagger}(\omega) - \frac{1}{2} \left\{ S_i^{\dagger}(\omega) S_j(\omega), \rho(t) \right\} \right)$$
(A.24)

where  $H_{LS} = \sum_{i,j,\omega} \pi_{ij} S_i^{\dagger}(\omega) S_j(\omega)$  is the Lamb shift Hamiltonian, which renormalizes the energy levels of the system. Since  $\left\langle E_i^{\dagger}(s) E_j(0) \right\rangle_E$  is positive,  $\gamma_{ij}$  is also positive, and it can be diagonalized by a transformation  $\tau$ 

$$\tau \gamma(\omega) \tau^{-1} = \begin{pmatrix} \Gamma_1(\omega) & 0 & \cdots \\ 0 & \Gamma_2(\omega) & \cdots \\ \vdots & \vdots & \ddots \end{pmatrix}$$
(A.25)

Rewriting the equation in its diagonal form we get:

$$\frac{d\rho(t)}{dt} = -i[H + H_{LS}, \rho(t)] + \sum_{j,\omega} \Gamma_j(\omega) \left( L_j(\omega)\rho(t)L_j^{\dagger}(\omega) - \frac{1}{2} \left\{ L_j^{\dagger}(\omega)L_j(\omega), \rho(t) \right\} \right)$$
(A.26)

where

$$L_j(\omega) = \sum_{l} \tau_{jl} S_l(\omega) \tag{A.27}$$

Since we are free to choose the environment coupling operators in OQCET, we can choose a real  $\Lambda_{ij}$ . This means the  $\pi_{ij}$  term is zero, and the Lamb shift contribution vanishes. If we then rewrite the sums over i and  $\omega$  as one sum over i we get the well-known form of the Lindblad equation

$$\frac{d\rho(t)}{dt} = -i[H, \rho(t)] + \sum_{i} \Gamma_{i} \left( L_{i}\rho(t)L_{i}^{\dagger} - \frac{1}{2} \left\{ L_{i}^{\dagger}L_{i}, \rho(t) \right\} \right)$$
(A.28)

This is the form that we use for cluster evolution in OQCET.

## Appendix B

# Energy and particle number conservation

To show that OQCET conserves particle number  $N = \sum_{\sigma,\mathbf{r}} X_{\sigma,\mathbf{r},\mathbf{r}'}$  and energy  $E = \langle H \rangle$ , we will show that  $\partial_t N$  and  $\partial_t E$  are zero for any values of  $Y_{\sigma,\mathbf{r}\mathbf{r}'}, W_{\sigma,\sigma',\mathbf{r},\mathbf{r}'}$  extracted from the clusters. Starting from equations Eq. (3.27) conservation of total particle number is easy to show

$$\partial_t N = \sum_{\mathbf{r}, \sigma} \partial_t X_{\sigma, \mathbf{r}, \mathbf{r}} = -iJ \sum_{\mathbf{r}, \mathbf{u}, \sigma} (X_{\sigma, \mathbf{r} - \mathbf{u}, \mathbf{r}} - X_{\sigma, \mathbf{r}, \mathbf{r} + \mathbf{u}})$$
(B.1)

Making the substitution  $\mathbf{r} \to \mathbf{r} - \mathbf{u}$  in the second term we see that the terms cancel out and we have

$$\partial_t N = 0 \tag{B.2}$$

To show conservation of energy we will prove

$$\partial_t E = -J \sum_{\mathbf{r}, \mathbf{u}, \sigma} \partial_t X_{\sigma, \mathbf{r}, \mathbf{r} + \mathbf{u}} - \mu \sum_{\mathbf{r}, \sigma} \partial_t X_{\sigma, \mathbf{r}, \mathbf{r}} + U \sum_{\mathbf{r}} \partial_t d_{\mathbf{r}} = 0$$
 (B.3)

The second term is zero from the conservation of particle number. From Eq. (3.27) we get

$$\sum_{\mathbf{r},\mathbf{u},\sigma} \partial_t X_{\sigma,\mathbf{r},\mathbf{r}+\mathbf{u}} = \sum_{\mathbf{r},\mathbf{u},\sigma} i \left( -J \sum_{\mathbf{u}'} \left( X_{\sigma,\mathbf{r}-\mathbf{u}',\mathbf{r}+\mathbf{u}} - X_{\sigma,\mathbf{r},\mathbf{r}+\mathbf{u}+\mathbf{u}'} \right) + U \left( X_{\bar{\sigma},\mathbf{r},\mathbf{r}} - X_{\bar{\sigma},\mathbf{r}+\mathbf{u},\mathbf{r}+\mathbf{u}} \right) X_{\sigma,\mathbf{r},\mathbf{r}+\mathbf{u}} + Y_{\sigma,\mathbf{r},\mathbf{r}+\mathbf{u}} \right) + U \left( X_{\bar{\sigma},\mathbf{r},\mathbf{r}} - X_{\bar{\sigma},\mathbf{r}+\mathbf{u},\mathbf{r}+\mathbf{u}} \right) X_{\sigma,\mathbf{r},\mathbf{r}+\mathbf{u}} + Y_{\sigma,\mathbf{r},\mathbf{r}+\mathbf{u}} \right)$$
(B.4)

By substituting  $\mathbf{r} \to \mathbf{r} - \mathbf{u}'$  in the term  $\sum_{\mathbf{r},\mathbf{u},\mathbf{u}',\sigma} X_{\sigma,\mathbf{r},\mathbf{r}+\mathbf{u}+\mathbf{u}'}$  the hopping terms cancel out, leaving

$$\sum_{\mathbf{r},\mathbf{u},\sigma} \partial_t X_{\sigma,\mathbf{r},\mathbf{r}+\mathbf{u}} = iU \sum_{\mathbf{r},\mathbf{u},\sigma} \left( \left( X_{\bar{\sigma},\mathbf{r},\mathbf{r}} - X_{\bar{\sigma},\mathbf{r}+\mathbf{u},\mathbf{r}+\mathbf{u}} \right) X_{\sigma,\mathbf{r},\mathbf{r}+\mathbf{u}} + Y_{\sigma,\mathbf{r},\mathbf{r}+\mathbf{u}} \right)$$
(B.5)

A further substitution  $\mathbf{r} + \mathbf{u} \to \mathbf{r}$ , followed by substituting  $\mathbf{u} \to -\mathbf{u}$  in the term  $\sum_{\mathbf{r},\mathbf{u},\sigma} X_{\bar{\sigma},\mathbf{r}+\mathbf{u},\mathbf{r}+\mathbf{u}} X_{\sigma,\mathbf{r},\mathbf{r}+\mathbf{u}}$  gives us the form

$$\sum_{\mathbf{r},\mathbf{u},\sigma} \partial_t X_{\sigma,\mathbf{r},\mathbf{r}+\mathbf{u}} = iU \sum_{\mathbf{r},\mathbf{u},\sigma} \left( \left( X_{\bar{\sigma},\mathbf{r},\mathbf{r}+\mathbf{u}} - X_{\bar{\sigma},\mathbf{r}+\mathbf{u},\mathbf{r}} \right) X_{\sigma,\mathbf{r},\mathbf{r}} + Y_{\sigma,\mathbf{r},\mathbf{r}+\mathbf{u}} \right)$$
(B.6)

Substituting Eq. (B.6) and Eq. (3.35) into Eq. (B.3)

$$\partial_t E = -iJU \sum_{\mathbf{r}} \left( W_{\mathbf{r},\mathbf{r},\uparrow,\downarrow} + \sum_{\sigma,\mathbf{u}} Y_{\sigma,\mathbf{r},\mathbf{r}+\mathbf{u}} \right)$$
 (B.7)

From Eq. (3.33),  $W_{\uparrow,\downarrow,\mathbf{r},\mathbf{r}}$  is given as

$$W_{\uparrow,\downarrow,\mathbf{r},\mathbf{r}} = \left\langle \sum_{\mathbf{u}} \left\{ \left( c_{\uparrow,\mathbf{r}+\mathbf{u}}^{\dagger} c_{\uparrow,\mathbf{r}} - c_{\uparrow,\mathbf{r}}^{\dagger} c_{\uparrow,\mathbf{r}+\mathbf{u}} \right) n_{\downarrow,\mathbf{r}} + n_{\uparrow,\mathbf{r}} \left( c_{\downarrow,\mathbf{r}+\mathbf{u}}^{\dagger} c_{\downarrow,\mathbf{r}} - c_{\downarrow,\mathbf{r}}^{\dagger} c_{\downarrow,\mathbf{r}+\mathbf{u}} \right) \right\} \right\rangle^{\text{conn}}$$

$$\left. + n_{\uparrow,\mathbf{r}} \left( c_{\downarrow,\mathbf{r}+\mathbf{u}}^{\dagger} c_{\downarrow,\mathbf{r}} - c_{\downarrow,\mathbf{r}}^{\dagger} c_{\downarrow,\mathbf{r}+\mathbf{u}} \right) \right\} \right\rangle^{\text{conn}}$$
(B.8)

which can be written as

$$W_{\uparrow,\downarrow,\mathbf{r},\mathbf{r}} = \sum_{\mathbf{u},\sigma} \left\langle \left( c_{\sigma,\mathbf{r}+\mathbf{u}}^{\dagger} c_{\sigma,\mathbf{r}} - c_{\sigma,\mathbf{r}}^{\dagger} c_{\sigma,\mathbf{r}+\mathbf{u}} \right) n_{\bar{\sigma},\mathbf{r}} \right\rangle^{\text{conn}}$$
(B.9)

If we introduce

$$\tilde{W}_{\sigma,\mathbf{r},\mathbf{u}} = \left\langle \left( c_{\sigma,\mathbf{r}+\mathbf{u}}^{\dagger} c_{\sigma,\mathbf{r}} - c_{\sigma,\mathbf{r}}^{\dagger} c_{\sigma,\mathbf{r}+\mathbf{u}} \right) n_{\bar{\sigma},\mathbf{r}} \right\rangle^{\text{conn}}$$
(B.10)

the above can be written as

$$W_{\uparrow,\downarrow,\mathbf{r},\mathbf{r}} = \sum_{\sigma,\mathbf{u}} \tilde{W}_{\sigma,\mathbf{r},\mathbf{u}}$$
 (B.11)

We can then write Eq. (B.7) as

$$\partial_t E = -\frac{1}{2} i J U \sum_{\sigma, \mathbf{r}, \mathbf{u}} \left( \tilde{W}_{\sigma, \mathbf{r}, \mathbf{u}} + \tilde{W}_{\sigma, \mathbf{r} + \mathbf{u}, -\mathbf{u}} + Y_{\sigma, \mathbf{r}, \mathbf{r} + \mathbf{u}} + Y_{\sigma, \mathbf{r} + \mathbf{u}, \mathbf{r}} \right)$$
(B.12)

where we have made the substitutions  $\mathbf{r} \to \mathbf{r} + \mathbf{u}$  and  $\mathbf{u} \to -\mathbf{u}$  to obtain the second  $\tilde{W}$  and Y terms. Applying Eqs. (B.10) and (3.26) we write out the terms in brackets

$$\tilde{W}_{\sigma,\mathbf{r},\mathbf{u}} + \tilde{W}_{\sigma,\mathbf{r}+\mathbf{u},-\mathbf{u}} + Y_{\sigma,\mathbf{r}+\mathbf{u}} + Y_{\sigma,\mathbf{r}+\mathbf{u},\mathbf{r}} = \left\langle \left( c_{\sigma,\mathbf{r}+\mathbf{u}}^{\dagger} c_{\sigma,\mathbf{r}} - c_{\sigma,\mathbf{r}}^{\dagger} c_{\sigma,\mathbf{r}+\mathbf{u}} \right) n_{\bar{\sigma},\mathbf{r}} \right\rangle^{\text{conn}} \\
+ \left\langle \left( c_{\sigma,\mathbf{r}}^{\dagger} c_{\sigma,\mathbf{r}+\mathbf{u}} - c_{\sigma,\mathbf{r}+\mathbf{u}}^{\dagger} c_{\sigma,\mathbf{r}} \right) n_{\bar{\sigma},\mathbf{r}+\mathbf{u}} \right\rangle^{\text{conn}} \\
+ \left\langle c_{\bar{\sigma},\mathbf{r}}^{\dagger} c_{\bar{\sigma},\mathbf{r}} c_{\bar{\sigma},\mathbf{r}}^{\dagger} c_{\sigma,\mathbf{r}+\mathbf{u}} \right\rangle^{\text{conn}} \\
- \left\langle c_{\bar{\sigma},\mathbf{r}+\mathbf{u}}^{\dagger} c_{\bar{\sigma},\mathbf{r}+\mathbf{u}} c_{\bar{\sigma},\mathbf{r}+\mathbf{u}}^{\dagger} c_{\sigma,\mathbf{r}+\mathbf{u}} \right\rangle^{\text{conn}} \\
+ \left\langle c_{\bar{\sigma},\mathbf{r}+\mathbf{u}}^{\dagger} c_{\bar{\sigma},\mathbf{r}+\mathbf{u}} c_{\bar{\sigma},\mathbf{r}+\mathbf{u}}^{\dagger} c_{\sigma,\mathbf{r}} \right\rangle^{\text{conn}} \\
- \left\langle c_{\bar{\sigma},\mathbf{r}}^{\dagger} c_{\bar{\sigma},\mathbf{r}} c_{\bar{\sigma},\mathbf{r}+\mathbf{u}}^{\dagger} c_{\sigma,\mathbf{r}} \right\rangle^{\text{conn}} \tag{B.13}$$

Operators with opposite spins commute, so all the terms in the above equation cancel out and

$$\tilde{W}_{\sigma,\mathbf{r},\mathbf{u}} + \tilde{W}_{\sigma,\mathbf{r}+\mathbf{u},-\mathbf{u}} + Y_{\sigma,\mathbf{r},\mathbf{r}+\mathbf{u}} + Y_{\sigma,\mathbf{r}+\mathbf{u},\mathbf{r}} = 0$$
(B.14)

Since  $\tilde{W}_{\sigma,\mathbf{r},\mathbf{u}}$ ,  $Y_{\sigma,\mathbf{r},\mathbf{r}+\mathbf{u}}$  lie on the same bond (in the same cluster), the identity is valid for all  $\tilde{W}_{\sigma,\mathbf{r},\mathbf{u}}$ ,  $Y_{\sigma,\mathbf{r},\mathbf{r}+\mathbf{u}}$  calculated on clusters. This finally leads us to

$$\partial_t E = 0 \tag{B.15}$$

which we set out to prove.

## Appendix C

# Numerical Matsubara Fourier transform

The Matsubara Green's function is defined as

$$G^{M}(\tau) = -\langle \mathcal{T}_{\tau}c(\tau)c^{\dagger}(0)\rangle \tag{C.1}$$

It can be shown that it is antiperiodic for fermions,

$$G^{M}(\tau) = -G^{M}(\tau + \beta) \tag{C.2}$$

As a consequence, its Fourier transform is discrete, and  $G^M(\tau)$  can be written as a sum of Matsubara frequencies:

$$G^{M}(\tau) = \frac{1}{\beta} \sum_{n=-\infty}^{+\infty} e^{-i\omega_{n}\tau} G^{M}(i\omega_{n})$$
 (C.3)

$$G^{M}(i\omega_{n}) = \int_{0}^{\beta} d\tau e^{i\omega_{n}\tau} G^{M}(\tau)$$
 (C.4)

$$\omega_n = \frac{(2n+1)\pi}{\beta} \tag{C.5}$$

From the form of Eq. (C.3), we see that the double occupancy from Eq. (3.40) can be calculated as the Fourier transform of  $(\beta/U) \sum_{\mathbf{k}} G_{\mathbf{k}}(i\omega_n) \Sigma_{\mathbf{k}}(i\omega_n)$  at time  $\tau = 0^-$ .

A high frequency (Laurent) expansion of  $G^M(i\omega_n)$  demonstrates the issue we would run into if we were to naively try the Fourier transform Eq. (C.3) numerically:

$$G^{M}(i\omega_{n}) = \frac{a}{i\omega_{n}} + \frac{b}{(i\omega_{n})^{2}} + \frac{c}{(i\omega_{n})^{3}} + \frac{d}{(i\omega_{n})^{4}} + O((i\omega_{n})^{5}) , \quad a, b, c, d \in \mathbb{R}$$
 (C.6)

The  $\frac{1}{i\omega_n}$  term is what gives rise to the discontinuity of  $G^M$  at  $\tau=0$ , and because of its very slow decay, it is difficult to capture numerically. To address this, we fit the first few parameters of the Laurent expansion and do these Fourier transforms analytically. The remainder now decays much more rapidly, and its Fourier transform can be computed numerically to a high degree of precision.

The first step is to determine the coefficients a, b, c, d in Eq. (C.6). We first notice that the odd and even powers give imaginary and real contributions to  $G^M$ , respectively. We fit the tails of  $G^M(i\omega_n)$  with the cutoff  $\omega_n > 20$  using a least-squares method. The real and imaginary parts are fit separately with functions

$$f_{\text{Re}} = \frac{b}{(i\omega_n)^2} + \frac{d}{(i\omega_n)^4}$$

$$f_{\text{Im}} = \frac{a}{i\omega_n} + \frac{c}{(i\omega_n)^3}$$
(C.7)

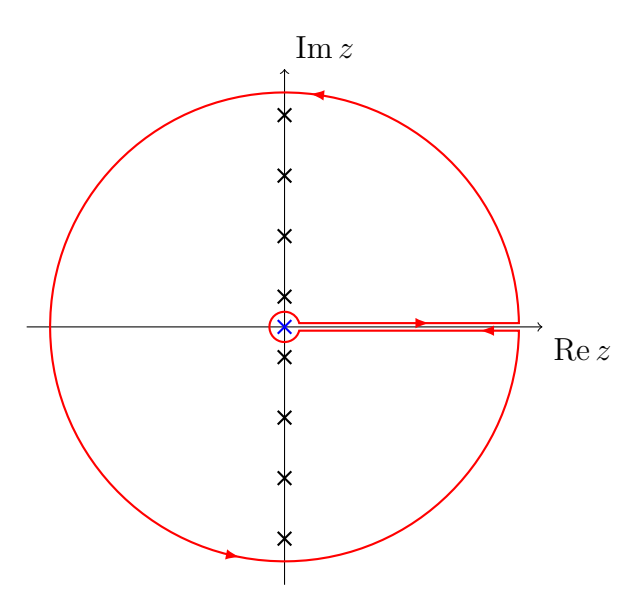


Figure C.1: Keyhole contour for complex integration. Black crosses are poles of g(z), the blue cross represents the pole of h(z).

The analytical Fourier transform of  $1/(i\omega_n)^l$  can be computed by integration along the keyhole contour C shown in Fig. C.1 [58]

$$I = \oint_C h(z)g(z)dz \tag{C.8}$$

where

$$h(z) = \frac{1}{\beta} \frac{e^{-z\tau}}{z^l}$$

$$g(z) = \beta n_f(z) = \frac{\beta}{e^{\beta z} + 1}$$
(C.9)

To simplify calculation, we restrict the domain of  $\tau$  to  $0 \le \tau \le \beta$ . The full function can easily be recovered by Eq. (C.2).

The contour encloses simple poles of g(z) at the Matsubara frequencies. The integral I can be evaluated by Cauchy's residue theorem

$$I = 2\pi i \sum_{i\omega_n} \operatorname{Res}(h(z)g(z)) \Big|_{z=i\omega_n}$$
 (C.10)

Where

$$\operatorname{Res}(f(z))\Big|_{z=z_k} = \frac{1}{(p-1)!} \lim_{z \to z_k} \frac{d^{(p-1)}}{dz^{(p-1)}} ((z-z_k)^p f(z))$$
 (C.11)

is the residue for a pole of order p at  $z = z_k$ . for a simple pole (p = 1) the expression simplifies to

$$\operatorname{Res}(f(z))\Big|_{z=z_k} = \lim_{z \to z_k} ((z - z_k)f(z)) \tag{C.12}$$

 $h(i\omega_n)$  is regular for all n, so

$$\operatorname{Res}(h(z)g(z))\Big|_{z=i\omega_n} = h(i\omega_n)\operatorname{Res}(g(z))\Big|_{z=i\omega_n}$$
 (C.13)

The residue of g(z) is easily computed

$$\operatorname{Res}(g(z))\Big|_{z=i\omega_n} = \lim_{z \to i\omega_n} (z - i\omega_n) \frac{\beta}{e^{\beta z} + 1}$$

$$= \lim_{\eta \to 0} \frac{\beta \eta}{e^{\beta(\eta + i\omega_n)} + 1}$$

$$= \lim_{\eta \to 0} \frac{\beta \eta}{-e^{\beta \eta} + 1}$$

$$= \lim_{\eta \to 0} \frac{\beta \eta}{-1 - \beta \eta + 1}$$

$$= -1$$
(C.14)

where we have used that  $e^{\beta(i\omega_n)} = -1$ , which follows directly from Eq. (C.5). This gives us

$$I = \frac{-2\pi i}{\beta} \sum_{i\omega_n} \frac{e^{-i\omega_n \tau}}{(i\omega_n)^l} \tag{C.15}$$

Next we wish to show that the integral over the outer circle of the contour vanishes as the outer radius goes to infinity (i.e. that as  $|z| \to \infty$ , g(z)h(z) goes to zero faster than  $|z|^{-1}$ ). For Rez > 0, g(z)h(z)  $e^{-|z|\tau}$ , while when Rez < 0, g(z)h(z)  $e^{|z|(\tau-\beta)}$ . Since  $0 \le \tau \le \beta$ , the integrand vanishes exponentially as  $|z| \to \infty$ . This means the only nonzero contribution to the integral is along the small circular contour around z = 0. This can be evaluated by the residue theorem, this time enclosing only the pole at z = 0 (with an additional minus sign, as the contour is oriented clockwise)

$$\begin{split} I &= -2\pi i \operatorname{Res}(h(z)g(z))\Big|_{z=0} \\ &= -2\pi i \operatorname{Res}(h(z)g(z))\Big|_{z=0} \\ &= -2\pi i \operatorname{Res}(\frac{1}{\beta} \frac{e^{-z\tau}}{z^{l}} \frac{\beta}{e^{\beta z} + 1})\Big|_{z=0} \\ &= -2\pi i \frac{1}{(l-1)!} \lim_{z \to 0} \frac{d^{(l-1)}}{dz^{(l-1)}} \left(z^{l} \frac{e^{-z\tau}}{z^{l} e^{\beta z} + 1}\right) \\ &= -2\pi i \frac{1}{(l-1)!} \lim_{z \to 0} \frac{d^{(l-1)}}{dz^{(l-1)}} \left(\frac{e^{-z\tau}}{e^{\beta z} + 1}\right) \end{split}$$
(C.16)

Equating Eq. (C.15) and Eq. (C.16)

$$\frac{1}{\beta} \sum_{i\omega_n} \frac{e^{-i\omega_n \tau}}{(i\omega_n)^l} = \frac{1}{(l-1)!} \lim_{z \to 0} \frac{d^{(l-1)}}{dz^{(l-1)}} \left( \frac{e^{-z\tau}}{e^{\beta z} + 1} \right) \\
= \frac{1}{(l-1)!} \lim_{z \to 0} \sum_k \binom{l-1}{k} \left( \frac{d^k}{dz^k} e^{-z\tau} \right) \left( \frac{d^{(l-1-k)}}{dz^{(l-1-k)}} \frac{1}{e^{\beta z} + 1} \right)$$
(C.17)

The *n*-th derivative of  $1/(e^w + 1)$  can be written as a sum

$$\frac{d^n}{dw^n} \frac{1}{e^w + 1} = \sum_{m=0}^n C_m^n \frac{e^{mw}}{(1 + e^w)^{m+1}}$$
 (C.18)

where  $C_n^m$  are coefficients to be determined. From the above definition, it directly follows that  $C_0^0 = 1$  (taking m = 0, the sum only has one term). Taking the derivative of both sides we get

$$\frac{d^{n+1}}{dw^{n+1}} \frac{1}{e^w + 1} = \sum_{m=0}^{n} C_m^m \frac{d}{dn} \left( \frac{e^{mw}}{(1 + e^w)^{m+1}} \right)$$

$$\sum_{m=0}^{n+1} C_m^{m+1} \frac{e^{mw}}{(1 + e^w)^{m+1}} = \sum_{m=0}^{n} C_m^m \left( \frac{me^{mw}}{(1 + e^w)^{m+1}} - \frac{(m+1)e^{(m+1)w}}{(1 + e^w)^{m+2}} \right)$$

$$\sum_{m=0}^{n+1} C_m^{m+1} \frac{e^{mw}}{(1 + e^w)^{m+1}} = \sum_{m=0}^{n} mC_m^n \frac{e^{mw}}{(1 + e^w)^{m+1}} - \sum_{m=1}^{n+1} mC_{m-1}^n \frac{e^{mw}}{(1 + e^w)^{m+1}}$$
(C.19)

where we have made the substitution  $m \to m+1$  in the second term. Equating terms in the sum we get the recurrence relations

$$C_m^{n+1} = mC_m^n - mC_{m-1}^n, 0 \le m \le n$$

$$C_{n+1}^{n+1} = (n+1)C_n^n (C.20)$$

Introducing  $S_m^n = \frac{(-1)^m}{m!} C_m^n$ , we see that  $S_m^n$  satisfy the recursion relation for Stirling numbers of the second kind,

$$S_m^{n+1} = mS_m^n + S_{m-1}^n (C.21)$$

In the literature, Stirling numbers of the second kind  $S_m^n$  are usually written as  $\binom{n}{m}$ , and we will employ that notation onwards. Performing the substitution  $w = \beta z$ , by the chain rule we have  $\frac{d}{dw} = \beta \frac{d}{dz}$  and Eq. (C.18) now reads

$$\frac{d^n}{dz^n} \frac{1}{e^{\beta z} + 1} = \beta^n \sum_{m=0}^n (-1)^m m! \binom{n}{m} \frac{e^{mz}}{(1 + e^z)^{m+1}}$$
(C.22)

Finally, substituting this equation into Eq. (C.17) and using  $\binom{n}{k} = \frac{n!}{k!(n-k)!}$ 

$$\frac{1}{\beta} \sum_{i \in \mathbb{Z}} \frac{e^{-i\omega_n \tau}}{(i\omega_n)^l} = \sum_{k=0}^{l-1} \sum_{m=0}^{l-1-k} {l-1-k \choose m} \frac{(-1)^k \beta^{l-1-k} m!}{2^{m+1} k! (l-1-k)!} \tau^k$$
 (C.23)

Defining  $\mathcal{F}(\frac{1}{(i\omega_n)^l}) \equiv \frac{1}{\beta} \sum_{i\omega_n} \frac{e^{-i\omega_n\tau}}{(i\omega_n)^l}$ , Fourier transforms of the first four terms in the Laurent series read as follows:

$$\mathcal{F}\left(\frac{1}{i\omega_n}\right) = -\frac{1}{2}$$

$$\mathcal{F}\left(\frac{1}{(i\omega_n)^2}\right) = \frac{1}{4}(2\tau - \beta)$$

$$\mathcal{F}\left(\frac{1}{(i\omega_n)^3}\right) = \frac{1}{4}(\beta\tau - \tau^2)$$

$$\mathcal{F}\left(\frac{1}{(i\omega_n)^4}\right) = \frac{1}{12}\left(\tau^3 - \frac{3}{2}\beta\tau^2 + \frac{1}{4}\beta^3\right)$$
(C.24)

The remainder  $\tilde{G}^{M}(i\omega_{n})$  we calculate by simple subtraction

$$\tilde{G}^{M}(i\omega_{n}) = G^{M}(i\omega_{n}) - \left(\frac{a}{i\omega_{n}} + \frac{b}{(i\omega_{n})^{2}} + \frac{c}{(i\omega_{n})^{3}} + \frac{d}{(i\omega_{n})^{4}}\right)$$
(C.25)

Eq. (C.3) can be rewritten as in terms of the discrete Fourier transform:

$$\tilde{G}^{M}(\tau) = \frac{1}{\beta} \sum_{n=-N}^{N} e^{-i\omega_{n}\tau} \tilde{G}^{M}(i\omega_{n})$$

$$= \frac{1}{\beta} e^{-i\pi\frac{\tau}{\beta}} \sum_{n=-N}^{N} e^{-i2\pi\frac{\tau}{\beta}n} \tilde{G}^{M}(i\omega_{n})$$
(C.26)

where we have truncated the Matsubara frequencies to the first N terms. This gives us  $\tilde{G}^M(\tau)$  at 2N equally spaced points on the interval  $[0,\beta)$ . Finally, summing all the terms we obtain  $G^M(\tau)$ 

$$G^{M}(\tau) = -\frac{a}{2} + \frac{b}{4} (2\tau - \beta) + \frac{c}{4} (\beta \tau - \tau^{2}) + \frac{d}{12} \left(\tau^{3} - \frac{3}{2}\beta \tau^{2} + \frac{1}{4}\beta^{3}\right) + \tilde{G}^{M}(\tau) \quad (C.27)$$

## Appendix D

## Exact diagonalization

To benchmark the results obtained from OQCET we can use numerically exact results obtained by exact diagonalization (ED). ED is limited to very small systems (we use a 2x2 cluster, which has very pronounced finite-size effects) but it nevertheless provides us with a good starting point for benchmarking.

We first diagonalize the unperturbed Hamiltonian H. In its eigenbasis, the Hamiltonian can be expressed as:

$$H_{\text{diag}} = P^{-1}H_{\text{fock}}P\tag{D.1}$$

where  $H_{\text{fock}}$  is the matrix representing the Hamiltonian in the Fock basis. We start from a thermal state

$$\rho = \frac{1}{Z} \sum_{\Psi} e^{-\beta E_{\Psi}} |\Psi\rangle \langle \Psi| \tag{D.2}$$

We introduce a perturbation  $\propto \Pi(t, t_p, V)$  (Eq. (3.17)) which is piecewise constant in time. The next step is to diagonalize the perturbed Hamiltonian H' and obtain its eigenstates  $|\chi\rangle$ .

$$H'_{\text{diag}} = P'^{-1}H'_{\text{fock}}P' \tag{D.3}$$

The eigenstates  $|\chi\rangle$  evolve as

$$|\chi(t)\rangle = e^{-iE_{\chi}t} |\chi(0)\rangle$$
 (D.4)

From this it follows that the density operator evolves as

$$\rho(t) = \frac{1}{Z} \sum_{\chi,\chi'} e^{-i(E_{\chi} - E_{\chi'})t} a_{\chi\chi'} |\chi(0)\rangle \langle \chi'(0)|$$
(D.5)

where  $|\chi(0)\rangle$  are eigenstates of H'. An operator A transforms under a change of basis as follows:

$$A' = M^{-1}AM \tag{D.6}$$

Therefore, to obtain our density matrix in the perturbed Hamiltonian eigenspace, we must first transform from the H eigenspace to the fock space by the change of basis matrix  $P^{-1}$ , then apply the change of basis by P'.

$$\rho_{\text{fock}} = P \rho_H P^{-1}$$

$$\rho_{H'} = P'^{-1} \rho_{\text{fock}} P'$$
(D.7)

Once we have reached  $t_p$ , the perturbation switches off and we once again have our unperturbed Hamiltonian H. We now transform back into the H eigenspace, and  $\rho(t)$  is given as

$$\rho(t) = \frac{1}{Z} \sum_{\Psi, \Psi'} e^{-i(E_{\Psi} - E_{\Psi'})t} a_{\Psi\Psi'} |\Psi(t_p)\rangle \langle \Psi'(t_p)|, \qquad t > t_p$$
 (D.8)

## Bibliography

- [1] A. Georges. "Strongly Correlated Electron Materials: Dynamical Mean-Field Theory and Electronic Structure". In: *AIP Conference Proceedings*. Vol. 715. AIP, 2004, pp. 3–74. DOI: 10.1063/1.1800733.
- [2] G. Kotliar and D. Vollhardt. "Strongly Correlated Materials: Insights From Dynamical Mean-Field Theory". In: *Physics Today* 57.3 (Mar. 2004), pp. 53–59. ISSN: 1945-0699. DOI: 10.1063/1.1712502.
- [3] B. Keimer et al. "From quantum matter to high-temperature superconductivity in copper oxides". In: *Nature* 518.7538 (Feb. 2015), pp. 179–186. ISSN: 1476-4687. DOI: 10.1038/nature14165.
- [4] T. Furukawa et al. "Quantum criticality of Mott transition in organic materials". In: Nature Physics 11.3 (Feb. 2015), pp. 221–224. ISSN: 1745-2481. DOI: 10.1038/nphys3235.
- [5] Y. Kurosaki et al. "Mott Transition from a Spin Liquid to a Fermi Liquid in the Spin-Frustrated Organic Conductor κ-(ET)<sub>2</sub>Cu<sub>2</sub>(CN)<sub>3</sub>". In: *Physical Review Letters* 95.17 (Oct. 2005). ISSN: 1079-7114. DOI: 10.1103/physrevlett.95. 177001.
- [6] H. Menke et al. "Superconductivity and Mott Physics in Organic Charge Transfer Materials". In: *Physical Review Letters* 133.13 (Sept. 2024). ISSN: 1079-7114. DOI: 10.1103/physrevlett.133.136501.
- [7] A. Fischer et al. "Unconventional superconductivity in magic-angle twisted trilayer graphene". In: npj Quantum Materials 7.1 (Jan. 2022). ISSN: 2397-4648. DOI: 10.1038/s41535-021-00410-w.
- [8] Z. Zhou et al. Double-dome Unconventional Superconductivity in Twisted Trilayer Graphene. 2024. arXiv: 2404.09909 [cond-mat.mes-hall].
- [9] Y. Cao et al. "Strange Metal in Magic-Angle Graphene with near Planckian Dissipation". In: *Physical Review Letters* 124.7 (Feb. 2020). ISSN: 1079-7114. DOI: 10.1103/physrevlett.124.076801.
- [10] V. J. Emery. "Theory of high-T<sub>c</sub> superconductivity in oxides". In: *Physical Review Letters* 58.26 (June 1987), pp. 2794–2797. ISSN: 0031-9007. DOI: 10.1103/physrevlett.58.2794.

- [11] L. F. Mattheiss. "Electronic band properties and superconductivity in La<sub>2-y</sub>X<sub>y</sub>CuO<sub>4</sub>". In: *Physical Review Letters* 58.10 (Mar. 1987), pp. 1028–1030. ISSN: 0031-9007. DOI: 10.1103/physrevlett.58.1028.
- [12] B. Bacq-Labreuil et al. "Toward an Ab Initio Theory of High-Temperature Superconductors: A Study of Multilayer Cuprates". In: *Physical Review X* 15.2 (May 2025). ISSN: 2160-3308. DOI: 10.1103/physrevx.15.021071.
- [13] E. Pavarini et al. "Band-Structure Trend in Hole-Doped Cuprates and Correlation with T<sub>c max</sub>". In: *Physical Review Letters* 87.4 (July 2001). ISSN: 1079-7114. DOI: 10.1103/physrevlett.87.047003.
- [14] R. Raimondi, J. H. Jefferson, and L. F. Feiner. "Effective single-band models for the high-T<sub>c</sub> cuprates. II. Role of apical oxygen". In: *Physical Review B* 53.13 (Apr. 1996), pp. 8774–8788. ISSN: 1095-3795. DOI: 10.1103/physrevb.53.8774.
- [15] Y. Ohta, T. Tohyama, and S. Maekawa. "Apex oxygen and critical temperature in copper oxide superconductors: Universal correlation with the stability of local singlets". In: *Physical Review B* 43.4 (Feb. 1991), pp. 2968–2982. ISSN: 1095-3795. DOI: 10.1103/physrevb.43.2968.
- [16] M. R. Norman et al. "Destruction of the Fermi surface in underdoped high-Tc superconductors". In: *Nature* 392.6672 (Mar. 1998), pp. 157–160. ISSN: 1476-4687. DOI: 10.1038/32366.
- [17] I. E. Trofimov et al. "Growth and properties of  $La_{2-x}Sr_xCuO_4$  films". In: *Applied Physics Letters* 65.19 (Nov. 1994), pp. 2481–2483. ISSN: 1077-3118. DOI: 10.1063/1.112671.
- [18] J. M. Tarascon et al. "Superconductivity at 40 K in the Oxygen-Defect Perovskites  $La_{2-x}Sr_xCuO_{4-y}$ ". In: *Science* 235.4794 (Mar. 1987), pp. 1373–1376. ISSN: 1095-9203. DOI: 10.1126/science.235.4794.1373.
- [19] C. Chaillout et al. "The crystal structure of superconducting  $La_2CuO_{4.032}$  by neutron diffraction". In: *Physica C: Superconductivity* 158.1-2 (Apr. 1989), pp. 183–191. ISSN: 0921-4534. DOI: 10.1016/0921-4534(89)90315-8.
- [20] X. Y. Tee et al. "Two superconducting transitions in single-crystal  $La_{2-x}Ba_xCuO_4$ ". In: *Physical Review B* 95.5 (Feb. 2017). ISSN: 2469-9969. DOI: 10 . 1103 / physrevb.95.054516.
- [21] P. Limelette et al. "Mott Transition and Transport Crossovers in the Organic Compound  $\kappa$ —(BEDT-TTF)<sub>2</sub>Cu[N(CN)<sub>2</sub>]Cl". In: *Physical Review Letters* 91.1 (July 2003). ISSN: 1079-7114. DOI: 10.1103/physrevlett.91.016401.
- [22] R. H. McKenzie. "Similarities Between Organic and Cuprate Superconductors".
   In: Science 278.5339 (Oct. 1997), pp. 820–821. ISSN: 1095-9203. DOI: 10.1126/science.278.5339.820.
- [23] T. Isono et al. "Quantum criticality in an organic spin-liquid insulator  $\kappa$  (BEDT TTF)<sub>2</sub>Cu<sub>2</sub>(CN)<sub>3</sub>". In: *Nature Communications* 7.1 (Nov. 2016). ISSN: 2041-1723. DOI: 10.1038/ncomms13494.

- [24] A. Georges et al. "Dynamical mean-field theory of strongly correlated fermion systems and the limit of infinite dimensions". In: *Reviews of Modern Physics* 68.1 (Jan. 1996), pp. 13–125. ISSN: 1539-0756. DOI: 10.1103/revmodphys.68.13.
- [25] M. Qin et al. "The Hubbard Model: A Computational Perspective". In: Annual Review of Condensed Matter Physics 13.1 (Mar. 2022), pp. 275–302. ISSN: 1947-5462. DOI: 10.1146/annurev-conmatphys-090921-033948.
- [26] J. Vučičević et al. "Bad-Metal Behavior Reveals Mott Quantum Criticality in Doped Hubbard Models". In: *Physical Review Letters* 114.24 (June 2015). ISSN: 1079-7114. DOI: 10.1103/physrevlett.114.246402.
- [27] P. T. Brown et al. "Bad metallic transport in a cold atom Fermi-Hubbard system". In: *Science* 363.6425 (Jan. 2019), pp. 379–382. ISSN: 1095-9203. DOI: 10.1126/science.aat4134.
- [28] J. Kovačević, M. Ferrero, and J. Vučičević. "Toward Numerically Exact Computation of Conductivity in the Thermodynamic Limit of Interacting Lattice Models". In: *Physical Review Letters* 135.1 (July 2025). ISSN: 1079-7114. DOI: 10.1103/mm38-zttx.
- [29] Y. Eom et al. Strange diffusivity of incoherent metal in half-filled twodimensional Hubbard model. 2025. arXiv: 2509.00281 [cond-mat.str-el].
- [30] J. Vučičević et al. "Conductivity in the Square Lattice Hubbard Model at High Temperatures: Importance of Vertex Corrections". In: *Physical Review Letters* 123.3 (July 2019). ISSN: 1079-7114. DOI: 10.1103/physrevlett.123.036601.
- [31] J. Vučičević, P. Stipsić, and M. Ferrero. "Analytical solution for time integrals in diagrammatic expansions: Application to real-frequency diagrammatic Monte Carlo". In: *Physical Review Research* 3.2 (Apr. 2021). ISSN: 2643-1564. DOI: 10.1103/physrevresearch.3.023082.
- [32] M. Lewenstein et al. "Ultracold atomic gases in optical lattices: mimicking condensed matter physics and beyond". In: *Advances in Physics* 56.2 (Mar. 2007), pp. 243–379. ISSN: 1460-6976. DOI: 10.1080/00018730701223200.
- [33] C. Gross and I. Bloch. "Quantum simulations with ultracold atoms in optical lattices". In: *Science* 357.6355 (Sept. 2017), pp. 995–1001. ISSN: 1095-9203. DOI: 10.1126/science.aal3837.
- [34] A. N. Rubtsov, V. V. Savkin, and A. I. Lichtenstein. "Continuous-time quantum Monte Carlo method for fermions". In: *Physical Review B* 72.3 (July 2005). ISSN: 1550-235X. DOI: 10.1103/physrevb.72.035122.
- [35] E. Gull et al. "Continuous-time auxiliary-field Monte Carlo for quantum impurity models". In: *EPL (Europhysics Letters)* 82.5 (May 2008), p. 57003. ISSN: 1286-4854. DOI: 10.1209/0295-5075/82/57003.
- [36] R. Rossi, F. Šimkovic, and M. Ferrero. "Renormalized perturbation theory at large expansion orders". In: EPL (Europhysics Letters) 132.1 (Nov. 2020), p. 11001. ISSN: 1286-4854. DOI: 10.1209/0295-5075/132/11001.

- [37] G. Baym and L. P. Kadanoff. "Conservation Laws and Correlation Functions". In: *Physical Review* 124.2 (Oct. 1961), pp. 287–299. ISSN: 0031-899X. DOI: 10. 1103/physrev.124.287.
- [38] G. Baym. "Self-Consistent Approximations in Many-Body Systems". In: Physical Review 127.4 (Aug. 1962), pp. 1391–1401. ISSN: 0031-899X. DOI: 10.1103/physrev.127.1391.
- [39] E. Kozik, M. Ferrero, and A. Georges. "Nonexistence of the Luttinger-Ward Functional and Misleading Convergence of Skeleton Diagrammatic Series for Hubbard-Like Models". In: *Physical Review Letters* 114.15 (Apr. 2015). ISSN: 1079-7114. DOI: 10.1103/physrevlett.114.156402.
- [40] K. Zantout, S. Backes, and R. Valentí. "Two-Particle Self-Consistent Method for the Multi-Orbital Hubbard Model". In: Annalen der Physik 533.2 (Jan. 2021). ISSN: 1521-3889. DOI: 10.1002/andp.202000399.
- [41] M. Potthoff, M. Aichhorn, and C. Dahnken. "Variational Cluster Approach to Correlated Electron Systems in Low Dimensions". In: *Physical Review Letters* 91.20 (Nov. 2003). ISSN: 1079-7114. DOI: 10.1103/physrevlett.91.206402.
- [42] C.-O. Almbladh, U. v. Barth, and R. v. Leeuwen. "VARIATIONAL TOTAL ENERGIES FROM Φ- AND Ψ- DERIVABLE THEORIES". In: International Journal of Modern Physics B 13.05n06 (Mar. 1999), pp. 535–541. ISSN: 1793-6578. DOI: 10.1142/s0217979299000436.
- [43] J. Vučičević et al. "Practical consequences of the Luttinger-Ward functional multivaluedness for cluster DMFT methods". In: *Physical Review B* 97.12 (Mar. 2018). ISSN: 2469-9969. DOI: 10.1103/physrevb.97.125141.
- [44] M. Ferrero et al. "Pseudogap opening and formation of Fermi arcs as an orbital-selective Mott transition in momentum space". In: *Physical Review B* 80.6 (Aug. 2009). ISSN: 1550-235X. DOI: 10.1103/physrevb.80.064501.
- [45] H. Bruus and K. Flensberg. *Many-body quantum theory in condensed matter physics*. Oxford Graduate Texts. Oxford University Press, 2004.
- [46] C. Berthod. Applications of the Many-Body Formalism in Condensed-Matter Physics, lecture notes. University of Geneva, 2011. URL: https://giamarchi.unige.ch/wp-content/php\_code/people/christophe.berthod/pdf/Many-body.pdf.
- [47] D. Manzano. "A short introduction to the Lindblad master equation". In: *AIP Advances* 10.2 (Feb. 2020). ISSN: 2158-3226. DOI: 10.1063/1.5115323.
- [48] H. Aoki et al. "Nonequilibrium dynamical mean-field theory and its applications". In: *Reviews of Modern Physics* 86.2 (June 2014), pp. 779–837. ISSN: 1539-0756. DOI: 10.1103/revmodphys.86.779.
- [49] F. Krien et al. "Conservation in two-particle self-consistent extensions of dynamical mean-field theory". In: *Physical Review B* 96.7 (Aug. 2017). ISSN: 2469-9969. DOI: 10.1103/physrevb.96.075155.

- [50] O. Parcollet et al. "TRIQS: A toolbox for research on interacting quantum systems". In: *Computer Physics Communications* 196 (Nov. 2015), pp. 398–415. ISSN: 0010-4655. DOI: 10.1016/j.cpc.2015.04.023.
- [51] P. Virtanen et al. "SciPy 1.0: Fundamental Algorithms for Scientific Computing in Python". In: *Nature Methods* 17 (2020), pp. 261–272. DOI: 10.1038/s41592-019-0686-2.
- [52] J. A. Nelder and R. Mead. "A Simplex Method for Function Minimization". In: *The Computer Journal* 7.4 (Jan. 1965), pp. 308–313. ISSN: 1460-2067. DOI: 10.1093/comjnl/7.4.308.
- [53] F. Harris. "On the use of windows for harmonic analysis with the discrete Fourier transform". In: *Proceedings of the IEEE* 66.1 (1978), pp. 51–83. ISSN: 0018-9219. DOI: 10.1109/proc.1978.10837.
- [54] J. Vučičević, S. Predin, and M. Ferrero. "Charge fluctuations, hydrodynamics, and transport in the square-lattice Hubbard model". In: *Physical Review B* 107.15 (Apr. 2023). ISSN: 2469-9969. DOI: 10.1103/physrevb.107.155140.
- [55] H. Hafermann et al. "Collective charge excitations of strongly correlated electrons, vertex corrections, and gauge invariance". In: *Physical Review B* 90.23 (Dec. 2014). ISSN: 1550-235X. DOI: 10.1103/physrevb.90.235105.
- [56] J. Kokalj. "Bad-metallic behavior of doped Mott insulators". In: *Physical Review B* 95.4 (Jan. 2017). ISSN: 2469-9969. DOI: 10.1103/physrevb.95.041110.
- [57] D. Manzano and P. Hurtado. "Harnessing symmetry to control quantum transport". In: *Advances in Physics* 67.1 (Jan. 2018), pp. 1–67. ISSN: 1460-6976. DOI: 10.1080/00018732.2018.1519981.
- [58] A. Altland and B. D. Simons. Condensed Matter Field Theory. Cambridge University Press, Mar. 2010. ISBN: 9780511789984. DOI: 10.1017/cbo9780511789984.